DESY HERA 00–02

# HERA accelerator studies 1999

Edited by Georg H. Hoffstaetter

May 2000

# Abstract

The HERA accelerator study periods during 1999 were mainly concerned with issues of the luminosity upgrade project and with the disturbing production of coasting beam in the proton ring. These were already important subjects during the accelerator studies of December 1998 [11].

The effect of high lepton currents on the proton beam were investigated and found to be benign. However, experiences with the beam–beam disturbance for the electron emittance and polarization was found to be non–negligible. It is planned to reduce the horizontal electron emittance from the current $41\pi$nm to $22\pi$nm during the luminosity upgrade by increasing the RF frequency by about 300Hz and by using a 72° optics. Thus optic tests related to this change were performed and in particular the dynamic aperture and the luminosity were studied. Since the synchrotron radiation will have to go through the beam pipe of the detectors H1 and ZEUS after the luminosity upgrade, synchrotron radiation background will gain importance and even the radiation produced in the tail has to be considered. Therefore a scraper had been installed in the East section and was used for improved studies of tails in the electron beam distribution. Understanding the current optics is a prerequisite for understanding more advanced schemes and therefore some optical properties of the current HERA electron ring were measured. To be able to investigate the source of lifetime reductions for the electron beam, improved beam loss monitors were tested.

The readout and triggering of the HERA-B experiment relies strongly on a close correlation between the interactions and the bunch crossing signal. Coasting beam leads to a background of interactions which cannot be reconstructed and which can therefore spoil the particle physics results. Particle identification in the HERA-B experiment becomes disturbed by a coasting beam, and furthermore this unbunched beam appears to cause background spikes in H1 and ZEUS. Therefore the production of coasting beam in HERA was analyzed. This involves also the review of data taken in HERA–B during the last few years. Furthermore, various ways of eliminating coasting particles from the beam were tested. A further disturbance to the HERA–B experiment is unstable interaction rates. When the proton beam moves with respect to the HERA–B wires, the interaction rate can change rapidly. During December 1999 tests were made on how such unstable rates can be reduced by softening the edges of the proton beam distribution by means of a harmonic tune modulation.

# Contents

# 1 Experiments about the Beam–Beam Effect at HERA

M. Bieler, E. Gianfelice, G. Hoffstaetter,
T. Limberg, M. Minty, F. Willeke, DESY Hamburg

Date: 1999, Apr. 7, 3pm to Apr. 7, 11pm, Logbook XXXVI, p. 219–227
Date: 1999, Dec. 17, 3pmto Dec. 18, 1am, Logbook XXXXI, p. 55–60
Date: 1999, Dec. 18, 7amto Dec. 18, 11pm,Logbook XXXXI, p. 70–73

Proton beam stability during collision with high current electron bunches was of foremost concern during the design stages of the HERA collider [1]. In initial commissioning, the beam–beam interaction proved to be a key factor in determining the lifetime of the proton beam. It was quickly ascertained [2] that the proton beam lifetime in collision could be substantially increased by both matching the electron and proton beam sizes at the interaction points (IPs) and by carefully centering the beams. Presently, proton beam lifetimes of hundreds of hours are routinely observed. In the near future, the accelerators will be upgraded [3, 4] to include new low–$\beta$ insertions and to allow for yet higher beam currents. Experiments have been performed to explore at high electron beam currents new regimes of the proton beam–beam limit at HERA. Some recent observations on the influence of the beam–beam effect on electron dynamics and the specific luminostiy are also presented.

## 1.1 Introduction

In luminosity operation HERA-e is filled with 189 bunches. The HERA-p ring is filled with 180 proton bunches. The resultant current distribution contains 15 non–colliding $e^-$ bunches and 6 non–colliding proton bunches. The electron 'pilot' bunches are used to correct the online luminosity estimate for residual beam–gas–scattering events. With a head–on collision geometry at each of the two HERA interaction points, parasitic crossings and bunch scheduling issues are fortunately of no concern since the 11.6 m common orbit at the HERA IPs is less than half the 28.8 m bunch spacing.

After both beams are ramped to their top energy, the separation of the beams at the IPs is about $40\sigma$ vertically before they are brought into collision. A selection of beam parameters is given in Table 1.1. The luminosity, given by

$$L = \frac{1}{2\pi} \frac{N_e N_p f_r}{\Sigma_x \Sigma_y} \tag{1.1}$$

with $\Sigma_{x/y} = \sqrt{\sigma^2_{x/y,e} + \sigma^2_{x/y,p}}$ and an interaction frequency of $f_r = 174 \times 47.273$ kHz, is typically $L = (8 - 10) \times 10^{30}$ cm$^{-2}$s$^{-1}$. The corresponding specific luminosity is

| Parameter | proton | electron |
|---|---|---|
| E (GeV) | 920 | 27.5 |
| $I_{tot}$ (mA) | 80 | 30 |
| N (total/colliding) | 180/174 | 189/174 |
| $N_{ppb}$ | $5.9 \times 10^{10}$ | $2.1 \times 10^{10}$ |
| $I_b$ ($\mu$A) | 445 | 160 |
| $\beta_x^*, \beta_y^*$ (m) | 7,0.5 | 1,0.7 |
| $\epsilon_{x,y}$ (nm-r) | 5.1/5.1 | 40/4.0 |
| $\sigma_x, \sigma_y$ ($\mu m$) | 190,50 | 200,53 |
| $\nu_x, \nu_y$ | 0.291, 0.298 | 0.140, 0.194 |
| $\nu_s$ | 0.0011 | 0.0525 |
| $\tau_x, \tau_y$ (ms) | - | 14, 14 |
| $\tau_s$ (ms) | - | 7 |
| $\xi_x$, $\xi_y$ | 0.0007,0.00019 | 0.0108, 0.0287 |

**Table 1.1**: HERA parameters of the 1998/1999 physics run to date including the beam energy E, the total current $I_{tot}$, the number of bunches N, the number of particles per bunch $N_{ppb}$, the current per bunch $I_b$, the IP beta functions $\beta^*$, the beam emittances $\epsilon$, the IP spot sizes $\sigma$, the betatron and synchrotron tunes $\nu_x, \nu_y, \nu_s$, the damping times $\tau$, and the incoherent beam–beam parameters $\xi$ per crossing. Note that the tunes of the protons and of the electrons are quite different.

$L_{sp} = 6.6 \times 10^{29}$ cm$^{-2}$s$^{-1}$ mA$^{-2}$ which is 75% greater than design [5] due primarily to the reduced $\beta^*$ at the interaction points.

General observations, measurements related to beam–beam effects at HERA, and knowledge gained since the time when beams were first collided at HERA are described in [6]. Parts of the following descriptions of HERA accelerator physics studies are taken from this reference. Here we present recent measurements performed to determine if a beam–beam limit might be encountered at higher beam currents and or smaller beam emittances. This information is relevant for machine operation after the luminosity upgrade [3, 4].

## 1.2 Beam–Beam Effect on the Electrons

### 1.2.1 Electron Polarization

Having increased the proton current in HERA during the last years, we observe an average reduction of spin polarization of the electron/positron beam and an increased sensitivity to the choice of betatron and synchrotron tunes. We have different indications that tightly focused and/or high current proton beams have led to less polarization [7]. With large tune shifts from the beam–beam interaction, sometimes the polarization approached only 50%. Since the time of these observations, the electron beam tune shift was decreased by reducing the $\beta_y^{e*}$ from 1m to 0.6m at the IP and now 55-65% electron polarization routinely is reached [5].

This is supported by the following observation: In routine operation, given the

long proton beam lifetime of several hundreds of hours, often two electron injection cycles per proton fill are employed. From the time history shown in figure 1.1, the electron polarization is often higher for those electron fills corresponding to the older and less focusing proton beams.

An additional indication is shown in figure 1.2. The measured spin polarization is plotted versus the luminosity over a period of two weeks. The polarization level reached after the buildup time is given by the uppermost points forming an edge sloping down towards higher luminosity. Initial electron currents were kept rather constant during this time, so luminosity on that line can be taken as a measure of the proton currents and thus the electron tune shift. The maximum is reached for zero luminosity, meaning electrons only, i.e. in the absence of the beam–beam interaction. Towards higher proton currents and electron tune shifts the polarization drops by about 10% absolute.

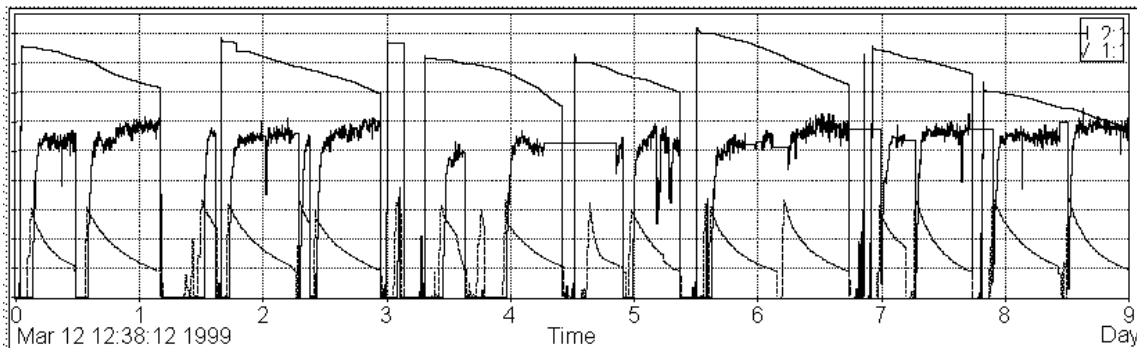


**Figure 1.1**: Time history of HERA proton (top) and electron (bottom) currents and the electron polarization (middle).

### 1.2.2 Electron Tune Shifts

The incoherent tune shift per IP of the electrons is

$$\xi^e_{x,y} = (\frac{r_e}{2\pi})\frac{N_{\rm ppb}\beta^{*e}_{x,y}}{\gamma_e\sigma^p_{x,y}(\sigma^p_x+\sigma^p_y)} \tag{1.2}$$

with $r_e = 2.82 \times 10^{-15}$ m, the proton rms beam size at the IP $\sigma^p_{x,y}$, and with the proton bunch population $N_{\rm ppb}$. For the electrons, a single bunch within a given bunch train may be externally excited and its betatron tunes measured [9]. This independent gating feature allows for comparison of the betatron tunes for colliding and non–colliding (pilot) bunches. An example is given in figure 1.3.

Using this technique, the electron beam–beam tune shift was measured over a small range of proton single bunch beam currents by taking the difference of the measured tunes for colliding and non–colliding bunches. The result is shown in figure 1.4. For example, the measurements at the beam currents of Table 1 were

$$\Delta\nu^e_x = 0.010 \quad \text{and} \quad \Delta\nu^e_y = 0.024\ . \tag{1.3}$$

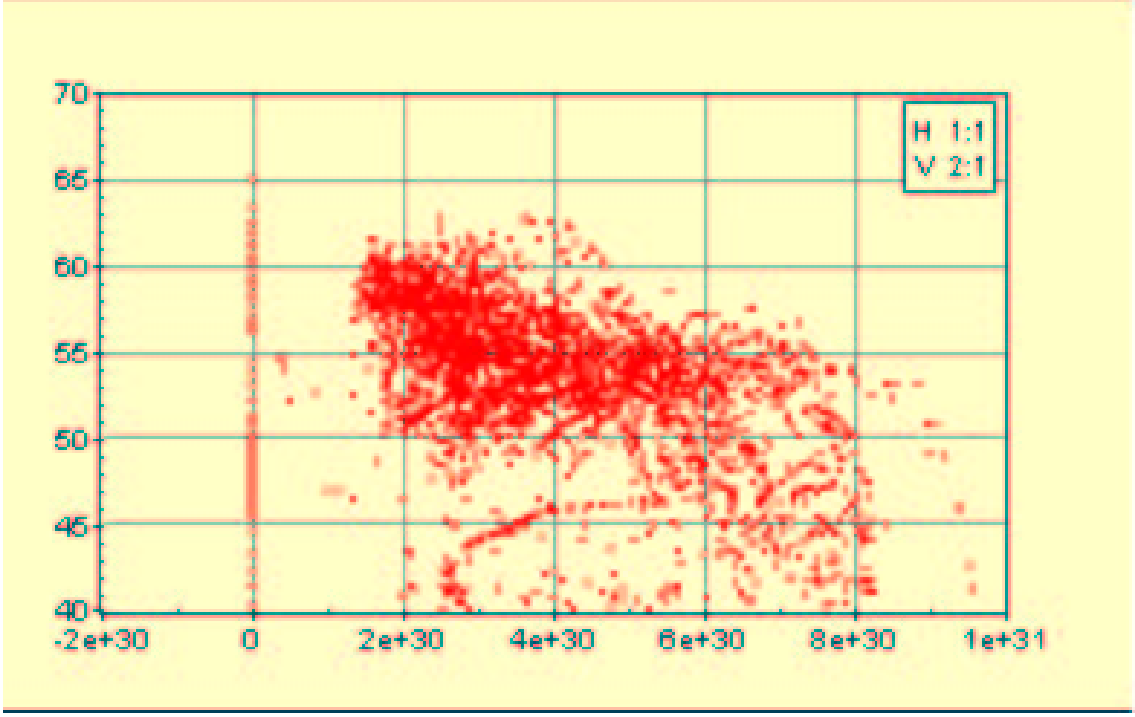


**Figure 1.2**: Polarization versus luminosity over a period of two weeks (starting March 11, 1999).

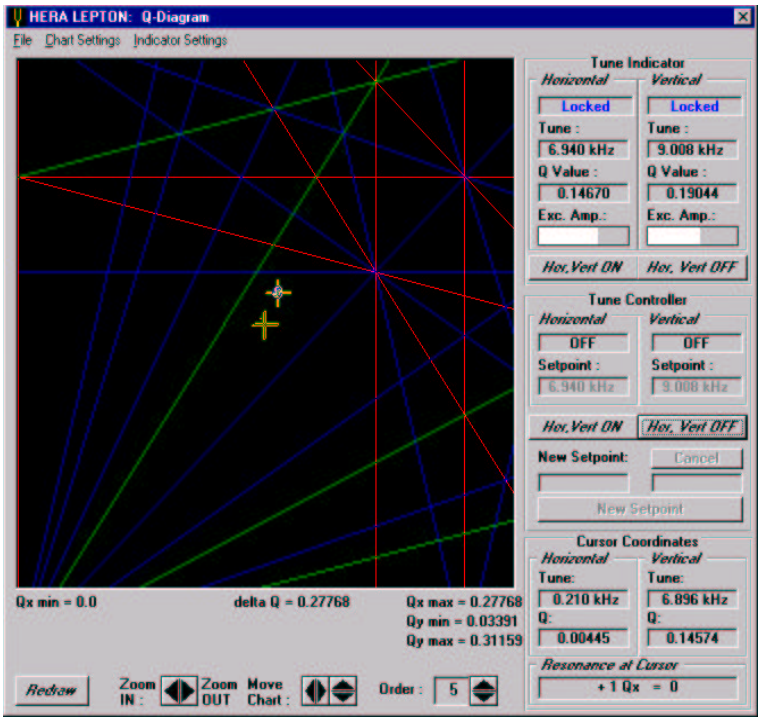


**Figure 1.3**: Tune diagram showing measured beam–beam tune shifts of an electron bunch in collision with protons (upper cross) and for a pilot bunch (lower cross).

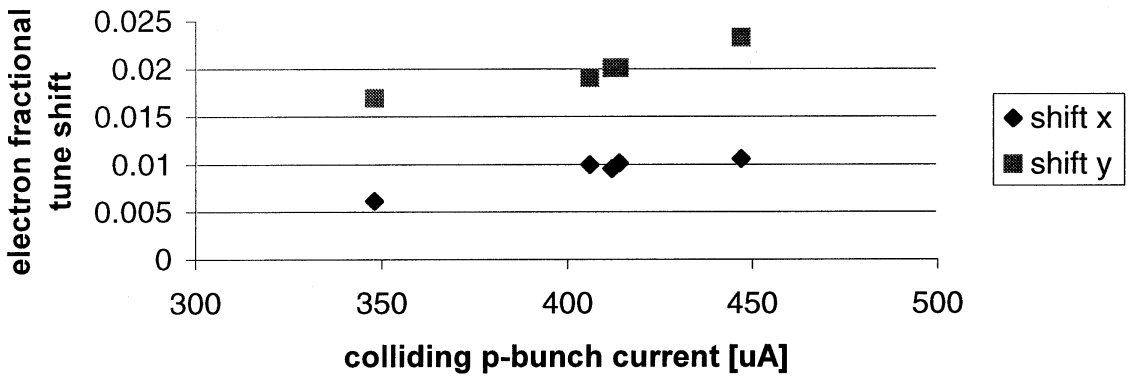


**Figure 1.4**: Fractional electron tune shifts $\Delta\nu_x^e$ versus colliding p–bunch current.

Here $\Delta\nu^e$ denotes the measured coherent tune shift. As shown in [10] and re–derived in two ways in the appendix, the coherent beam–beam tune shift for a ring with $N_{IP}$ interaction points is approximately by a factor 2 smaller than $N_{IP}\xi_x$ or $N_{IP}\xi_y$. For $N_{IP} = 2$ in HERA, the expectation is therefore $\Delta\nu^e_{x,exp} = 0.011$ and $\Delta\nu^e_{y,exp} = 0.029$. Here the first order expansion in the focusing perturbation is used. The discrepancy can be reduced by taking into account the additional focusing of the beam at each IP by the beam–beam interaction which in turn introduces a modulation of the beta function. This amounts to taking the focusing perturbation to second order, which leads to a tune shift of

$$\Delta\nu^e = \frac{N_{IP}}{2}\xi\{1 - \frac{\pi\xi}{\sin(2\pi Q)}[\cos(2\pi Q) + \cos(2|\Delta\phi| - 2\pi Q)]\} \ . \tag{1.4}$$

where $\Delta\phi$ is the relative difference between IPs in the betatron phase advance. Here the result of the appendix, that the measured tune shift $\Delta\nu^e$ is expected to be half the incoherent tune shift $\xi$ for matched Gaussian beams, has again be used. Note that this is not $\xi(1 + \frac{\Delta\beta}{\beta})$ but $\xi(1 + \frac{\Delta\beta}{2\beta})$. This fact can be derived by investigating the trace of the one turn matrix

$$\begin{aligned} \underline{M} &= \begin{pmatrix} \cos\mu_0 + \alpha_0 \sin\mu_0 & \beta_0 \sin\mu_0 \\ -\gamma_0 \sin\mu_0 & \cos\mu_0 + \alpha \sin\mu_0 \end{pmatrix} \begin{pmatrix} 1 & 0 \\ -\Delta k & 1 \end{pmatrix} \ , \\ \mathrm{tr}(\underline{M}) &= 2\cos(\mu_0 + \Delta\mu) = (2 - \Delta\mu^2)\cos\mu_0 - 2\Delta\mu \sin\mu_0 + O(\Delta\mu^3) \ . \end{aligned} \tag{1.5}$$

With $\mathrm{tr}(\underline{M}) = 2\cos\mu_0 - \Delta k\beta_0 \sin\mu_0$ one obtains a quadratic equation for $\Delta\mu$. The second order approximation in $\Delta k$ is denoted by $\Delta\mu_2$ and is obtained by expanding the solution of the quadratic equation in second order of $\Delta k$,

$$\Delta\mu_2^2 + 2\Delta\mu_2 \tan\mu_0 - \Delta k\beta_0 \tan\mu_0 = 0 \ , \tag{1.6}$$

$$\Delta\mu_2 = \frac{\Delta k\beta_0}{2}(1 - \frac{\Delta k\beta_0}{4\tan\mu_0}) \ . \tag{1.7}$$

The beta–beat $\Delta\beta$ is obtained by $M_{12} = (\beta_0 + \Delta\beta)\sin(\mu_0 + \Delta\mu) = \beta_0 \sin\mu_0$. After

inserting $\Delta\mu = \frac{\Delta k \beta_0}{2} + O(\Delta k^2)$ one obtains to first order in $\Delta k$, $\Delta\beta_1 = -\frac{\Delta k \beta_0^2}{2 \tan \mu_0}$ and

$$\Delta\mu_2 = \frac{\Delta k}{2}(\beta_0 + \frac{1}{2}\Delta\beta_1) \ . \tag{1.8}$$

In the design optics of HERA-e these phases are $\Delta\phi_x = 2\pi \cdot 23.763$ and $\Delta\phi_y = 2\pi \cdot 23.845$ for the tunes $Q_x = 47.148$ and $Q_y = 47.216$. This would lead to calculated tune shifts $\Delta\nu_{y,calc} = 0.011$, $\Delta\nu_{y,calc} = 0.031$ . However, the phase advance between the two interaction points can be perturbed, and depending on this phase $\Delta\nu^e_{x,calc}$ can be between 0.010 and 0.011 and $\Delta\nu^e_{y,calc}$ can be between 0.026 and 0.031 when $2|\Delta\Phi|$ is somewhere between 0 and $2\pi$.

## 1.3 Beam–Beam Effect on the Protons

For a number of bunch pairs, bunch currents and lifetimes were measured over a few hours. The proton lifetime correlates nicely with the intensity of the colliding electron bunch (figure 1.5). In a similar experiment for the electron beam–beam effect, the electron lifetime was not correlated with the proton bunch current.

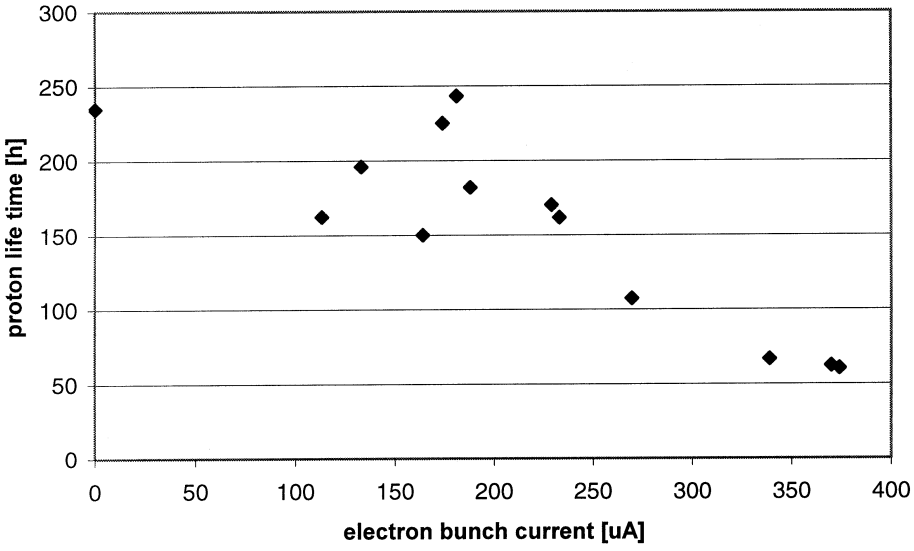


**Figure 1.5**: Proton bunch lifetime versus colliding e–bunch current.

### 1.3.1 The Proton Beam Core

The luminosity versus beam current was measured by varying the electron current per bunch and measuring the luminosity per crossing for the bunches of interest. For these measurements, the proton bunch currents were roughly constant and a special fill with varying electron bunch currents was injected as shown in figure 1.6. The maximum single bunch electron current of about 450 $\mu$A is about 1.7 times the nominal or design electron bunch current [12].

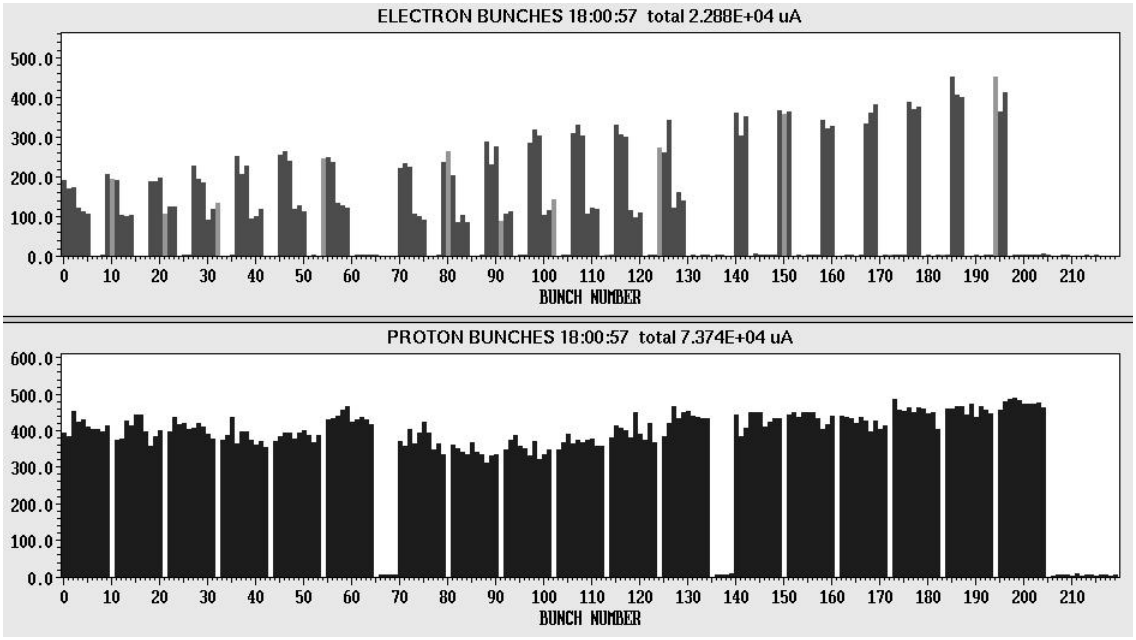


**Figure 1.6**: Current distributions used in beam–beam studies with specially tailored electron bunch currents.

Shown in figure 1.7 is the specific luminosity measured bunch–by–bunch by the H1 detector versus time for the electron bunch currents of figure 1.6. Each curve shows the average luminosity where the average is taken over all bunches with currents in a window of 25 $\mu$A over the range of 75 to 450 $\mu$A. The gradual loss of specific luminosity during the measurements was recovered with tuning optimization as evidenced by the two step increases. There are two positive outcomes of this experiment. Firstly, there is no correlation between the luminosity at any given time with electron beam current (while not shown, the current is not increasing from bottom to top, for example). Secondly, the 10% variation between the curves remained unchanged over the duration of the experiment. Taken together this indicates that the beam–beam interaction at high electron beam currents, as in this measurement, should not contribute to any time–dependent degradation of luminosity.

Two features of these data are not explained quantitatively. First the variation between the curves, being e–beam current independent, may or may not be a result of emittance degradations within HERA-p. Most likely, the injected beam emittance already varied from bunch to bunch. However, there is evidence of longitudinal beam instabilities measured at the top of the proton energy ramp and persisting for one to two hours [13]. Whether these observations are related has not been confirmed.

Taking as a measure of the time dependence of the measured specific luminosity the values after optimization at 61.2 and 99.3 minutes, we find a change of 1.6% or about 2.6% per hour. This level of change is consistent with proton beam emittance dilutions arising via the beam–beam interaction with an accelerating voltage phase modulation on the electron beam of much less than 1 mrad [14].

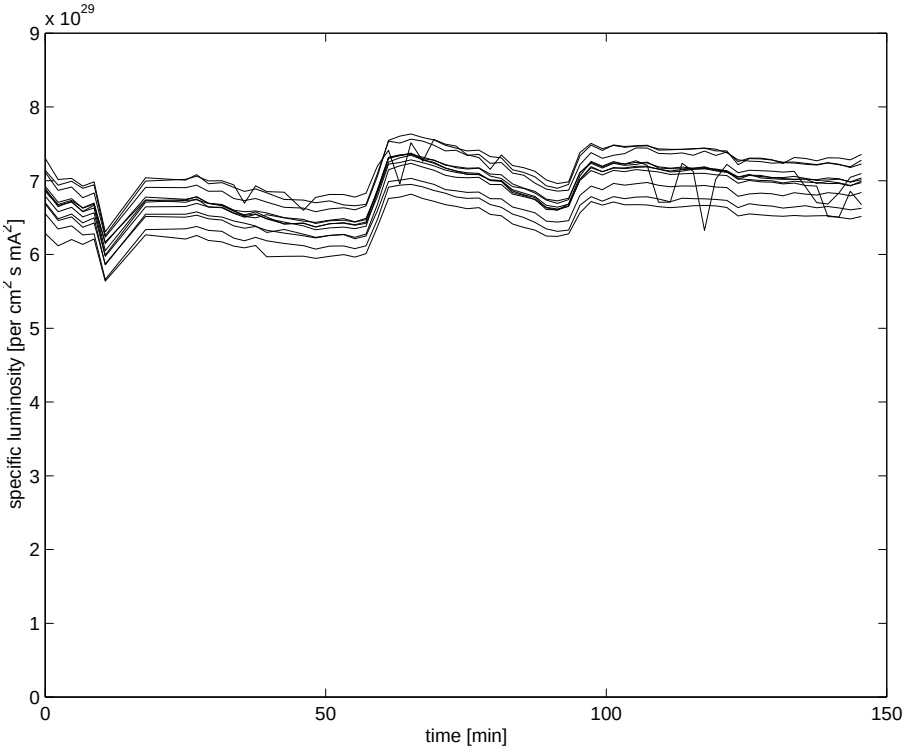


**Figure 1.7**: Specific luminosity measured by the H1 detector versus time for electron beam currents ranging from 75 to 450 $\mu$A in 25 $\mu$A steps. The proton bunch currents were on average 400 $\mu$A. The two step increases at 60 and 95 minutes resulted from a routine optimization of the relative beam positions at the IPs.

### 1.3.2 The Proton Beam Tails

The population of the beam tails generated by the beam–beam interaction was studied with the current distribution shown in figure 1.6 using the data acquisition systems of HERA-B. During standard operation a 50$\mu$m wire, whose position is controlled by feedback to maintain a constant data rate, is moved into the beam. The wire intercepts the tails of the beam distribution and the interaction rates are recorded versus bunch number.

In this experiment, after ramping to full energy before colliding the beams, collimators in high dispersion regions were used to scrape the proton beam tails. Using the HERA-B data acquisition system, the tail population was observed to be uniform from bunch to bunch. After two hours of colliding beams, HERA-B was again used to measure the rate versus electron bunch number as shown in figure 1.8. The event rate is observed to mimic the population of the electron beam with which the protons collide (see figure 1.6); the proton event rate for collisions with high current electrons was clearly higher than that of lower current electron bunches. A possible explanation is that the higher current collisions with correspondingly large beam–beam tune shifts, have larger beam tails arising possibly from nearby nonlinear optical resonances excited by the nonlinear beam–beam force.

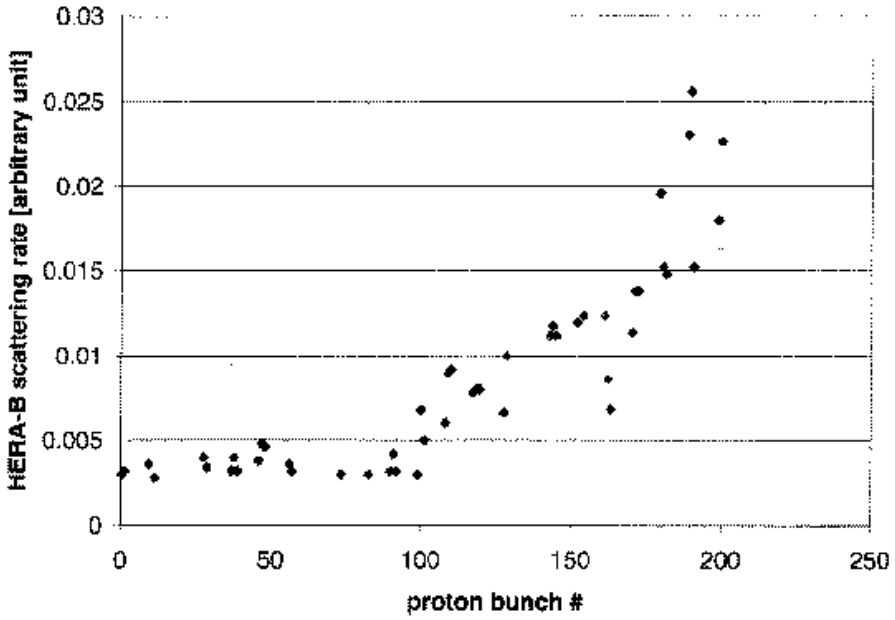


**Figure 1.8**: Beam tail scattering rate versus proton bunch number as measured by HERA-B with the scattering target just intercepting the beam halo.

The uniformity of the proton beam tails was next investigated by moving the HERA-B wire into the beam. The wire was stepped in 5 $\mu$m steps and the measured rates were recorded. Shown in figure 1.9 is the rate averaged over all bunches obtained with a high sampling frequency. In this experiment, the feedback loop used nominally to maintain a constant interaction rate was turned off; the step increases

in measured rate correspond to the insertion of the wire and the exponential decay of the rate shows the removal of particles from the proton beam tail.

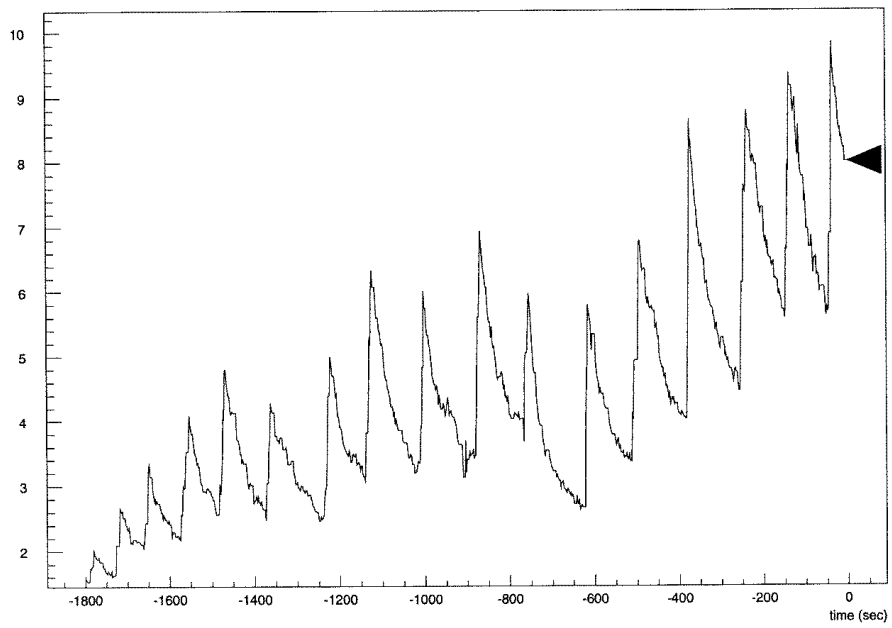


**Figure 1.9**: Beam tail scattering rate as measured by HERA-B versus time. The target was inserted in 5$\mu$m steps as indicated by the spikes. Time increases from left to right in this figure.

After collimating out the largest amplitude particles, the scattering rate versus bunch number was again measured as shown in figure 1.10. Comparison with figure 1.8 shows that the rate over the particle distribution became smoother; that is, the beam–beam interaction with the highest current electron bunches contributed to large amplitude particles while leaving the core of the beam distribution unchanged.

## 1.4 Summary

Taking into account the additional focusing of the beam–beam interaction, calculations and measurement of the beam–beam tune shifts can be brought in good agreement. Recent high current experiments performed to confirm the feasibility of the HERA upgrade proposal further extended the parameter regime to higher beam currents. Even at electron beam currents almost a factor of 3 times nominal, there was no evidence of a proton beam–beam limit. Nor was there observed any correlation between the electron current and specific luminosity. This suggests strongly that the electron and proton beam cores are not degraded by the beam–beam interaction. The lack of variation with time in this experiment is very encouraging. Tail–scraping measurements also seem to indicate that the core of the beam distribution is left intact even at very high beam currents. Consistency between observations both old and new gives confidence that subtle nonlinearities in the beam–beam in-

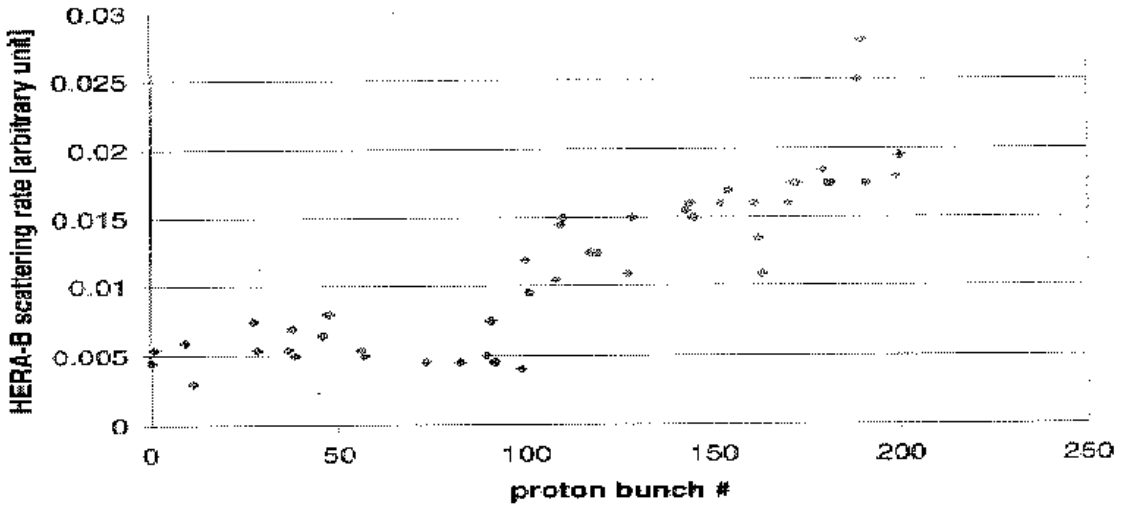


**Figure 1.10**: Beam tail scattering rate versus electron bunch current as measured by HERA-B with the wire about 100 $\mu$m closer to the core of the beam.

teraction should not limit accelerator performance with the parameters to be used in the HERA upgrade [3, 4].

## 1.5 Appendix – Coherent Tune Shift

### 1.5.1 The Beam–Beam Tune Shift of the Dipole moment

In order to compute the coherent beam–beam tune shift, we want to analyze how the dipole moment of the beam is transported around the ring. At a transverse phase space coordinate $\vec{z} = (x, x', y, y')$ the density of the beam at the azimuth $s$ in the ring is given by $\rho(\vec{z}, s)$. The dipole moment of the beam is then defined as

$$\vec{d}(s) = \int_\infty \rho(\vec{z}, s)\vec{r}(\vec{z})d\vec{z} \; . \tag{1.9}$$

For generality we express positions and slopes as $\vec{r}(\vec{z})$ and $\vec{r}'(\vec{z})$. When the transformation of phase space variables from $\vec{z}_0$ at azimuth 0 is given by the transfer map $\vec{z} = \vec{M}(\vec{z}_0, s)$ and the inverse transformation is given by $\vec{z}_0 = \vec{M}^{-1}(\vec{z}, s)$, then Liouville's theorem about the conservation of phase space density states $\rho(\vec{z}, s) = \rho(\vec{z}_0, 0) = \rho(\vec{M}^{-1}(\vec{z}, s), 0)$. Since the Jacobi matrix for a Hamiltonian map $\vec{M}$ has a unit determinant, the dipole moment can be reexpressed as

$$\vec{d}(s) = \int_\infty \rho(\vec{M}^{-1}(\vec{z}, s), 0)\vec{r}(\vec{z})d\vec{z} = \int_\infty \rho(\vec{z}_0, 0)\vec{r}(\vec{M}(\vec{z}_0, s))d\vec{z}_0 \; . \tag{1.10}$$

The slope of the dipole moment is then $\vec{d}'(s) = \int_0^\infty \rho(\vec{z}_0, 0)\vec{r}'(\vec{M}(\vec{z}_0, s))d\vec{z}_0$. For a linear equation of motion, the vector $(\vec{r}, \vec{r}')$ and the vector $(\vec{d}, \vec{d}')$ obey the same

equation of motion,

$$\frac{d}{ds}\begin{pmatrix}\vec{r}\\ \vec{r}'\end{pmatrix} = \underline{A}(s)\begin{pmatrix}\vec{r}\\ \vec{r}'\end{pmatrix} , \tag{1.11}$$

$$\frac{d}{ds}\begin{pmatrix}\vec{d}\\ \vec{d}'\end{pmatrix} = \int_\infty \rho(\vec{z}_0,0)\underline{A}(s)\begin{pmatrix}\vec{r}(\vec{M}(\vec{z}_0,s))\\ \vec{r}'(\vec{M}(\vec{z}_0,s))\end{pmatrix} d\vec{z}_0 = \underline{A}(s)\begin{pmatrix}\vec{d}\\ \vec{d}'\end{pmatrix} . \tag{1.12}$$

In a ring with linear particle transport of non–interacting particles, the oscillation frequency of a single particle is therefore equivalent to the oscillation frequency of the beam's dipole moment.

Now we want to investigate the oscillation frequency of the dipole moment in a collider with one interaction point where a beam 1 passes through a counter–rotating beam 2. For that we assume the particle transport from the beam–beam region once around the ring to be linear so that the vectors $(\vec{r},\vec{r}')$ and $(\vec{d},\vec{d}')$ have the same transport matrix $\underline{M}_0$ for the transport through this region.

The following convolution of Gaussians will be used several times:

$$G^\sigma(x) = \frac{1}{\sqrt{2\pi}\sigma}\exp(-\frac{x^2}{2\sigma^2}) , \quad \int_\infty G^{\sigma_1}(x-\tilde{x})G^{\sigma_2}(x)dx = G^{\sqrt{\sigma_1^2+\sigma_2^2}}(\tilde{x}) . \tag{1.13}$$

In the horizontal degree of freedom, the distribution of the action $J_x$ in a Gaussian beam is given by $E^{\epsilon_x}(J_x) = \frac{1}{\epsilon_x}\exp(-\frac{J_x}{\epsilon_x})$, where $\epsilon_x$ is the $1\sigma$ emittance. The phase space density is therefore

$$\rho(\vec{z},s)d\vec{z} = E^{\epsilon_x}(J_x)E^{\epsilon_y}(J_y)dJ_xdJ_y\frac{d\phi_x d\phi_y}{(2\pi)^2} . \tag{1.14}$$

The projection onto the horizontal plane is then given by a Gaussian,

$$\int_\infty \frac{1}{2\pi}E^{\epsilon_x}(J_x)dx' = G^{\sigma_x}(x) , \quad \sigma_x = \sqrt{\epsilon_x\beta_x} , \tag{1.15}$$

where the horizontal beta function is used. When a particle of charge $q_1$ and velocity $v_1$ in beam 1 with distance $\vec{r}$ from the center of beam 2 passes a bunch of beam 2 which has the total charge $q_2N_2$, velocity $v_2$, and $1\sigma$ transverse beam sizes $\sigma_{2x}$ and $\sigma_{2y}$, then the particle's slope $\vec{r}'$ changes by [10]

$$\Delta\vec{r}' = -C_{bb}\partial_{\vec{r}}U^{\sigma_{2x},\sigma_{2y}}(\vec{r}) , \tag{1.16}$$

$$C_{bb} = \frac{q_2}{q_1}\frac{N_2 r_1^C}{\gamma_1}\frac{c^2+v_1v_2}{v_1(v_1+v_2)} , \tag{1.17}$$

$$U^{\sigma_{2x},\sigma_{2y}}(\vec{r}) = 2\pi\int_0^\infty G^{\sqrt{\sigma_{2x}^2+t}}(x)G^{\sqrt{\sigma_{2y}^2+t}}(y)dt . \tag{1.18}$$

For small distances $\vec{r}$, the exponential can be expanded and to leading order,

$$\begin{aligned}
\Delta x' &=_1 xC_{bb}\int_0^\infty \frac{dt}{\sqrt{(\sigma_{2x}^2+t)^3(\sigma_{2y}^2+t)}} = xC_{bb}\int_{\sigma_{2x}^2}^\infty \frac{d\tau}{\tau^2\sqrt{\frac{\sigma_{2y}^2-\sigma_{2x}^2}{\tau}+1}} \\
&= -xC_{bb}\int_{\frac{1}{\sigma_{2x}^2}}^0 \frac{du}{\sqrt{(\sigma_{2y}^2-\sigma_{2x}^2)u+1}} = -2xC_{bb}\left[\frac{\sqrt{(\sigma_{2y}^2-\sigma_{2x}^2)u+1}}{\sigma_{2y}^2-\sigma_{2x}^2}\right]_{\frac{1}{\sigma_{2x}^2}}^0 \\
&= -2xC_{bb}\frac{1-\sigma_{2y}/\sigma_{2x}}{\sigma_{2y}^2-\sigma_{2x}^2} = C_{bb}\frac{2}{(\sigma_{2x}+\sigma_{2y})}\frac{x}{\sigma_{2x}} \ . \qquad (1.19)
\end{aligned}$$

This is the well known formula for the beam–beam kick and leads to the shift of the incoherent tunes of $\xi_x = -C_{bb}\frac{2}{\sigma_{2x}+\sigma_{2y}}\frac{\beta_x}{4\pi\sigma_{2x}}$ and $\xi_y = -C_{bb}\frac{2}{\sigma_{2x}+\sigma_{2y}}\frac{\beta_y}{4\pi\sigma_{2y}}$.

Now we want to investigate the change of the slope of the dipole moment of beam 1 when it passes beam 2. For that we let $\Delta z$ describe the shift of center and slope of beam 1 with respect to beam 2. When beam 1 is chosen as origin, then the initial beam distribution is denoted $\rho(\vec{z}_0, 0)$ so that $\rho(\vec{z}_0 - \Delta\vec{z}, 0)$ is the distribution when beam 2 is chosen as origin.

According to equation (1.10) the change of the slope of the dipole moment between the azimuth 0 and $s$ is given by

$$\Delta\vec{d}'(s) = \int_\infty \rho(\vec{z}_0 - \Delta\vec{z}, 0)(\vec{r}'(\vec{M}(\vec{z}_0, s)) - \vec{r}'(\vec{z}_0, 0))d\vec{z}_0 \ . \qquad (1.20)$$

With 0 chosen just before the beam–beam kick and $s$ chosen just after it,

$$\begin{aligned}
\vec{r}'(\vec{M}(\vec{z}_0, s)) &- \vec{r}'(\vec{z}_0, 0) = \Delta\vec{r}'(\vec{z}_0) = -C_{bb}\partial_{\vec{r}_0}U^{\sigma_{2x},\sigma_{2y}}(\vec{r}_0) \ , \qquad (1.21) \\
\Delta\vec{d}' &= -C_{bb}\int_\infty \rho(\vec{z} - \Delta\vec{z}, 0)\partial_{\vec{r}}U^{\sigma_{2x},\sigma_{2y}}(\vec{r})d\vec{z} \\
&= C_{bb}\int_\infty [\partial_{\vec{r}}\rho(\vec{z} - \Delta\vec{z}, 0)]U^{\sigma_{2x},\sigma_{2y}}(\vec{r})d\vec{z} \\
&= -C_{bb}\partial_{\Delta\vec{r}}\int_\infty \rho(\vec{z} - \Delta\vec{z}, 0)U^{\sigma_{2x},\sigma_{2y}}(\vec{r})d\vec{z} \ . \qquad (1.22)
\end{aligned}$$

For a Gaussian beam distribution, the integration over $x'$ and $y'$ can be performed with equation (1.15). Using the convolution equation (1.13) then leads to

$$\begin{aligned}
\Delta\vec{d}' &= -C_{bb}\partial_{\Delta\vec{r}}\int_\infty G^{\sigma_{1x}}(x - \Delta x)G^{\sigma_{1y}}(y - \Delta y)U^{\sigma_{2x},\sigma_{2y}}(\vec{r})dxdy \\
&= -2\pi C_{bb}\partial_{\Delta\vec{r}}\int_0^\infty G^{\sqrt{\Sigma_x^2+t}}(\Delta x)G^{\sqrt{\Sigma_y^2+t}}(\Delta y)dt \ , \qquad (1.23) \\
\Sigma_x &= \sqrt{\sigma_{1x}+\sigma_{2x}} \ , \quad \Sigma_y = \sqrt{\sigma_{1y}+\sigma_{2y}} \ . \qquad (1.24)
\end{aligned}$$

The shift $\Delta\vec{r}$ can be replaced by the dipole moment $\vec{d} = \int_\infty \rho(\vec{z}_0 - \Delta\vec{z})\vec{r}_0 d\vec{z}_0 = \Delta\vec{r}$.

The change in the slope of the dipole moment due to the beam–beam kick for two Gaussian beams is therefore given by

$$\Delta\vec{d}'(s) = -C_{bb}\partial_{\vec{d}}U^{\Sigma_x,\Sigma_y}(\vec{d}) \ . \tag{1.25}$$

This equation is analogous to equation (1.16) and for small oscillation amplitudes of the dipole moment it therefore leads to $\Delta d'_x = C_{bb}\frac{2}{\Sigma_x+\Sigma_y}\frac{d_x}{\Sigma_x}$ which is analogous to equation (1.19).

The coherent tune shifts $\Delta\nu_x$ and $\Delta\nu_y$ are therefore related to the incoherent tune shifts $\xi_x$ and $\xi_y$ by

$$\Delta\nu_x = \xi_x\frac{\sigma_{2x}+\sigma_{2y}}{\Sigma_x+\Sigma_y}\frac{\sigma_{2x}}{\Sigma_x} \ , \quad \Delta\nu_y = \xi_y\frac{\sigma_{2x}+\sigma_{2y}}{\Sigma_x+\Sigma_y}\frac{\sigma_{2y}}{\Sigma_y} \ . \tag{1.26}$$

For matched beams, i.e. for $\sigma_{1x} = \sigma_{2x}$ and $\sigma_{1y} = \sigma_{2y}$, the coherent tune shift is just half of the incoherent tune shift.

### 1.5.2 The Coherent Tune Shift from Hamiltonian Perturbation Theory

When the one turn map without the beam–beam kick is described by the Hamiltonian $H_0(\vec{z})$, then with the beam–beam kick it is described by an added term which is proportional to the beam–beam potential $U^{\sigma_{2x},\sigma_{2y}}(\vec{r})$,

$$H(\vec{z}) = H_0(\vec{z}) + C\cdot U^{\sigma_{2x},\sigma_{2y}}(\vec{r}) \ . \tag{1.27}$$

Let $\underline{A}$ be the transformation matrix to first order normal form coordinates $s_x = \sqrt{J_x}\exp(i\psi_x)$, $s_y = \sqrt{J_y}\exp(i\psi_y)$ of the ring without beam–beam kick. In these coordinates the Hamiltonian is given as

$$H(\vec{J},\vec{\phi}) = H_0(\vec{J}) + C\cdot U^{\sigma_{2x},\sigma_{2y}}(\vec{r}) \ , \quad x = \sqrt{2J_x\beta_x}\cos\phi_x \ , \quad y = \sqrt{2J_y\beta_y}\cos\phi_y \ . \tag{1.28}$$

In first order Hamiltonian perturbation theory the tune shift $\Delta Q_x$ of a particle is given by $\frac{1}{2\pi}\partial_{J_x}$ of the phase average of $H - H_0$,

$$\Delta Q_x = \frac{C}{2\pi}\cdot\partial_{J_x}\oint U^{\sigma_{2x},\sigma_{2y}}(\vec{r})\frac{d\vec{\phi}}{(2\pi)^2} \ . \tag{1.29}$$

A particle with initial normal form coordinate $s_{x0}$ is therefore rotated in phase space after one turn to $s_{x0}\exp(i(Q_x+\Delta Q_x))$. The leading order terms in $x$ and $y$ of the tune shift is the beam–beam parameter

$$\begin{aligned}
\xi_x &= \frac{C}{2\pi}\cdot\partial J_x\int_0^\infty \frac{\oint[1-\frac{(\sqrt{2J_x\beta_x}\cos\phi_x)^2}{2(\sigma_{2x}^2+t)}]\frac{d\phi_x}{2\pi}}{\sqrt{(\sigma_{2x}^2+t)(\sigma_{2y}^2+t)}}dt \\
&= -\frac{C}{2\pi}\cdot\beta_x\int_0^\infty \frac{1}{2\sqrt{(\sigma_{2x}^2+t)^3(\sigma_{2y}^2+t)}}dt \\
&= -\frac{C}{2\pi}\cdot\beta_x\frac{1}{(\sigma_{2x}+\sigma_{2y})\sigma_{2x}} \ .
\end{aligned} \tag{1.30}$$

The last integral over $t$ has already been evaluated in equation (1.19). Comparing with equation (1.19), leads to $C = C_{bb}$.

Given a beam 1 for which the initial shift $\Delta\vec{z}$ with respect to the center of beam 2 corresponds to the normal form coordinate $\Delta s_x$. The horizontal dipole moment in normal form coordinates is initially given by $d_{x0} = \Delta s_x$. After one turn around the ring it is given by $d_{xf} = d_{x0}(1+\Delta d)e^{i2\pi(Q_x+\Delta\nu_x)}$ where the real numbers $\Delta d$ and $\Delta\nu_x$ are a change in oscillation amplitude and in oscillation frequency. For small changes we find $\Delta\nu_x = \frac{1}{2\pi/\Delta s_{x0}}\mathrm{Im}\{e^{-i2\pi Q_x}d_{xf} - d_{x0}\}$ which will be used for the evaluation of

$$\begin{aligned} d_{xf} &= \int_\infty \rho(\vec{z}_0 - \Delta\vec{z}) s_{x0}(\vec{z}_0) e^{i2\pi(Q_x+\Delta Q_x(\vec{z}_0))} d\vec{z}_0 \\ &\approx e^{i2\pi Q_x} \int_\infty \rho(\vec{z}_0 - \Delta\vec{z}) s_{x0}(\vec{z}_0)(1 + i2\pi\Delta Q_x(\vec{z}_0)) d\vec{z}_0 \\ &= e^{i2\pi Q_x}[\Delta s_x + i2\pi \int_\infty \rho(\vec{z} - \Delta\vec{z}) s_x(\vec{z}) \Delta Q_x(\vec{z}) d\vec{z}] \ , \qquad (1.31) \\ \Delta\nu_x &= \frac{1}{\Delta s_x} \int_\infty \rho(\vec{z} - \Delta z) s_x(\vec{z}) \Delta Q_x(\vec{z}) d\vec{z}] \ . \qquad (1.32) \end{aligned}$$

Using equation (1.14) with $J_x = s_x s_x^*$ one thus obtains for small $\Delta s_x$,

$$\begin{aligned} \Delta\nu_x &= \frac{1}{\Delta s_x} \int_\infty \oint \frac{1}{\epsilon_x} e^{-\frac{|s_x - \Delta s_x|^2}{\epsilon_x}} E^{\epsilon_y}(J_y) s_x \Delta Q_x(\vec{J}) \frac{d\vec{\phi}}{(2\pi)^2} d\vec{J} \\ &\approx \frac{1}{\Delta s_x} \int_\infty E^{\epsilon_x}(J_x)(1 + \frac{s_x^*\Delta s_x + s_x \Delta s_x^*}{\epsilon_x}) E^{\epsilon_y}(J_y) s_x \Delta Q_x \frac{d\vec{\phi}}{(2\pi)^2} d\vec{J} \\ &= \int_\infty \frac{|s_x|^2}{\epsilon_x} E^{\epsilon_x}(J_x) E^{\epsilon_y}(J_y) \Delta Q_x(\vec{J}) dJ_x dJ_y \ , \qquad (1.33) \end{aligned}$$

where the integral over $\phi_x$ has eliminated all other terms leaving

$$\Delta\nu_x = -[\partial_\kappa \int_\infty \frac{1}{\epsilon} e^{-\kappa\frac{J_x}{\epsilon_x}} E^{\epsilon_y}(J_y) \Delta Q_x(\vec{J}) d\vec{J}]_{\kappa=1} \ . \qquad (1.34)$$

Now the average over $J_y$ is performed, where equation (1.15) is used for the resulting integral over $y'$,

$$\begin{aligned} \int_\infty E^{\epsilon_y}(J_y) \Delta Q_x(\vec{J}) dJ_y &= \frac{C}{2\pi} \cdot \partial_{J_x} \int_\infty E^{\epsilon_y}(J_y) \oint U^{\sigma_{2x},\sigma_{2y}}(\vec{r}) \frac{d\phi_x}{(2\pi)^2} dy dy' \\ &= \frac{C}{2\pi} \cdot \partial_{J_x} \int_0^\infty \oint \int_\infty G^{\sigma_{1y}}(y) G^{\sqrt{\sigma_{2y}^2+t}}(y) dy G^{\sqrt{\sigma_{2x}^2+t}}(x) d\phi_x dt \\ &= \frac{C}{2\pi} \cdot \partial_{J_x} \int_0^\infty \oint \frac{e^{-\frac{x^2}{2(\sigma_{2x}^2+t)}} - 1}{\sqrt{\sigma_{2x}^2+t}\sqrt{\Sigma_y^2+t}} \frac{d\phi_x}{2\pi} dt \ . \qquad (1.35) \end{aligned}$$

Here again equation (1.13) has been used and the term $-1$, which does not change the result after the derivative $\partial_{J_x}$, has been added to simplify the following partial

integration:

$$\begin{aligned}\Delta\nu_x &= -\frac{C}{2\pi}\cdot[\partial_\kappa\int_\infty\frac{1}{\epsilon_x}e^{-\kappa\frac{J_x}{\epsilon_x}}\partial_{J_x}\int_0^\infty\oint\frac{e^{-\frac{x^2}{2(\sigma_{2x}^2+t)}}-1}{\sqrt{\sigma_{2x}^2+t}\sqrt{\Sigma_y^2+t}}\frac{d\phi_x}{2\pi}dtdJ_x]_{\kappa=1}\\ &= -\frac{C}{2\pi}\cdot[\partial_\kappa\int_\infty\frac{\kappa}{\epsilon_x^2}e^{-\kappa\frac{J_x}{\epsilon_x}}\int_0^\infty\oint\frac{e^{-\frac{x^2}{2(\sigma_{2x}^2+t)}}-1}{\sqrt{\sigma_{2x}^2+t}\sqrt{\Sigma_y^2+t}}\frac{d\phi_x}{2\pi}dtdJ_x]_{\kappa=1}\ . \quad (1.36)\end{aligned}$$

Again equation (1.15) has been used for the integration over $x'$.

$$\begin{aligned}\Delta\nu_x &= -\frac{C}{\sqrt{2\pi}}\cdot[\partial_\kappa\int_0^\infty\int_\infty\frac{1}{\epsilon_x}G^{\frac{\sigma_{1x}}{\sqrt{\kappa}}}(x)\frac{G^{\sqrt{\sigma_{2x}^2+t}}(x)-\frac{1}{\sqrt{2\pi(\sigma_{2x}^2+t)}}}{\sqrt{\Sigma_y^2+t}}dxdt]_{\kappa=1}\\ &= -\frac{C}{2\pi\epsilon_x}\cdot[\partial_\kappa\int_0^\infty(\frac{1}{\sqrt{\sigma_{2x}^2+\sigma_{1x}^2/\kappa+t}\sqrt{\Sigma_y^2+1}}-\frac{1}{\sqrt{\sigma_{2x}^2+t}\sqrt{\Sigma_y^2+1}})dt]_{\kappa=1}\\ &= -\frac{C}{2\pi\epsilon_x}\frac{\sigma_{1x}^2}{2}\cdot\int_0^\infty\frac{1}{\sqrt{\Sigma_x^2+t}^3\sqrt{\Sigma_y^2+t}}dt = -C\frac{2}{\Sigma_x+\Sigma_y}\frac{\beta_x}{4\pi\Sigma_x}\ . \quad (1.37)\end{aligned}$$

The tune shifts $\Delta\nu_x$ and $\Delta\nu_y$ of the dipole moment is again related to the single particle tune shifts $\xi_x$ and $\xi_y$ by

$$\Delta\nu_x = \xi_x\frac{\sigma_{2x}+\sigma_{2y}}{\Sigma_x+\Sigma_y}\frac{\sigma_{2x}}{\Sigma_x}\ ,\quad \Delta\nu_y = \xi_y\frac{\sigma_{2x}+\sigma_{2y}}{\Sigma_x+\Sigma_y}\frac{\sigma_{2y}}{\Sigma_y}\ , \quad (1.38)$$

which is equivalent to equation (1.26). We have therefore derived by two entirely different methods that the coherent beam–beam tune shift for two matched Gaussian beams is half as big as the incoherent beam–beam tune shift.

**Acknowledgments**

We are indebted to S. Levonian, S. Issever, and M. Przybycien for their help in the preparation and analysis of the data taken with H1, HERA-B, and ZEUS respectively.

# 2 Luminosity and Dynamic Aperture of a 72° HERA-e Optics

by G. H. Hoffstaetter, DESY Hamburg

It is planed to reduce the horizontal emittance in HERA from currently 41πnm during the luminosity upgrade to 22πnm [3]. This should be achievable by increasing the RF frequency and the phase advance per FODO cell. The RF frequency should not be increased without an increased phase advance since this would lead to a larger longitudinal emittance and so would reduce our safety margins in the RF bucket size. In addition to reducing the emittance, more phase advance increases the bucket height and makes a shift in the RF frequency possible. These methods are explained in simple terms in [15]. We analyzed several possible optics for the luminosity upgrade lattice with various phase advances in the horizontal and vertical plane of the FODO cells. A lattice with 72° phase advance per FODO cell in both planes turned out to be most promising because it had the most acceptable dynamic aperture [16].
To test the usability of such an optics in the upgraded HERA-e, a 72° test optic was installed in the current ring. Here it will be reported how injection was set up for a shifted frequency. Furthermore, collisions with the proton beam were produced and the luminosity in the test optics was optimized and measured as a function of a joint RF frequency shift in the proton and the electron rings. Dynamic aperture measurements for the 60° and the 72° optics already performed in December 1998 were repeated to shown in which improvements the repair of three electron dipoles has fruited.

## 2.1 Luminosity with Reduced Emittance

Date: 1999, Apr. 26, 3pm to Apr. 27, 9am, Logbook XXXVII, p. 33–39
Date: 1999, Apr. 28, 1am to Apr. 28, 3pm, Logbook XXXVII, p. 41–47

In [17] it is described how the test injection optics with 72° phase advance per FODO cell was installed in the ring and how injection and acceleration was performed. Furthermore, it is illustrated, how the transition from the injection to the test luminosity optics was performed. An additional decrease of the emittance by shifting the RF frequency of the 500MHz RF system of the HERA electron ring was also analyzed during the December 1998 accelerator study period.

On April 28, 1999 an electron beam in the 72° luminosity test optics was brought into collision with the proton beam. The specific luminosity was optimized to $6.6 \cdot 10^{29}\mathrm{cm}^{-2}\mathrm{s}^{-1}\mathrm{mA}^{-2}$ at ZEUS and to $5.5 \cdot 10^{29}\mathrm{cm}^{-2}\mathrm{s}^{-1}\mathrm{mA}^{-2}$ at H1. The average specific luminosity in the two weeks before the accelerator studies was little below $7 \cdot 10^{29}\mathrm{cm}^{-2}\mathrm{s}^{-1}\mathrm{mA}^{-2}$ for a nominal emittance of 41πnm. Measurements during

December 1998 [18] indicate that the frequency of the electron ring is 175Hz lower than the central frequency. Linear optic calculations lead to an rms emittance of $56\pi$nm for this frequency shift. The linear 72° test optics leads to $45\pi$nm. The luminosity $\mathcal{L}$ is reciprocally proportional to $\Sigma_x = \sqrt{\sigma_x^{p2} + \sigma_x^{e2}}$ and $\Sigma_x = \sqrt{\sigma_x^{p2} + \sigma_x^{e2}}$ with the squared one sigma electron and proton beam sizes in the horizontal and vertical plane [19]. We indicate quantities in the present ring with a subscript 0 and denote the relative change of the horizontal and vertical emittance with $\delta$, which keeps the coupling ratio between them constant. The relative change in luminosity is then

$$\frac{\mathcal{L} - \mathcal{L}_0}{\mathcal{L}_0} = \frac{\Sigma_{x0}\Sigma_{y0}}{\sqrt{(\sigma_{x0}^{p2} + \sigma_{x0}^{e2}(1+\delta)^2)(\sigma_{y0}^{p2} + \sigma_{y0}^{e2}(1+\delta)^2)}} - 1 \ . \tag{2.1}$$

If the beams are matched in the present ring, one obtains

$$\mathcal{L} = \frac{2}{1 + (1+\delta)^2}\mathcal{L}_0 \ . \tag{2.2}$$

A 22% increase of the specific luminosity of $8.5 \cdot 10^{29}\mathrm{cm}^{-2}\mathrm{s}^{-1}\mathrm{mA}^{-2}$ was therefore expected. The too low specific luminosity measured for the 72° optics for ZEUS might be related to a unusually increased proton emittance, since the proton beam had been filled about 12 hours earlier and since the proton beam had experienced one electron ramp which lead to electron beam loss before luminosity was established. Furthermore, the proton beam had been excited by a transverse kicker for the coasting beam excitation described in section 12. On the other hand, the wire scanner was used just before optimizing luminosity and yielded $\epsilon_x = 21.2\pi$mm mrad and $\epsilon_y = 15.0\pi$mm mrad, which is not very unusual. Freshly accelerated proton beams for example resulted in $\epsilon_x = 19.8\pi$mm mrad and $\epsilon_y = 15.3\pi$mm mrad on May 1 and $\epsilon_x = 17.8\pi$mm mrad on April 29.

It is not understood why the Luminosity at H1 could not be optimized to the same value as at ZEUS. A similar effect, leading to lower luminosity at H1 than at ZEUS, is often observed during normal luminosity operation of HERA. But the difference in luminosity is usually much smaller.

In [20] we have also presented different measurements of the electron emittance to establish the emittance decrease with RF frequency and the emittance decrease with more phase advance per FODO cell. The spot size of the synchrotron light monitor showed a reduction in good agreement with theory, whereas the divergence of bremsstrahlung measured at the luminosity monitors of H1 and ZEUS did not reflect the required emittance reduction by a big margin. The change in luminosity with an increase of the RF frequency was therefore used in April 1999 as a third way of measuring the decrease of the emittance in order to determine which of the two previous measurements is correct.

While the nominal frequency of the electron RF system was shifted, the synchronization loop simultaneously shifted the frequencies of both proton RF systems. However, one has to adjust the nominal frequency of the proton 208MHz RF system before a too large difference to the frequency of the electron RF system disturbs

the synchronization loop. The following procedure turned out to be usable: alternating we increased the 500MHz electron RF frequency by 24Hz and the 208MHz RF frequency by 10Hz. The frequency of the proton rings 52MHz RF system is automatically adjusted to the 208MHz system.

The resulting relative increase in luminosity at H1 and ZEUS is shown in figure 2.1 (left). The agreement is remarkably good. This establishes that the decrease in emittance measured by the synchrotron light spot is trustworthy whereas the emittance deduces from the luminosity monitors was incorrect during the December 1999 accelerator studies. Therefore the observed increase in luminosity is an independent check that the emittance reduction with increased RF frequency can be used as predicted by theory. Furthermore this measurement is an independent verification of the previously measured frequency shift of 175Hz below the center frequency. Figure 2.1 (right) shows that the agreement between theory and measured luminosity increase would be much worse if the electron RF frequency was matched to the length of the path through the quadrupoles centers.

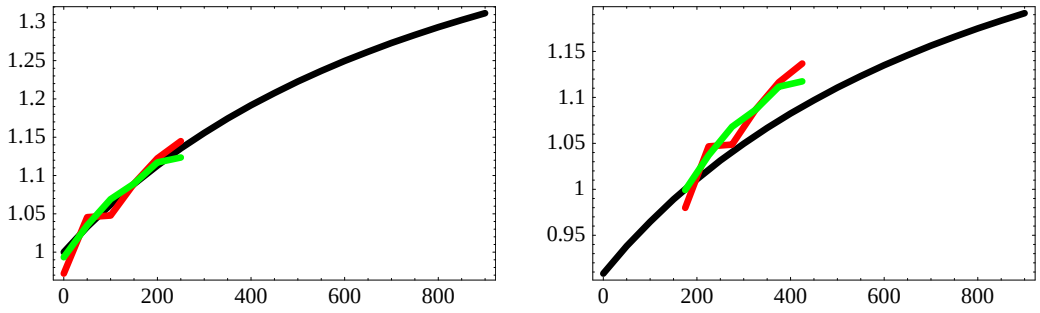


**Figure 2.1**: Relative increase of luminosity with increasing RF frequency in the 500MHz electron RF system for ZEUS (red), H1 (green), and simulated (black). Left: The simulation assumed the electron RF frequency to be 175Hz below the center frequency. Right: The simulation assumed the electron RF frequency to be the center frequency.

## 2.2 Measurement of Dynamic Aperture

Date: 1999, June 20, 11pm to June 21, 3pm, Logbook XXXVII, p. 105–107
Date: 1999, June 28, 3pm to June 29, 7pm, Logbook XXXVII, p. 154–163
Date: 1999, July 3, 3pm to July 3, 11pm, Logbook XXXVII, p. 197–199

The dynamic aperture of the 72° test luminosity optics has been measured and compared to the dynamic aperture of the present 60° optics during the December 1998 HERA accelerator studies. We reported $7.9\sigma$ dynamic aperture for the present 60° luminosity optics and $8.1\sigma$ dynamic aperture for the 72° luminosity test optics at 27.5GeV [17]. In February 1999 shortages to ground at three dipole magnets of the electron ring were found and repaired. After this repair, the average transfer efficiency from PETRA to HERA was improved very noticeably, indicating that the dynamic aperture has been increased. In April 1999 it was therefore re-measured.

For the measurement, the beam was kicked by an angle $\Theta$, which lets the central particles subsequently travel with a Courant Snyder invariant $\beta_k\Theta^2$, where $\beta_k$ is the beta function at the kicker. When the central particles are kicked to a Courant Snyder invariant which corresponds to the dynamic aperture $DA$, then approximately half of the beam distribution will be outside the dynamic aperture and half will be inside. Therefore, the beam was kicked with the fourth injection kicker to various amplitudes and the relative beam loss was measured. The voltage of kicker 4 and the resulting beam current reduction are shown in the figures 2.2 to 2.4 for the current 60° injection optics, for the current 60° luminosity optics, and for the 72° test optics. These data points were now interpolated to extrapolate the kicker voltage $V_2$ at which half the beam is lost. The kicker leads to 0.256mrad per kV voltage at an Energy of 12GeV. The corresponding kick $\Theta_2$ and the dynamic aperture $DA$ are therefore computed by

$$\Theta_2 = \frac{V_2}{\mathrm{kV}}\frac{12GeV}{E}\cdot 0.256\mathrm{mrad}\ , \quad DA = \beta_k\Theta_2^2\ , \quad DA_{rel} = \sqrt{\frac{DA}{\varepsilon}}\ . \tag{2.3}$$

For the 60° injection optics the beta function at the kicker 4 is $\beta_k = 35.9$m, for the 60° luminosity optics it is $\beta_k = 27.8$m and for the 72° test luminosity optics it is $\beta_k = 34.6$m. The relative dynamic aperture $DA_{rel}$ is an even more relevant quantity, since it describes how many sigma of the beam distribution fit into the dynamic aperture. To make comparison easier, the dynamic aperture of the current injection optics at 12GeV was computed relative to the nominal emittance of the current luminosity optics at high energy, which is 41$\pi$nm. The nominal emittance of the 72° test luminosity optics is 34$\pi$nm without a frequency shift and 22$\pi$nm after a frequency shift of 300Hz. The measurements shown in the figures 2.2 to 2.4 lead to the following dynamic apertures:

| Optics | Date | $V_2$ | $DA$ | $DA_{rel}$ | RF shift |
|---|---|---|---|---|---|
| 60° injection | 20 Jun.1999 | 1.55kV | 6.7$\pi$mm mrad | 12.1$\sigma$ | 0Hz |
| 60° injection | 20 Jun.1999 | 1.53kV | 5.7$\pi$mm mrad | 12.0$\sigma$ | 0Hz |
| 60° injection | 20 Jun.1999 | 1.53kV | 5.7$\pi$mm mrad | 12.0$\sigma$ | 0Hz |
| 60° injection | 20 Jun.1999 | 1.69kV | 7.7$\pi$mm mrad | 13.2$\sigma$ | 0Hz |
| 60° luminosity | 3 Jul.1999 | >3.50kV | $>$ 4.4$\pi$mm mrad | $>$ 10.3$\sigma$ | 0Hz |
| 60° luminosity | 3 Jul.1999 | >3.50kV | $>$ 4.4$\pi$mm mrad | $>$ 10.3$\sigma$ | 0Hz |
| 60° luminosity | 3 Jul.1999 | >3.50kV | $>$ 4.4$\pi$mm mrad | $>$ 10.3$\sigma$ | 0Hz |
| 72° luminosity | 3 Jul.1999 | 2.70kV | 3.4$\pi$mm mrad | 10.0$\sigma$ | 0Hz |
| 72° luminosity | 3 Jul.1999 | 2.76kV | 3.5$\pi$mm mrad | 10.2$\sigma$ | 0Hz |
| 72° luminosity | 3 Jul.1999 | 2.66kV | 3.3$\pi$mm mrad | 9.8$\sigma$ | 0Hz |
| 72° luminosity | 3 Jul.1999 | 2.77kV | 3.6$\pi$mm mrad | 12.7$\sigma$ | 300Hz |
| 72° luminosity | 3 Jul.1999 | 2.74kV | 3.5$\pi$mm mrad | 12.6$\sigma$ | 300Hz |
| 72° luminosity | 3 Jul.1999 | 2.82kV | 3.7$\pi$mm mrad | 10.4$\sigma$ | 0Hz |

The dynamic aperture for the 60° optics was so large that it could not be measure with the maximal voltage of 3kV for kicker 4. The measurements should be repeated while using kicker 2 and 3 simultaneously. Here we have used the data shown in

figure 2.3 to formulate a plausible lower limit on the dynamic aperture. The dynamic aperture was not noticeably reduced when the Rf frequency was shifted by 300Hz. Since the nominal emittance deceased, the relative dynamic aperture in the 72° test optics is as large as in the 60° injection optic.

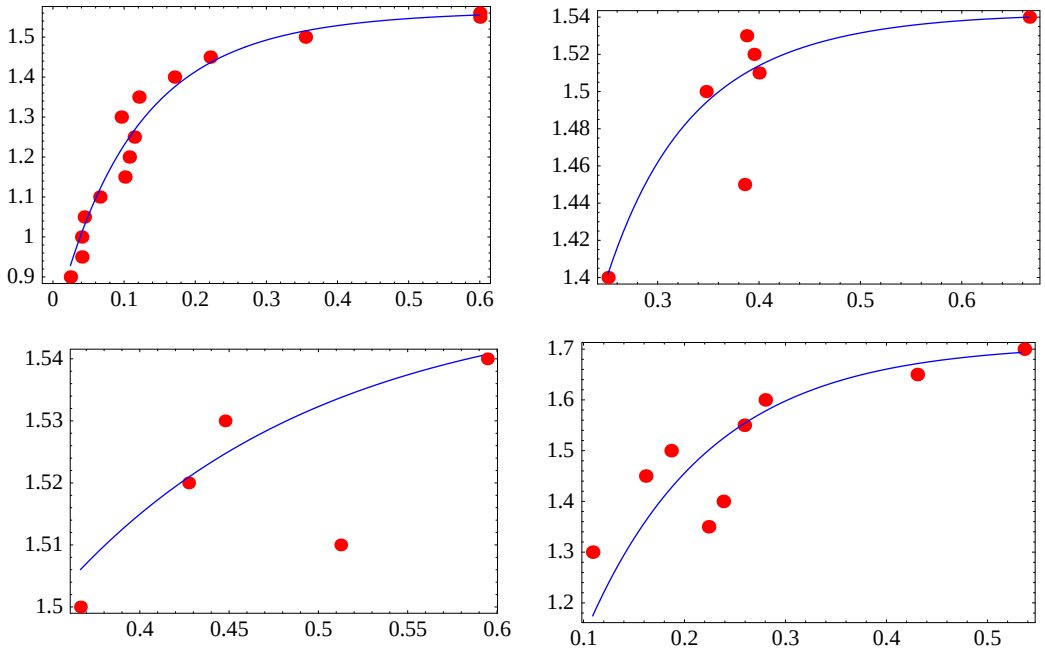


**Figure 2.2**: Kicker voltage as a function of the fraction of particles that are kicked out of the beam in the 60° injection optics at 12GeV. (These data were taken by B. Holzer, Logbook XXXVII pages 105–107.)

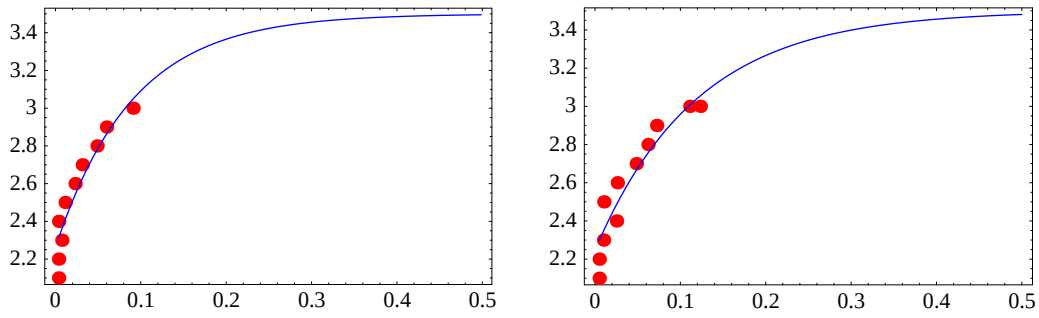


**Figure 2.3**: Kicker voltage as a function of the fraction of particles that are kicked out of the beam in the 60° luminosity optics.

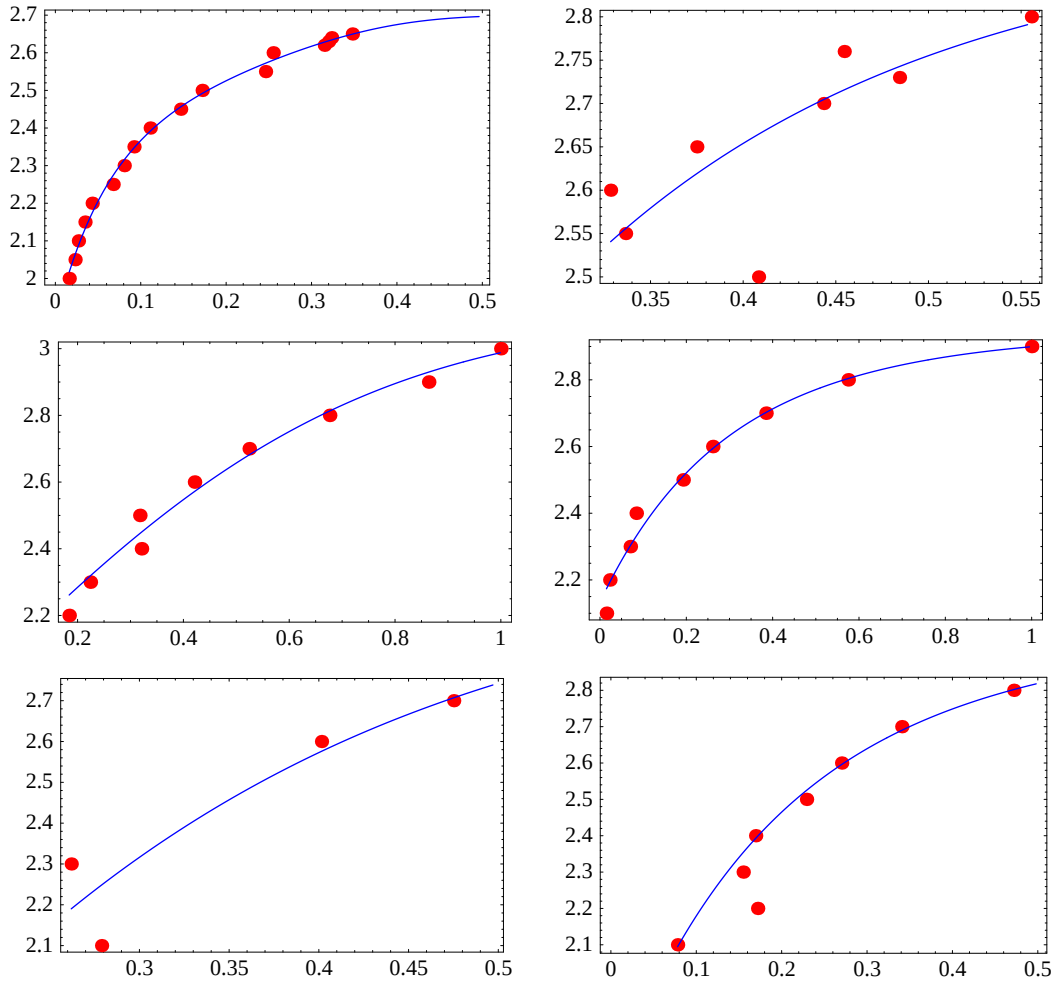


**Figure 2.4**: Kicker voltage as a function of the fraction of particles that are kicked out of the beam in the 60° optics.

# 3 Tail Scan Experiments I at HERA–e

by A. Meseck, DESY Hamburg

Date: 1999, Apr. 6, 11pm to April 7, 3am, Logbook XXXVI, p. 209–213
Date: 1999, June 28, 3pm to 5pm, Logbook XXXVII, p. 154
Date: 1999, June 29, 7pm to June 30, 5am, Logbook XXXVII, p. 164–165
Date: 1999, July 4, 10am to 12am, Logbook XXXVII, p. 201–202

In order to protect the H1 detector and the ZEUS detector from synchrotron radiation and particle background, knowledge of the transverse dimension of the lepton distribution is necessary. The tails of the distribution are important, because they emit strong synchrotron radiation.
Tail scraping experiments allow us to study the tails of the distribution. A scraper is moved closer to the beam in steps and at each step the lifetime of the beam and the loss rate are measured. With such a tail scan it is possible to obtain information about particles, which are at an amplitude larger than the position of the scraper.
Because of the present background in the experiments and with regard to the luminosity upgrade project, where the synchrotron radiation becomes more important, the following measurements were carried out:

- horizontal and vertical tail scraping on a 27.5GeV positron beam, where the proton ring had luminosity condition but the protons were not filled (no beam-beam interaction)
- horizontal and vertical tail scraping on a 27.5GeV positron beam, where the upgrade focusing scheme of 72° per FODO cell in the arcs was used. In this case the proton ring had luminosity condition but again without proton filling.

## 3.1 Measurements

The tail scan experiments were taken on June 28*nd* and 29*nd* and on July 3*rd* in 1999.

During the last shut down two scrapers were installed in the HERA electron ring (HERA–e). They make it possible to take scraping measurements at the positron beam. The scrapers are installed in the east section 35m right of the IP in a region with negligible dispersion. Each of the scrapers has a horizontal and a vertical scraper jaw. So that it is possible to scrape the beam from above, below, the right side, and the left side. The scraper jaws could be moved from BKR via mouse click in steps of 0.1mm or 0.01mm respectively. The distance between both scrapers amounts to 40mm.

The beam loss rates in HERA are measured by Beam Loss Monitors (BLMs). Two of them, $OR31C$ and $OR32C$, were installed next to the scrapers during the last shut down. Those two BLMs have different sensitivity and are dedicated to the scraping experiments. The nearest regular HERA–e BLM, $OR44$, has a distance of 10m from the scrapers. The beam current losses are used to determine the beam lifetime for HERA.

For each Measurement the date, the time, the beam lifetime, the beam current, the scraper position, and the data of the BLMs were recorded in a separate file.

Figure 3.1 shows the beam loss rates of several BLMs as a function of the horizontal scraper position for a 27.5GeV positron beam with regular luminosity conditions but without the proton fill. Figure 3.2 shows the loss rates of several BLMs as a function of the vertical scraper position for the same case. The results of the measurements with the upgrade focusing scheme in the arcs are shown in the figure 3.3 and figure 3.4.

### 3.1.1 Efficiency of the Beam Loss Monitors

During the tail scan experiments the scraper was moved until lifetimes of the order of one hour were reached. In this region the beam lifetime is determined by the losses on the scraper. The beam current as well as the time and the data of the BLMs can be used to calculate the efficiency for detecting a lost positron (see table 3.1). In this calculations the background in the monitors caused by the synchrotron radiation and the beam gas scattering is taken into the account by using the following formula:

$$N_{DPLP} = \frac{NBLM - NBLM_0}{NI - NI_0} \ , \tag{3.1}$$

where $N_{DPLP}$ is the detected particles per lost particles, $NBLM$ is the measured loss rate of the BLMs with the tail scan at the lifetime of one hour , $NBLM_0$ is the measured loss rate of the BLMs without the tail scan, $NI$ is the total loss rate obtain from beam current measurement at the lifetime of one hour, and $NI_0$ is the total loss rate without the tail scan.

| Scraper Position | Monitor OR44 | Monitor OR32C | Monitor OR31C |
|---|---|---|---|
| Outside | $3.9 * 10^{-5}$ | $3.2 * 10^{-6}$ | $2.6 * 10^{-7}$ |
| Inside | $3.6 * 10^{-5}$ | $3.2 * 10^{-6}$ | $2.6 * 10^{-7}$ |
| Top | $4.5 * 10^{-5}$ | $6.8 * 10^{-6}$ | $4.1 * 10^{-7}$ |
| Bottom | $4.0 * 10^{-5}$ | $4.4 * 10^{-6}$ | $2.1 * 10^{-7}$ |

**Table 3.1**: Detected particles per lost particles.

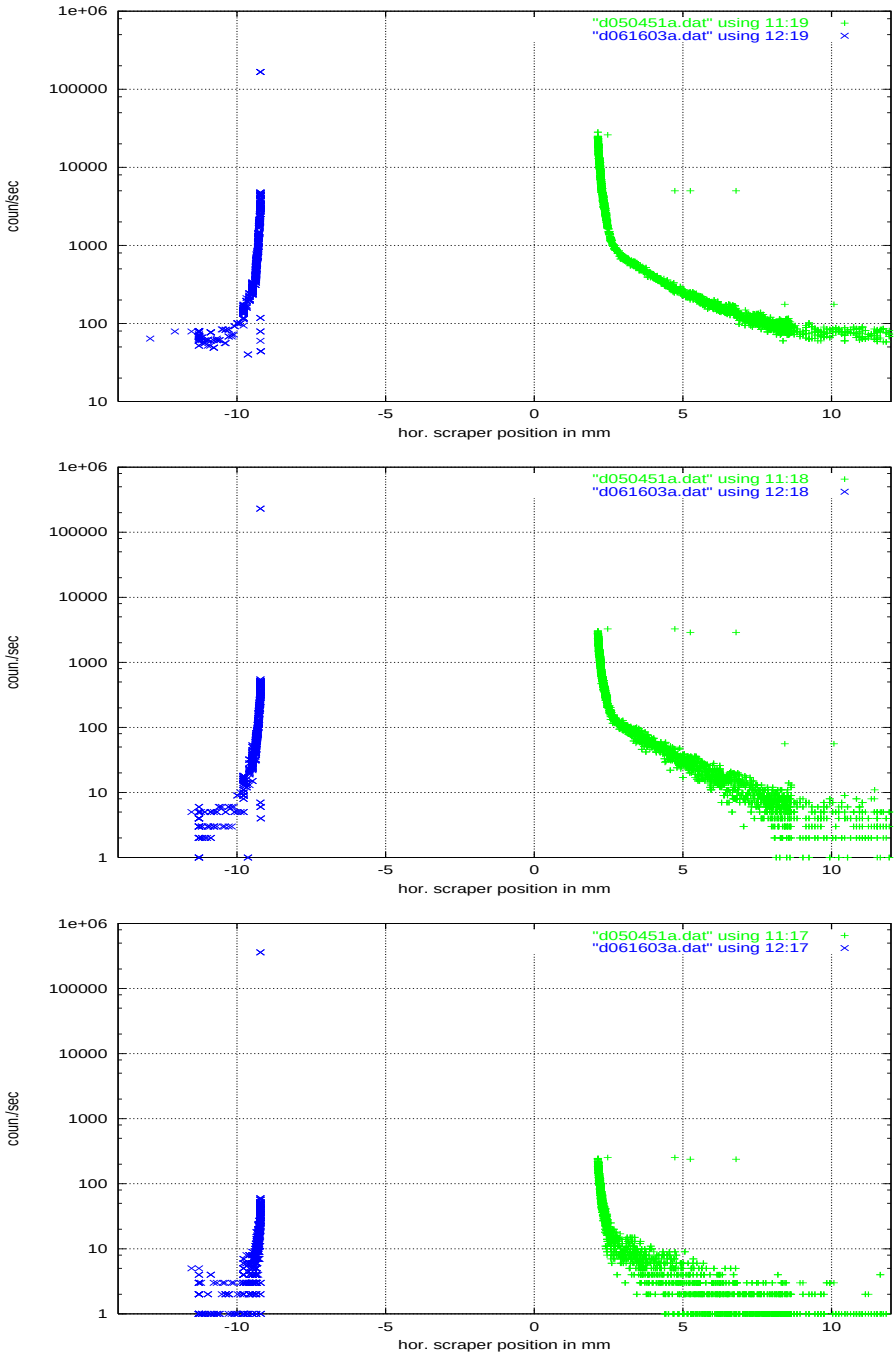


**Figure 3.1**: Beam loss rates versus horizontal scraper position, with regular focusing scheme; top: monitor $OR44$, middle: monitor $OR32C$, bottom: monitor $OR31C$.

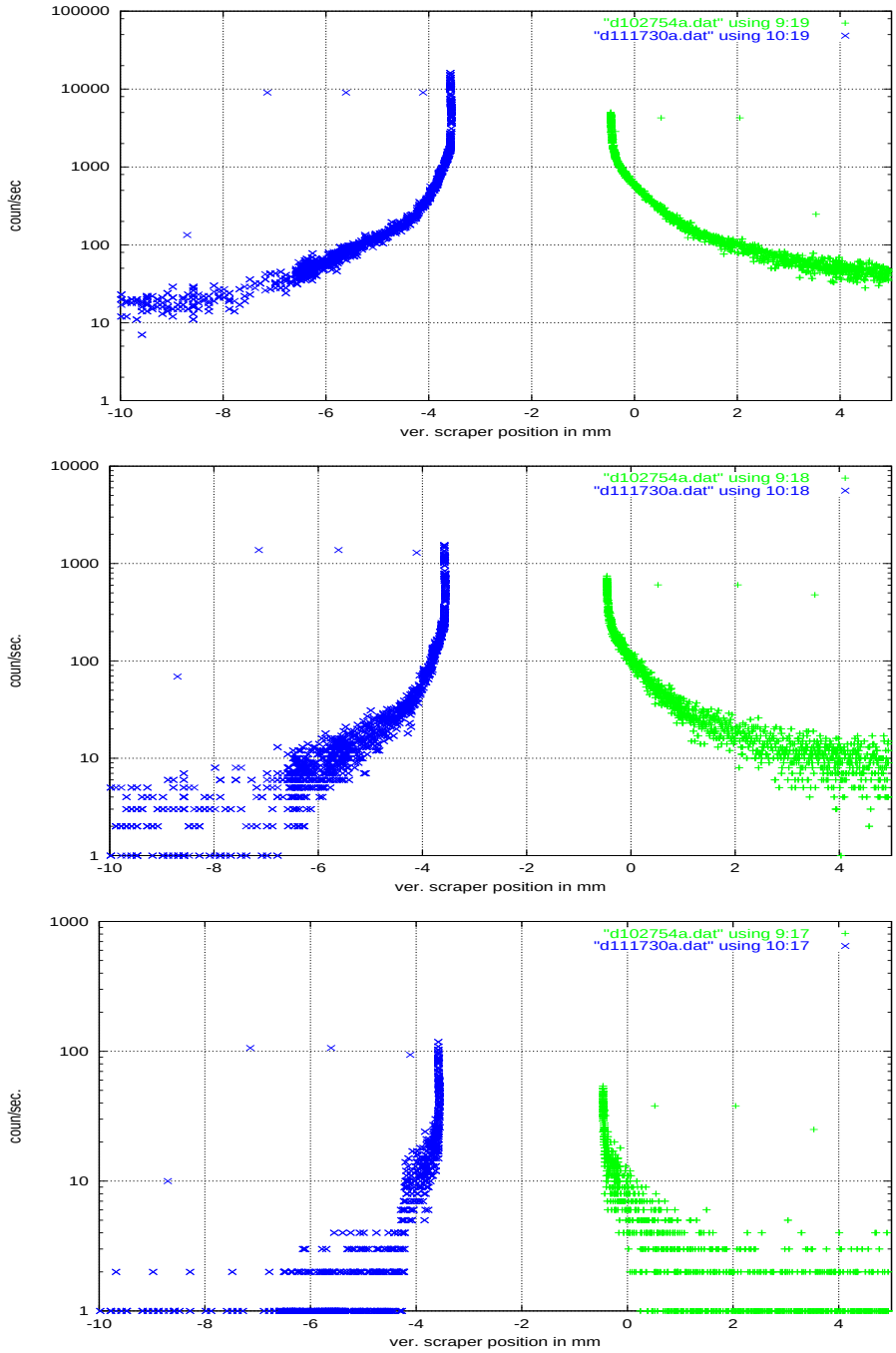


**Figure 3.2**: Beam loss rates versus vertical scraper position,with regular focusing scheme; top: monitor $OR44$, middle: monitor $OR32C$, bottom: monitor $OR31C$.

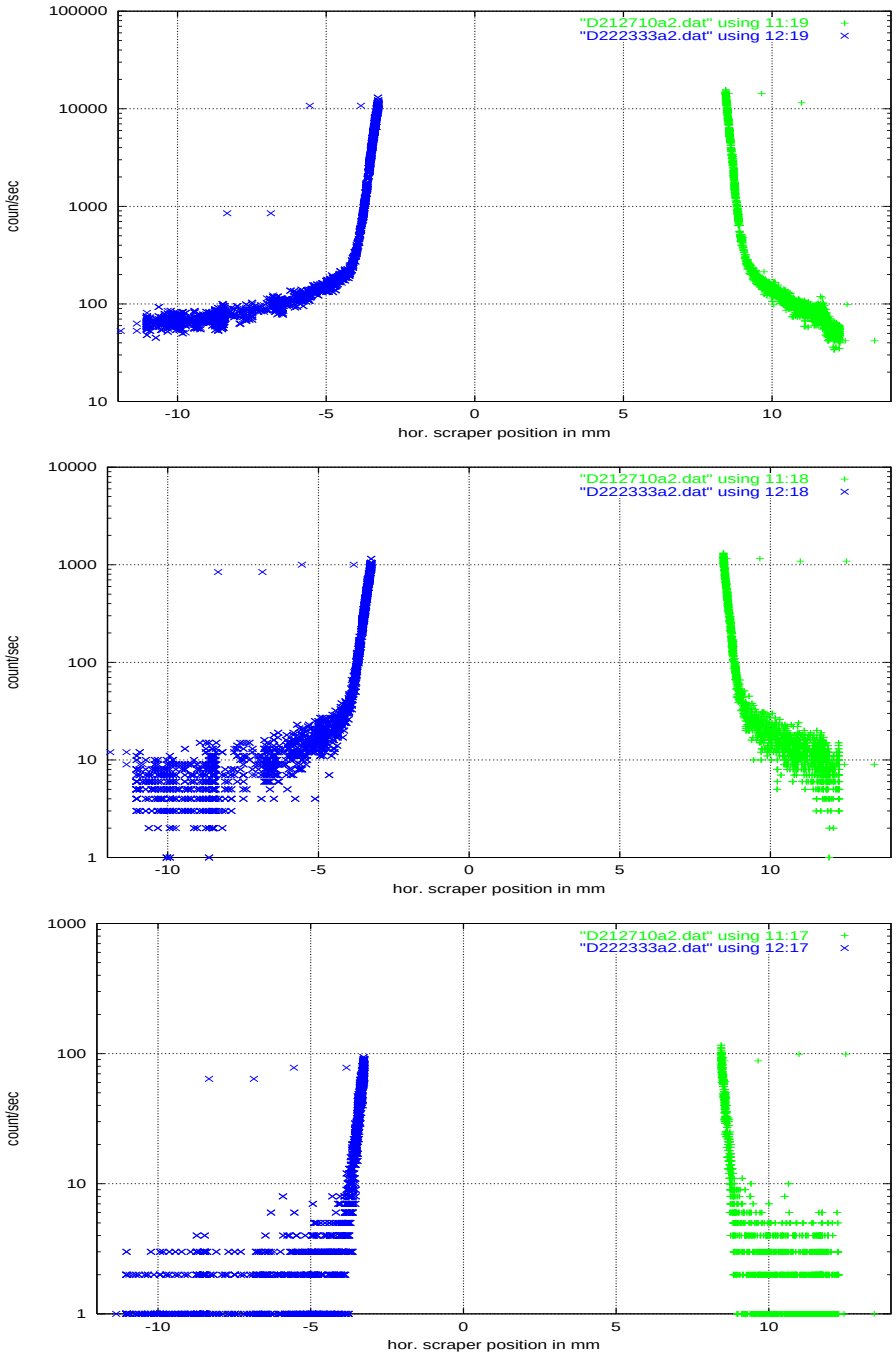


**Figure 3.3**: Beam loss rates versus horizontal scraper position,with upgrade focusing scheme; top: monitor $OR44$, middle: monitor $OR32C$, bottom: monitor $OR31C$.

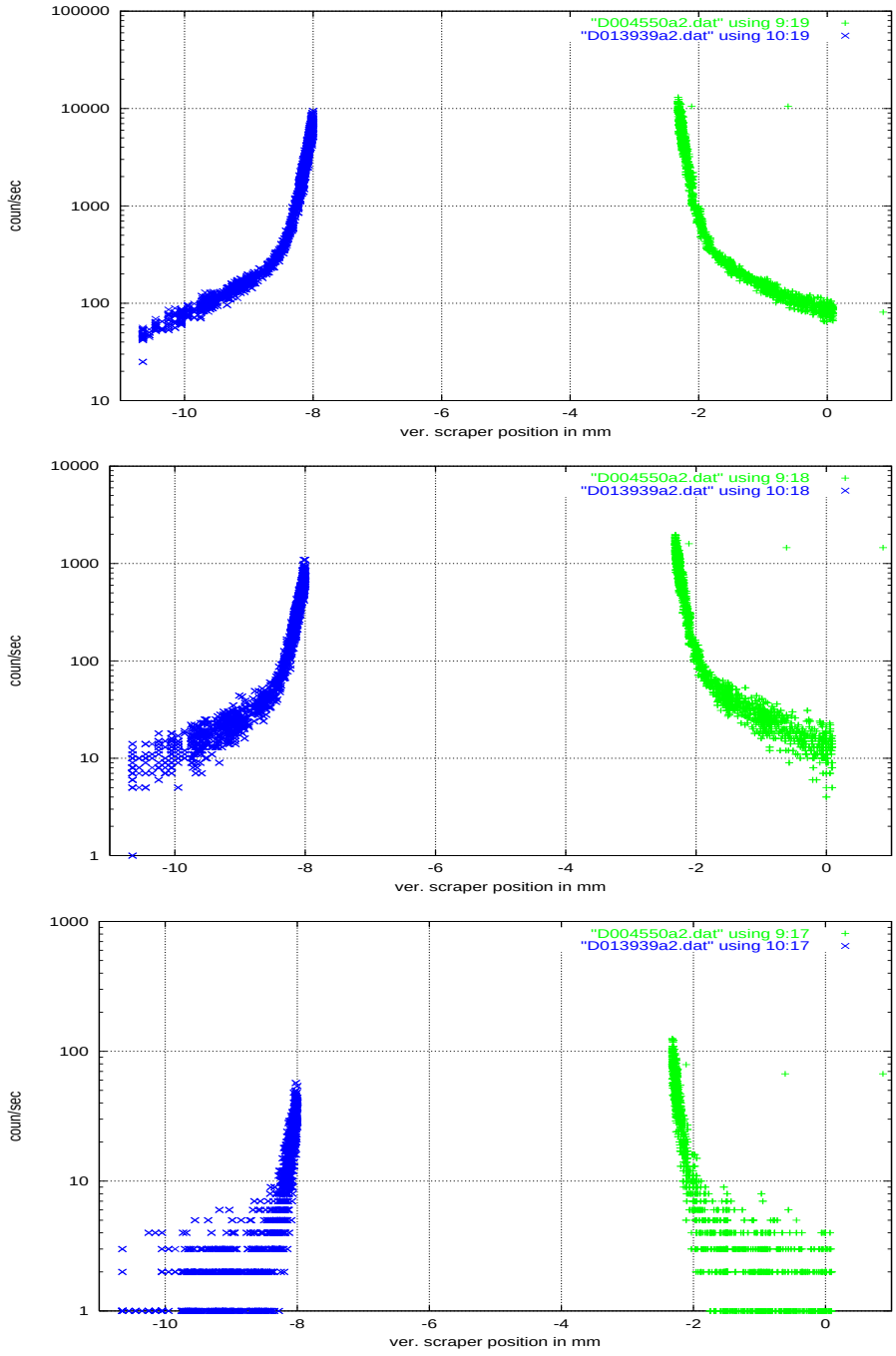


**Figure 3.4**: Beam loss rates versus vertical scraper position,with upgrade focusing scheme; top: monitor $OR44$, middle: monitor $OR32C$, bottom: monitor $OR31C$.

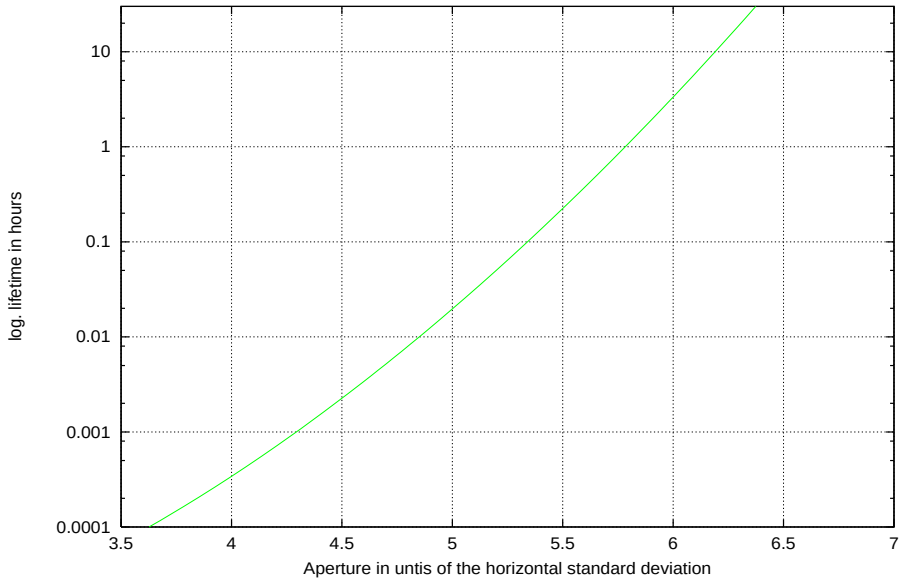


**Figure 3.5**: Upgrade Focusing Scheme.

## 3.2 Evaluation

During the tail scan experiments the physical aperture was reduced by moving the scrapers gradually. The measurements were taken until lifetimes of the order of one hour were reached, as mentioned in the last section. In this region the core of the transverse beam distribution is scraped. Assuming that the core of the distribution is Gaussian, as we would expect from the previous measurements [21], the beam lifetime and the scraper position, which corresponds to the physical aperture, can be used to calculate the standard deviation of the transverse beam distribution. The connection between the beam lifetime $\tau_{qz}$, the transverse aperture $z$, and the standard deviation of the transverse beam distribution $\sigma_z$ is given by [22]:

$$\tau_{qz} = \frac{\tau_z}{2} \frac{e^{\frac{z^2}{2\sigma_z^2}}}{\frac{z^2}{\sigma_z^2}} \ , \tag{3.2}$$

where $z = x, y$, and the $\tau_z$ is the corresponding transverse damping time. Using the above formula, the lifetime as a function of the aperture in units of the standard deviation can be plotted. Such a plot is shown in figure 3.5.

Form figure 3.5 is concluded that in the case of the upgrade focusing scheme in the arcs a lifetime of one hour corresponds to a horizontal aperture of $5.76\sigma_x$. The standard deviation of the horizontal beam distribution $\sigma_x$ can be calculated by comparing this value with the corresponding measured scraper position of 8.44mm or $-3.25$mm respectively (see figure 3.8):

$$2 \cdot 5.65\sigma_x = (|-3.25| + 8.44)\text{mm} \Longrightarrow \sigma_x = 1.035\text{mm} \ . \tag{3.3}$$

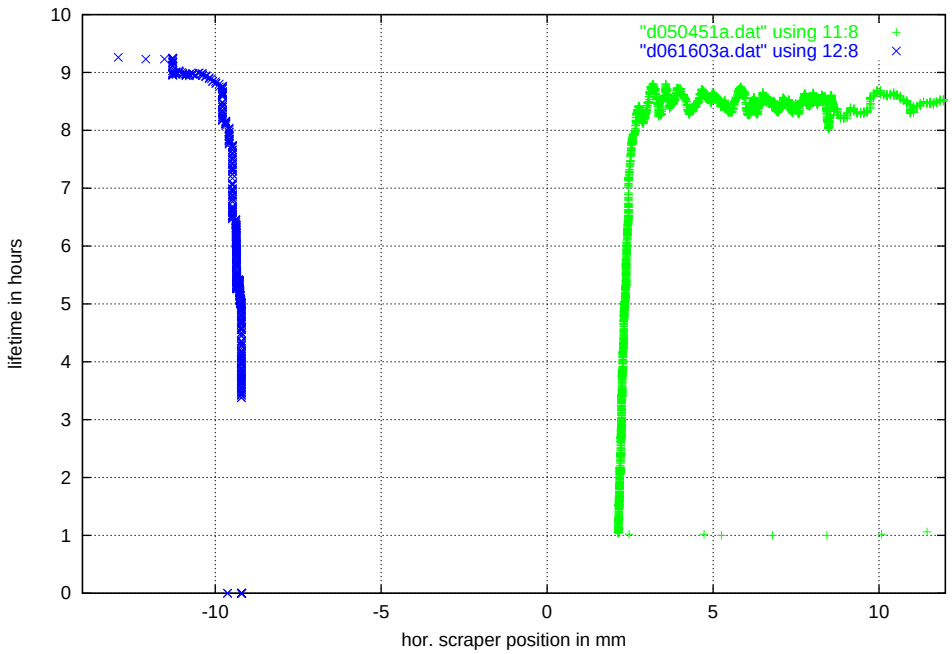


**Figure 3.6**: Lifetime versus horizontal scraper position, with regular focusing scheme.

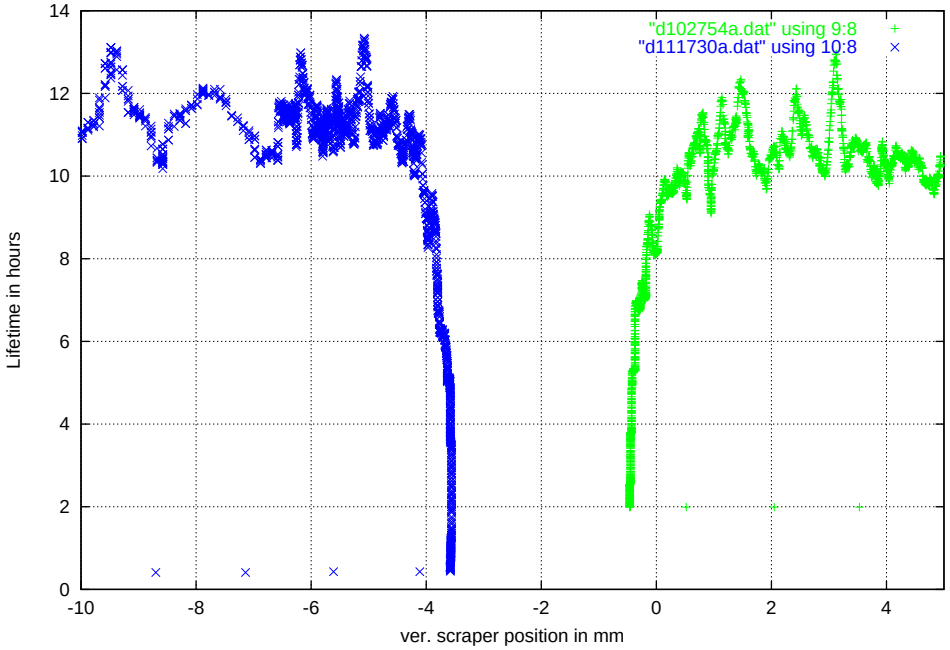


**Figure 3.7**: Lifetime versus vertical scraper position, with regular focusing scheme.

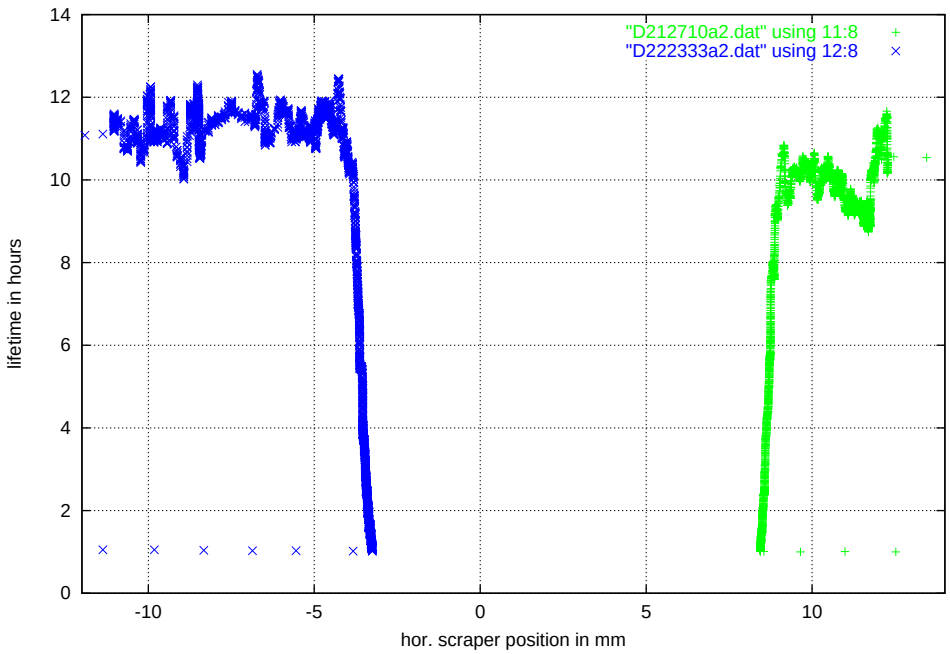


**Figure 3.8**: Lifetime versus horizontal scraper position, with upgrade focusing scheme.

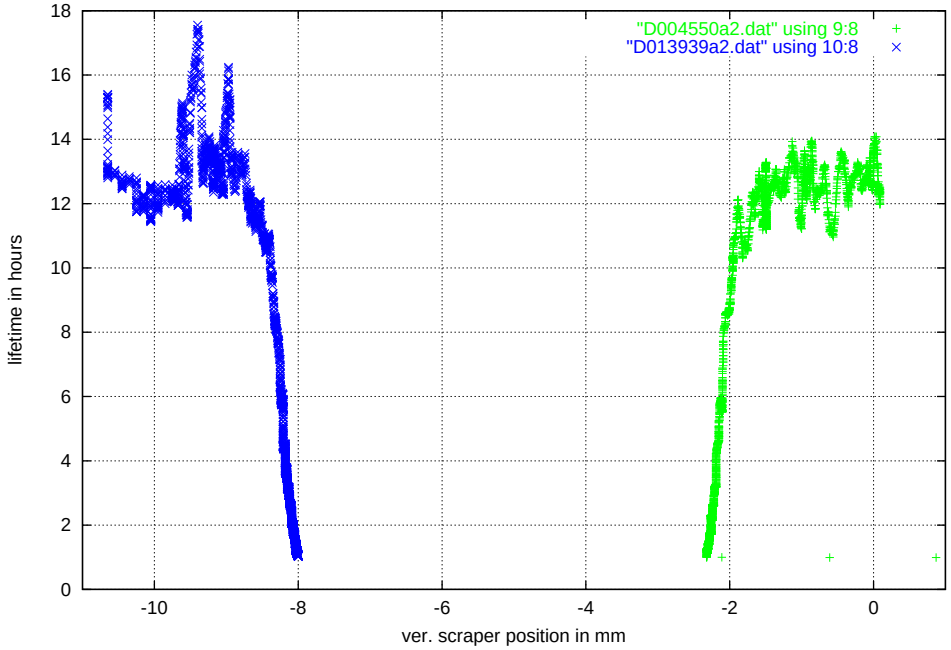


**Figure 3.9**: Lifetime versus vertical scraper position,with upgrade focusing scheme.

| | $\sigma_x$ with regular focusing scheme | $\sigma_y$ with regular focusing scheme | $\sigma_x$ with upgrade focusing scheme | $\sigma_y$ with upgrade focusing scheme |
|---|---|---|---|---|
| theoretical | 0.850mm | - | 0.657mm | - |
| measured | 0.977mm | 0.268mm | 1.035mm | 0.502mm |

**Table 3.2**: The theoretical and measured standard deviation of the transverse beam distribution.

In this way the standard deviation of the horizontal and vertical beam distribution with the regular and the upgrade focusing scheme can be calculated. The table 3.2 gives the measured and theoretical standard deviations. The theoretical values for the standard deviation of the horizontal distribution are simulated by the program PETROS.

In the case of the regular focusing scheme the measured horizontal standard deviation agrees well with the simulated value. In the case of the upgrade focusing scheme the measured horizontal standard deviation is larger than the simulated value by a factor 1.5. Problems with the tune controller and bad closed orbit could cause this large discrepancy.

Due to quantum excitation there is a continuous flow of particles from the beam core into the tails and back by damping toward the core. If there were no nonlinear forces and no aperture, theoretically the particle distribution under influence of damping and statistical fluctuation would be a Gaussian distribution. In a real storage ring like HERA we expect Non-Gaussian tails of the distribution caused by nonlinear components of the magnetic fields and the beam-beam interaction.

A reduction of the aperture, what happens during the scraping measurements gradually, absorbs all particles which reach occasionally large amplitudes due to the emission of a high energy photon. In order to explain the tail scan experiments, it is therefore useful to simulate the tails under suitable conditions. This will be done next time. Further tail scan experiments for a 27.5GeV positron beam with beam-beam interaction should be taken to complete this and the previous measurements, where lifetimes of the order of 0.1 hour were reached by bumps.[2].

## Acknowledgments

I would like to thank the colleagues, which made the tail scan experiments possible: B. Sarau for the installation of the Scrapers, K. Wittenburg for the installation of the BLMs and M. Lomperski for his program, which writes the measured data to separate files.

# 4 Tail Scan Experiments II at HERA–e

by A. Meseck, DESY Hamburg

Date: 1999, Dec. 12, 11pm to Dec. 12 7am Logbook XXXXI, p. 73–74

In order to complete the tail scan experiments from June and July in 1999, additional tail scraping measurements at HERA–e were carried out in October and in December in 1999. The data without proton filling had to be taken again, because of the bad closed orbit and the problems with tune controller during the measurements in June and July, as mentioned in section 3.

## 4.1 Introduction

In operation of HERA–e, protection of the H1 detector and the ZEUS detector from the synchrotron radiation caused by the lepton beam is necessary. The transverse dimension of the synchrotron radiation fan depends on the transverse dimension of the lepton distribution. The tails of the lepton distribution causes the edge of the radiation fan. Therefore they are important.

It is possible to obtain information about the tails by tail scan experiments. During such a tail scan experiment, the physical aperture is reduced by moving a scraper toward the beam in steps. At each step the beam lifetime and the loss rate are measured.

At the present HERA electron ring, where the focusing scheme of 60° per FODO cell in the arcs is used, the following tail scan measurements were carried out:

- horizontal and vertical tail scan measurements on a 27.5 GeV positron beam under regular luminosity conditions, i.e. with beam-beam interaction, on October 8th.

- horizontal tail scan on a 27.5 GeV positron beam on December 19th, where the magnets of the proton ring had luminosity conditions but the protons were not filled, i.e. without beam-beam interaction.

With regard to the luminosity upgrade project, tail scan experiments were carried out in two cases, where the upgrade focusing scheme of 72° per FODO cell in the arcs was used:

- horizontal and vertical tail scraping on a 27.5GeV positron beam under luminosity conditions, i.e. with beam-beam interaction, on December 16th.

- horizontal and vertical tail scraping on a 27.5GeV positron beam on December 19th. In this case the magnets of the proton ring had luminosity conditions but the protons were not filled, i.e. no beam-beam interaction.

## 4.2 Measurements

The scrapers, which are installed in the East section 35m right of the IP in a region with negligible dispersion, were moved by remote control from the BKR in steps of 0.1mm or 0.01mm respectively.

During the experiments the beam loss rates were measured by the Beam Loss Monitors (BLMs) as described in section 3: $OR31C$ and $OR32C$, which are installed next to the scrapers and have different sensitivity, and by $OR44$, which is the nearest regular HERA–e BLM and has a distance of 10m from the scrapers.

The beam current measurement is used to determine the beam lifetime for HERA. For each Measurement the date, the time, the beam lifetime, the beam current, the scraper position, and the data of the BLMs were recorded.

The beam loss rates as a function of the horizontal and vertical scraper positions for a 27.5GeV positron beam under the regular luminosity condition are shown in figure 4.1. Figure 4.2 shows it for the upgrade focusing scheme. The results of the measurements without beam-beam interaction are shown in the figure 4.3 and figure 4.4.

## 4.3 Evaluation

During the tail scan experiments the physical aperture is reduced by moving the scrapers gradually. The measurements were taken until lifetimes of the order of one hour were reached. If there were no nonlinear forces, no beam-gas scattering, and no aperture, theoretically the particle distribution under influence of damping and statistical fluctuation would be a Gaussian distribution. Assuming that the core of the distribution is Gaussian, as we would expect from the measurements in 1998 [21], the beam lifetime and the scraper position, which corresponds to the physical aperture, can be used to calculate the standard deviation of the transverse beam distribution. The connection between the beam lifetime $\tau_{qz}$, the transverse aperture $z$, and the standard deviation of the transverse beam distribution $\sigma_z$ is given by [22]:

$$\tau_{qz} = \frac{\tau_z}{2} \frac{e^{\frac{z^2}{2\sigma_z^2}}}{\frac{z^2}{2\sigma_z^2}}, \tag{4.1}$$

if there is no dispersion at the location of the scraper.

The variable $z$ can be either $x$ or $y$ for horizontal or vertical scraping and $\tau_z$ is the corresponding transverse damping time, where $\tau_x = 1.43 \cdot 10^{-2}$sec and $\tau_y = 1.33 \cdot 10^{-2}$sec for the regular and the upgrade focussing scheme. These values were computed for the center frequency of the RF system and were used in the following calculations. When the frequency is 154Hz lowere, one computes $\tau_x = 1.75 \cdot 10^{-2}$sec and $\tau_y = 1.33 \cdot 10^{-2}$sec.

Using the above formula, the lifetime as a function of the aperture in untis of the standard deviation can be plotted. Such a plot is shown in figure 4.5.

Form figure 4.5 it is concluded that in the case of the regular focussing scheme in the arcs a lifetime of two hour corresponds to a horizontal aperture of $5.77\sigma_x$.

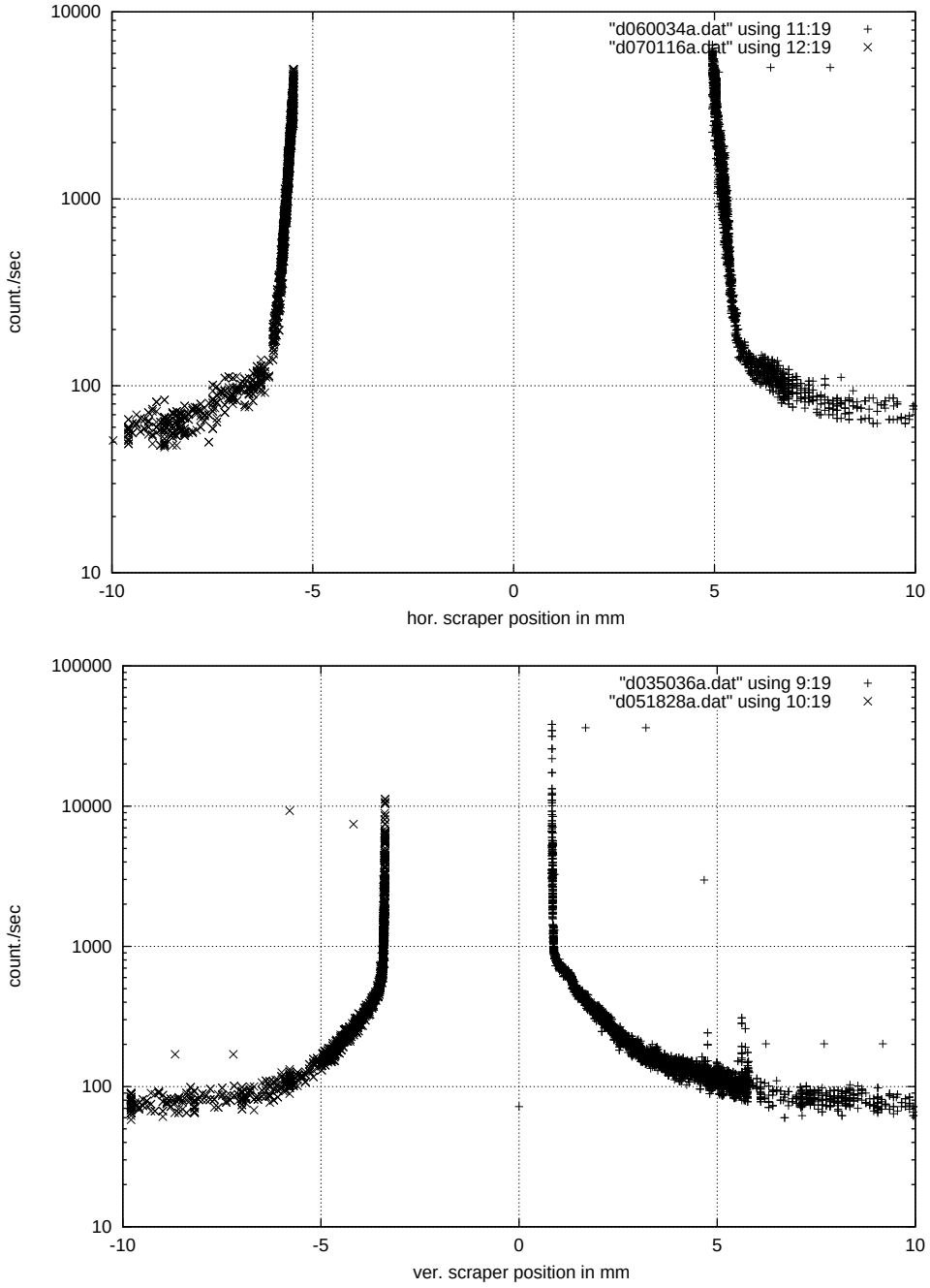


**Figure 4.1**: Beam loss rates versus scraper position, with the regular focusing scheme and with beam-beam interaction.

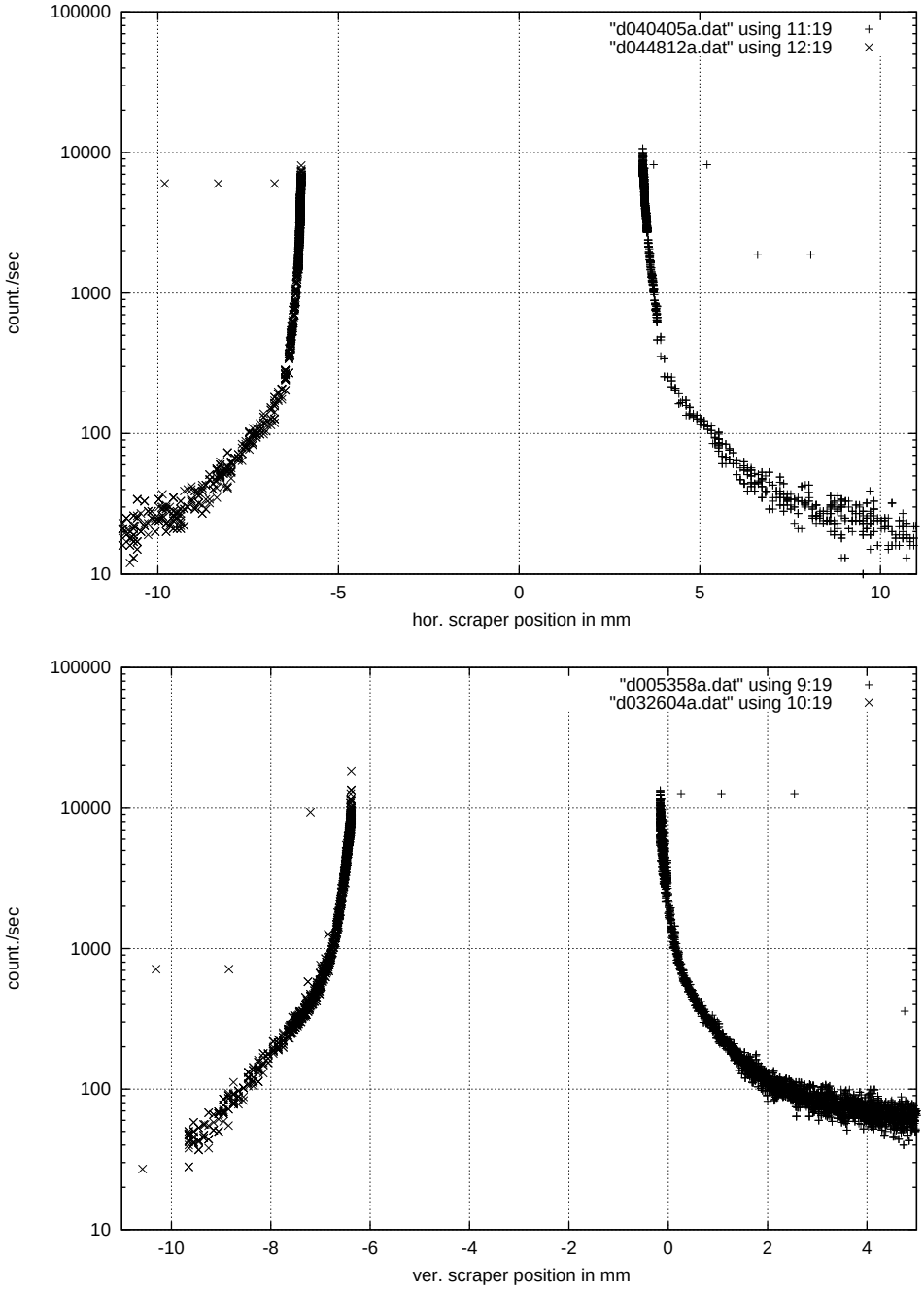


**Figure 4.2**: Beam loss rates versus scraper position, with the upgrade focusing scheme and with beam-beam interaction.

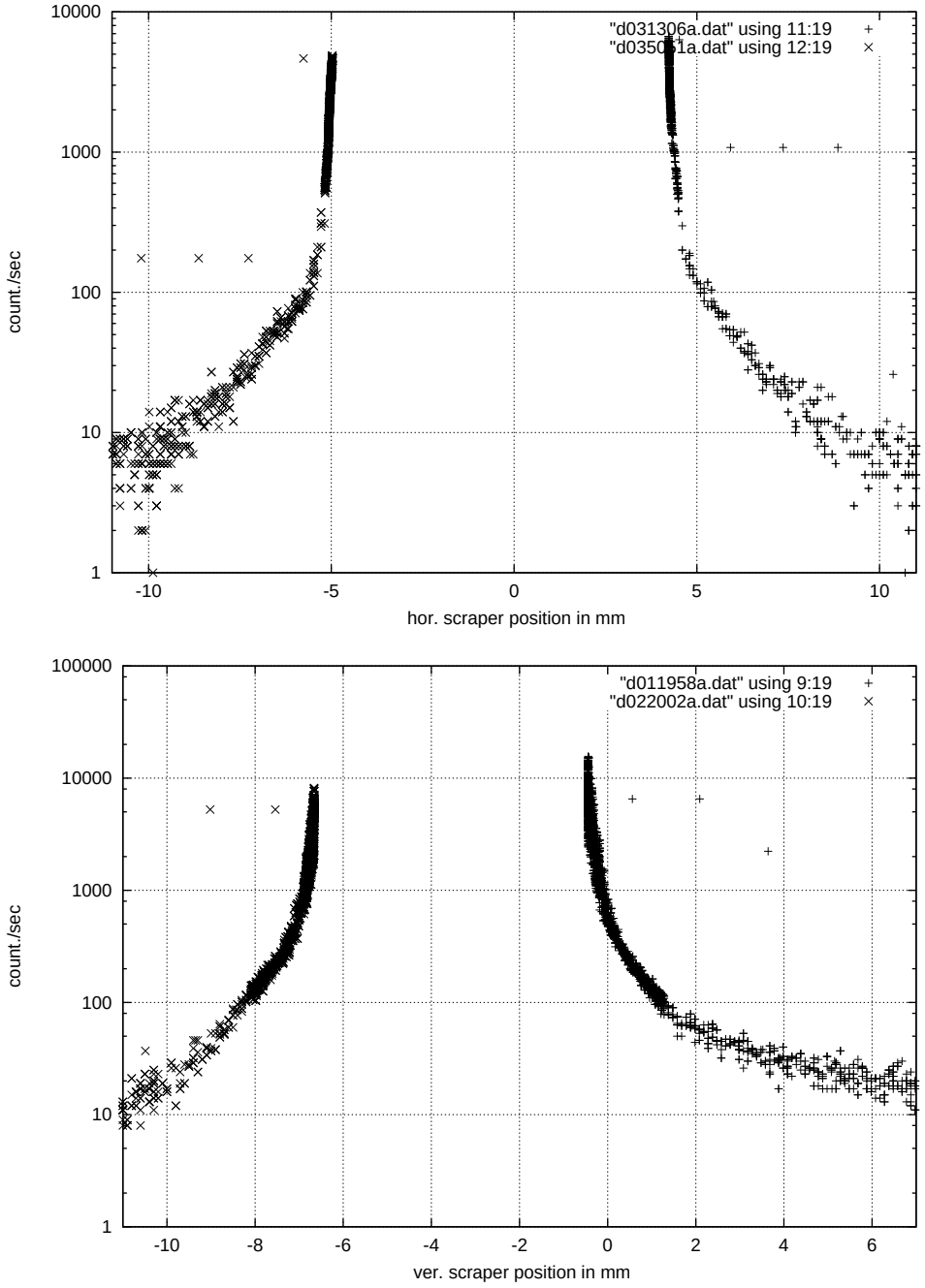


**Figure 4.3**: Beam loss rates versus scraper position, with the upgrade focusing scheme and without beam-beam interaction.

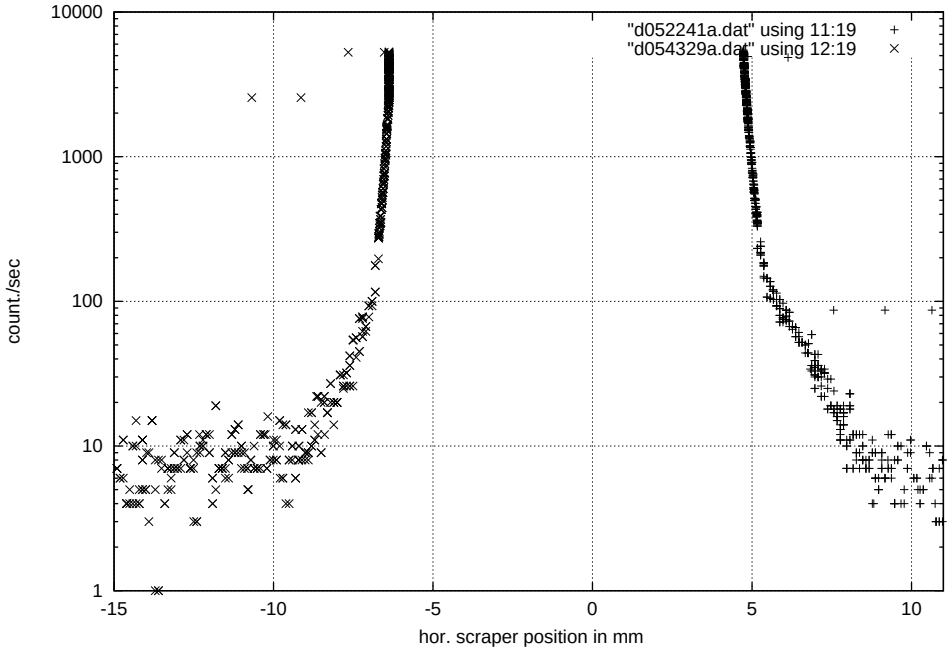


**Figure 4.4**: Beam loss rates versus horizontal scraper position, with the regular focusing scheme and without beam-beam interaction.

The standard deviation of the horizontal beam distribution $\sigma_x$ can be obtained from measured scraper position at which the lifetime is two hour. In figure 4.1 for example they are 4.95mm or $-5.49$mm respectively:

$$2 \cdot 5.77\sigma_x = (|-5.49| + 4.95)mm \ , \quad \rightarrow \sigma_x = 0.905mm \tag{4.2}$$

In this way the standard deviation of the horizontal and vertical beam distribution was obtained for the regular and the upgrade focusing scheme.

The table.4.1 gives the measured and the theoretical standard deviations for the cases, where no beam-beam interaction acts, while the table.4.2 gives the measured and theoretical standard deviations with beam-beam interaction. The theoretical values for the standard deviation of the horizontal distribution were simulated by the program MAD, where the $\beta$-beat due to the beam-beam interaction is considered. Since the recent measurements [18] suggests that the frequency of the RF system is roughly 154Hz lower than central frequency, the theoretical values for the standard deviation were also simulated with the frequency shift.

For the regular and the upgrade focusing schemes, the measured horizontal standard deviations agree well with the simulated values which have a frequency shift of 154Hz if no beam-beam interaction acts. In the case of the upgrade focusing scheme under the influence of the beam-beam interaction the measured horizontal standard deviation agrees with the simulated value which has a frequency shift of 154Hz. For the regular focusing scheme the simulated values are larger or smaller than the

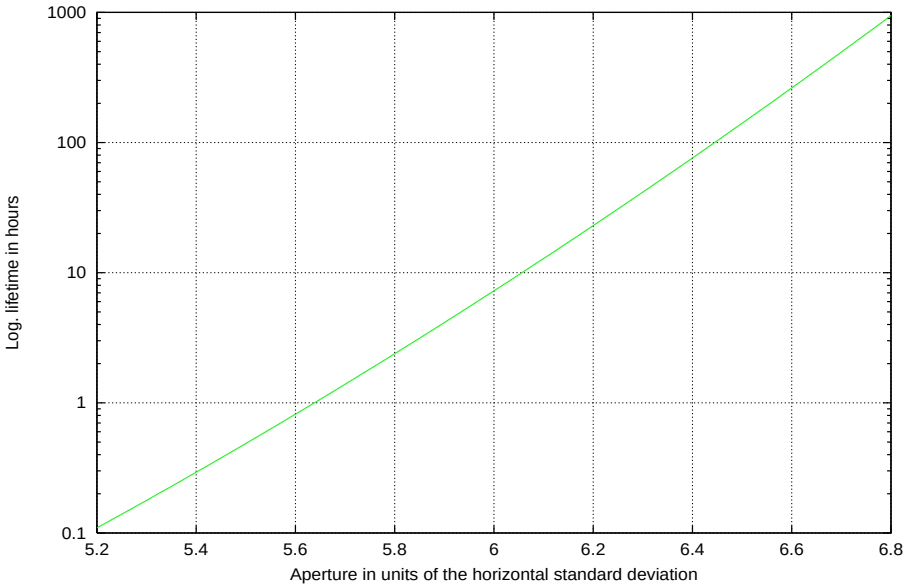


**Figure 4.5**: Regular focussing scheme, with beam-beam interaction.

| focusing scheme | $\sigma_x$ regular | $\sigma_y$ regular | $\sigma_x$ upgrade | $\sigma_y$ upgrade |
|---|---|---|---|---|
| theoretical with $\Delta RF = 0Hz$ | 0.843mm | - | 0.731mm | - |
| theoretical with $\Delta RF = 154Hz$ | 0.953mm | - | 0.810mm | - |
| measured | 0.950mm | 0.268mm | 0.800mm | 0.537mm |

**Table 4.1**: The theoretical and the measured standard deviation of the transverse beam distribution, without beam-beam interaction.

measured horizontal standard deviation, if beam-beam interaction acts. A beat of the beta function could lead to this discrepancy. Therefore the beta function at the position of the scrapers should be measured.

In HERA–e, leptons suffer energy losses or deflections by collisions with residual gas molecules. These can lead to losses of the leptons causing a reduction of the beam lifetime. After the collision the leptons which are not lost have larger oscillation amplitudes and increase the population in the tails of the lepton distribution. A reduction of the aperture during the scraping measurements absorbs all particles which reach a larger amplitude than the scraper position and leads therefore to a reduction of the beam lifetime. The connection between the beam lifetime contribution $\tau_{gas}(z)$ due to the beam-gas scattering and the transverse aperture $z$ in this

| focusing scheme | $\sigma_x$ regular | $\sigma_y$ regular | $\sigma_x$ upgrade | $\sigma_y$ upgrade |
|---|---|---|---|---|
| theoretical with $\Delta RF = 0Hz$ | 0.841mm | - | 0.746mm | - |
| theoretical with $\Delta RF = 154Hz$ | 0.950mm | - | 0.827mm | - |
| measured | 0.905mm | 0.370mm | 0.822mm | 0.539mm |

**Table 4.2**: The theoretical and the measured standard deviation of the transverse beam distribution, with beam-beam interaction.

case is given by [23]:

$$\tau_{gas}(z) = \frac{\gamma^2 k_b T}{2\pi Z^2 re^2 cP} \frac{z^2}{\beta_{ave.}\beta_{sca}} \tag{4.3}$$

where $P$ is the gas pressure, $k_b$ is the Boltzmann constant, $Z$ is the atomic number of the gas atom, $re$ is classical electron radius, $\gamma$ is the relativistic factor, c is the light speed, $\beta_{ave.}$ is the average beta function, $\beta_{sca}$ is the beta function at the scraper, and T is the temperature.

The lifetime $\tau$ of the lepton beam is determined by the lifetime $\tau_{qz}$ of a Gaussian distribution inside the physical aperture and the lifetime$\tau_{gas}$ due to the beam-gas scattering:

$$\frac{1}{\tau} = \frac{1}{\tau_{qz}} + \frac{1}{\tau_{gas}} \ . \tag{4.4}$$

The connection between the total lepton losses $\Delta N$ and the lifetime $\tau$ is given by:

$$\Delta N = N_0 \cdot \left(1 - e^{\frac{\Delta t}{\tau}}\right) \tag{4.5}$$

where $N_0$ is the initial number of leptons, and $\Delta t = 1$ sec is the time interval during which the BLMs accumulate the lepton losses.

Using the above formulas, the loss rates as functions of the scraper positions can be calculated. The measured and calculated loss rates as functions of the corresponding scraper positions are shown in the figures 4.6, 4.7, 4.8, 4.9.

From the figures 4.6, 4.7, 4.8, 4.9 it is to be seen that the measured loss rates can not be explained only by a Gaussian distribution with additional tail population due to the beam-gas scattering. An other effect, probably nonlinear forces, acts on the lepton beam and leads to the additional population of the tails. In order to explain the tail scan experiments completely, it is therefore useful to investigate in the nonlinear forces in HERA–e in future simulations.

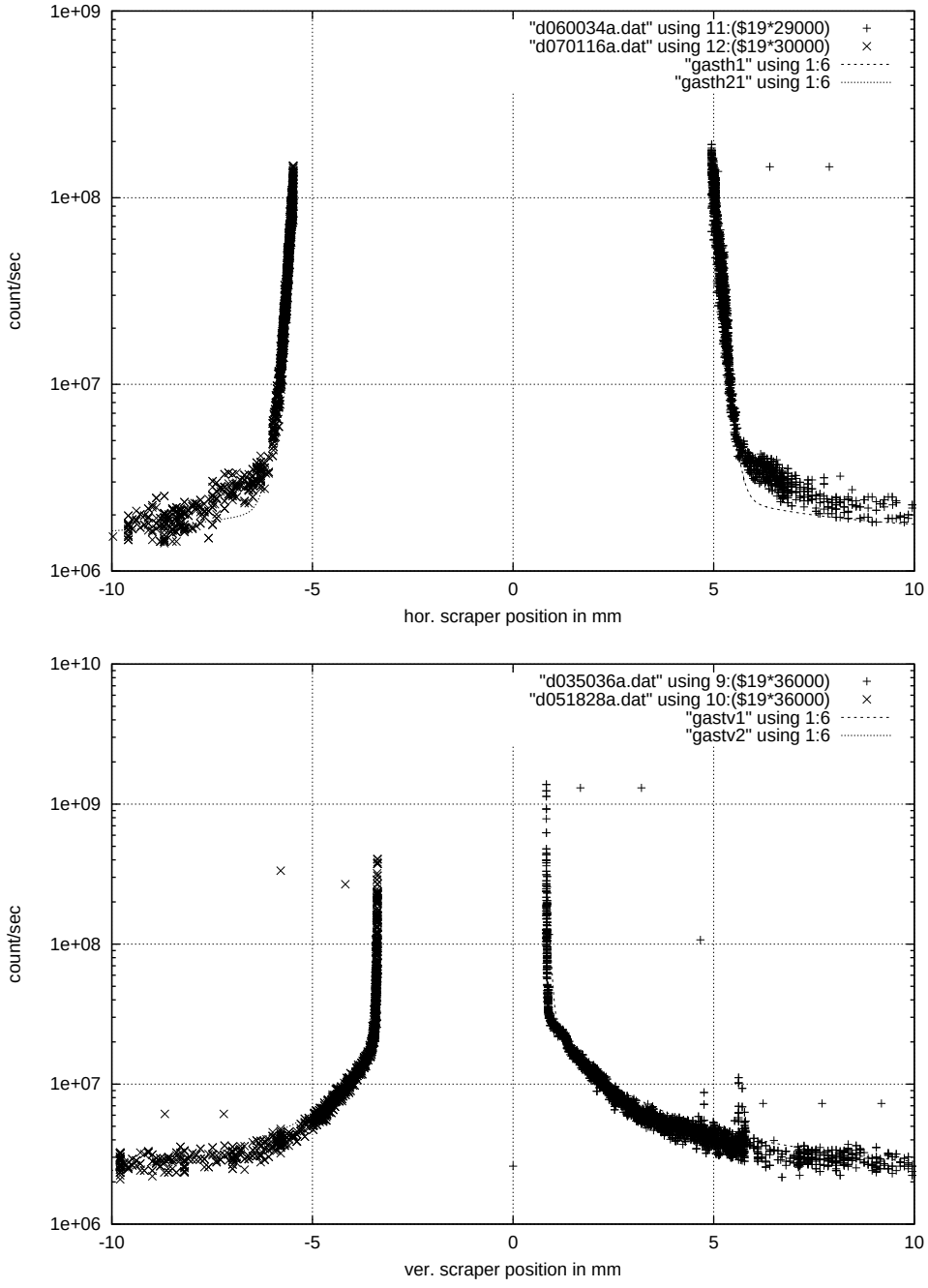


**Figure 4.6**: Measured (+,×) and the calculated (line) beam loss rates versus scraper position, with the regular focusing scheme and with beam-beam interaction.

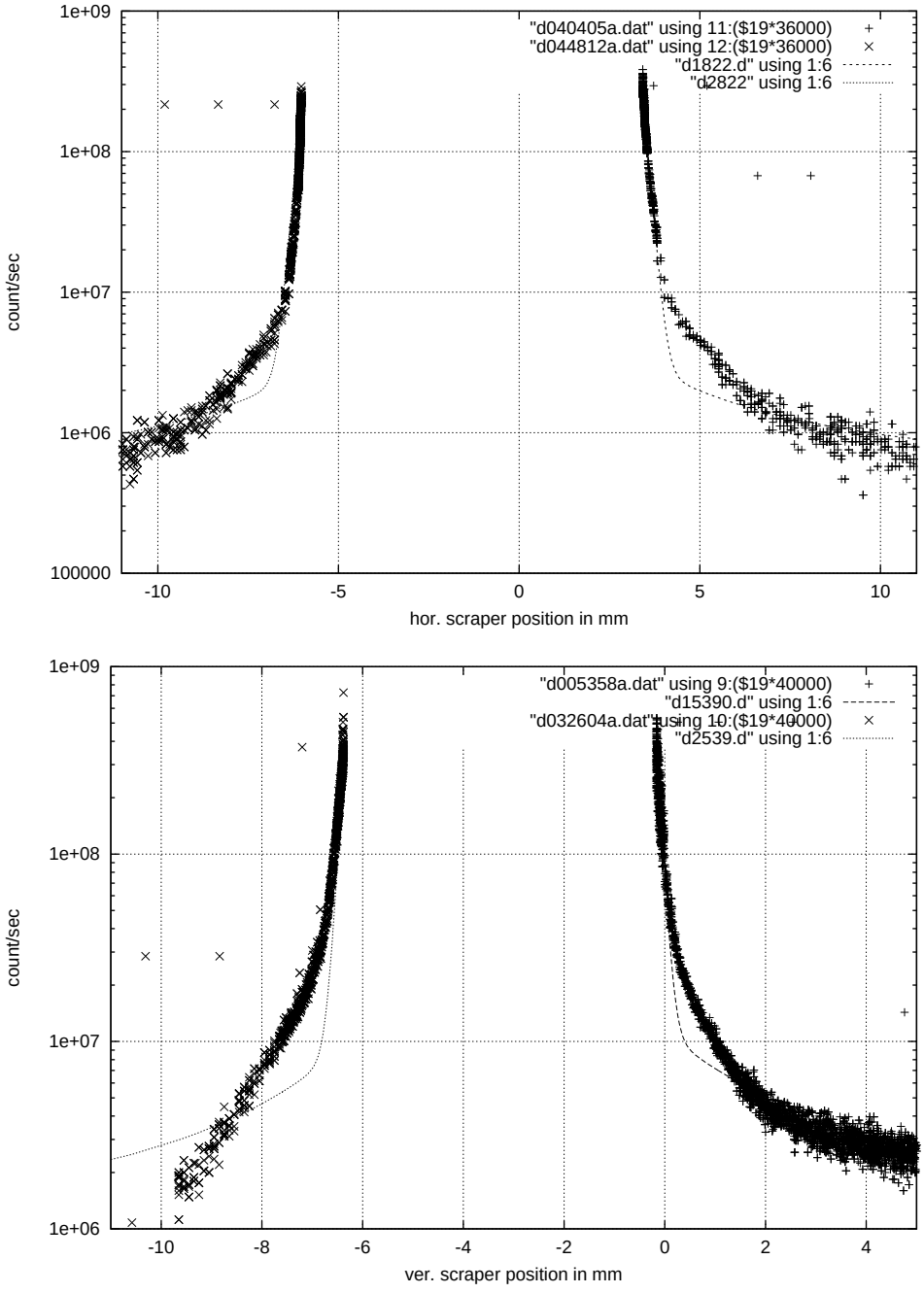


**Figure 4.7**: Measured (+,×) and the calculated (line) beam loss rates versus scraper position, with the upgrade focusing scheme and with beam-beam interaction.

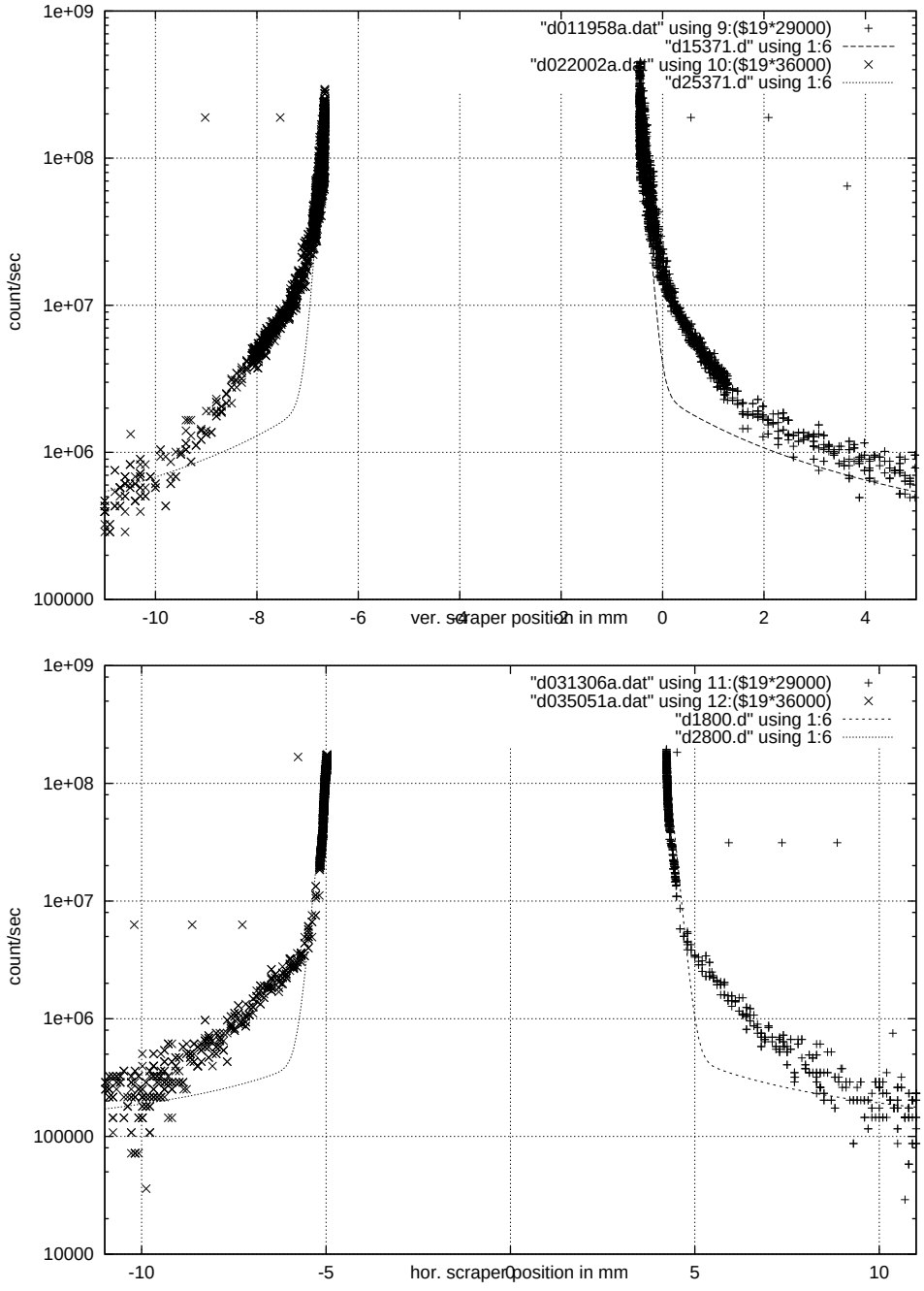


**Figure 4.8**: Measured (+,×) and the calculated (line) beam loss rates versus scraper position, with the upgrade focusing scheme without beam-beam interaction.

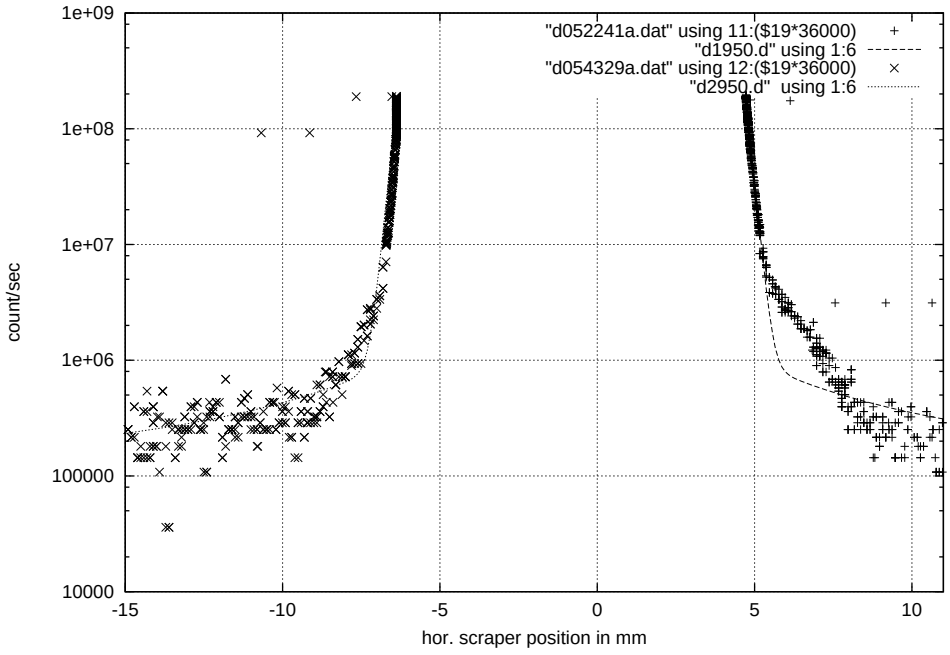


**Figure 4.9**: Measured (+,×) and the calculated (line) beam loss rates versus horizontal scraper position, with the regular focusing scheme and without beam-beam interaction.

# 5 Dispersion Measurement at HERA–e

by A. Meseck, DESY Hamburg

Date: 1999, Apr. 7, 3am to 7am, Logbook XXXVI, p. 214–215

The deviation from the nominal dispersion due to nonlinear forces could cause an increase of the emittance in HERA–e [24]. For luminosity upgrade project, where a reduction of the emittance is intended, the horizontal dispersion in the current HERA electron ring was therefore measured. The beam size measured by the Synchrotron Radiation (SR) Monitor can be used to measure the horizontal emittance of the electron beam. The emittance is obtained from the synchrotron light spot by subtracting the contribution due to energy spread and the dispersion at the position of the SR-Monitor [20]. Therefore the dispersion was also measured at the position of the SR-Monitor.

## 5.1 Measurements and Evaluation

The measurement was carried out after a lumi-run on April $23rd$ in 1999. Before beginning the measurement, the proton beam was dumped and the synchronization between HERA and PETRA was switched off.

The dispersion measurement was performed by shifting the RF frequency in steps of 150Hz or 300Hz. At each step the beam position was measured by Beam Position Monitors (BPMs). After each frequency shift the data of the BPMs were stored in a separate file and the image of the SR-Monitor was printed out. The latter allows us to determine the dispersion at the position of the SR-Monitor.

Changes in the RF frequency cause momentum deviation with respect to the nominal momentum of the beam. The connection between the RF frequency shift $\Delta f$ and the momentum deviation $\Delta p$ is given by:

$$\frac{\Delta p}{p} = -\frac{\Delta f}{f} \cdot \frac{1}{\alpha_p} \ , \tag{5.1}$$

where $\alpha_p$ is momentum compaction factor, $f$ is the nominal RF frequency, and $p$ is the nominal momentum.

Particles with different momenta have different closed orbits. The difference of the orbits $\Delta x$ due to the momentum deviation is called the dispersion $D$:

$$D = \frac{\Delta x}{\frac{\Delta p}{p}} \ . \tag{5.2}$$

Using the above formulas and the data of the BPMs and the SR-Monitor, the dispersion at the position of the BPMs as well as the horizontal dispersion at the position of the SR-Monitor were determined.

The Simulation of the dispersion by the program PETROS yields a horizontal dispersion of 822mm at the position of the SR-Monitor. The measured horizontal dispersion of $840.063 \pm 15.641$mm agrees well with the simulated value.

Figure 5.1 shows the simulated and the measured horizontal dispersion at the position of the BPMs. There was a good agreement between measured and theoretical dispersion. Figure 5.2 shows the simulated and the measured vertical dispersion at the position of the BPMs. There was obviously a larger deviation of the nominal dispersion around monitor 150, which is in the section east left of the IP.

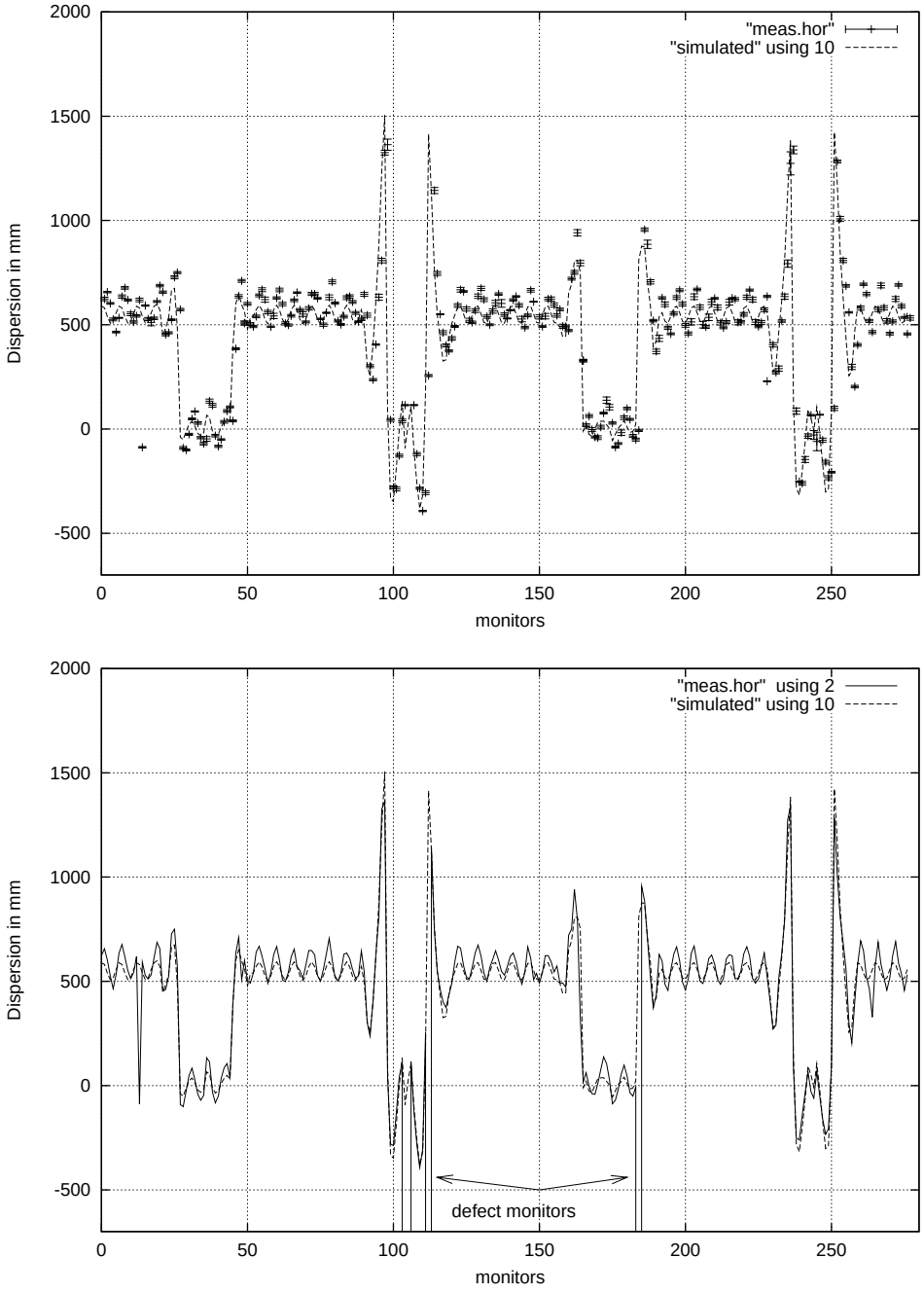


**Figure 5.1**: The simulated and measured horizontal dispersion in HERA–e, top: With error bars.

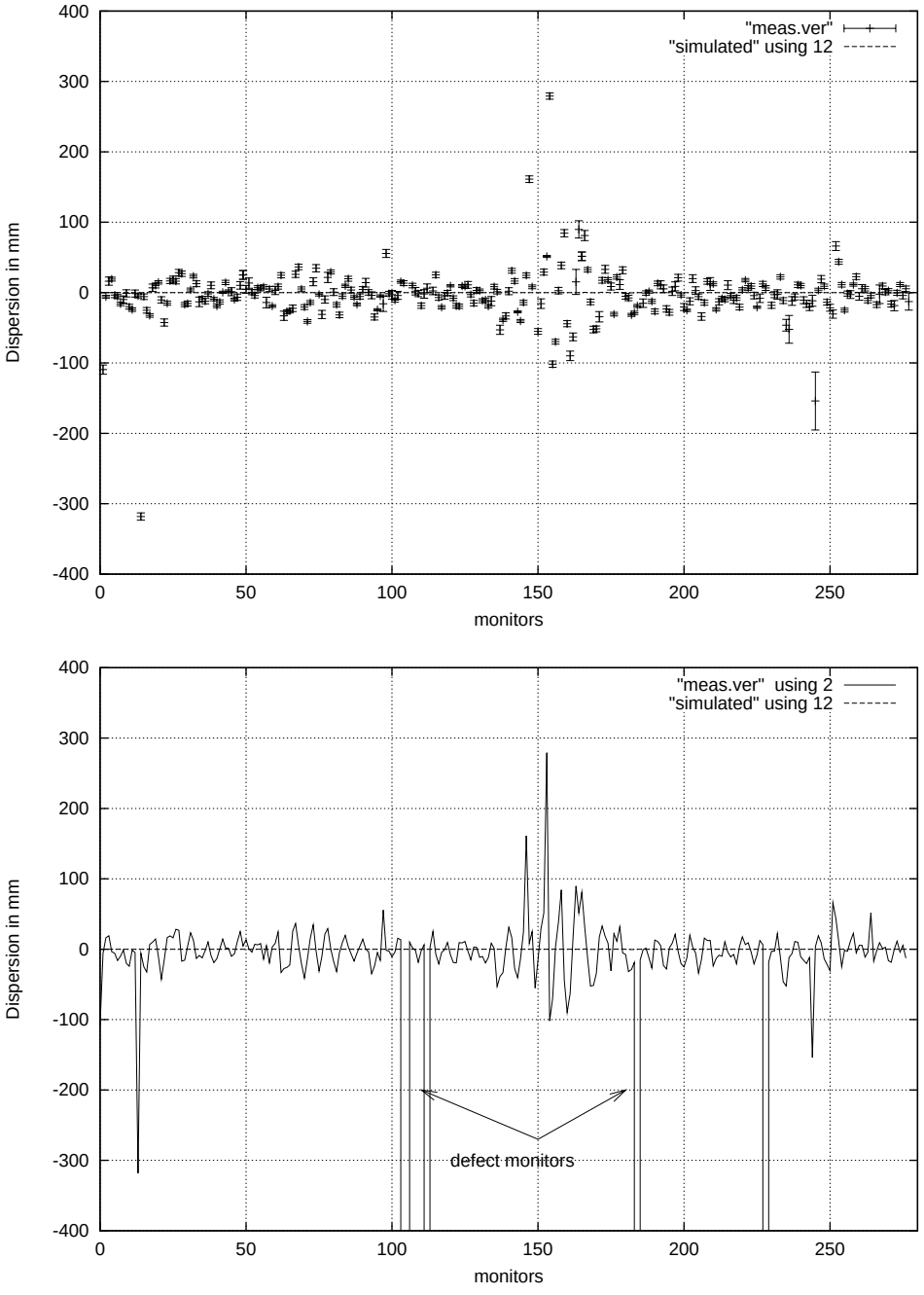


**Figure 5.2**: The simulated and measured vertical dispersion in the HERA electron ring, top: With error bars.

# 6 Measurement of the Center Frequency in the HERA Electron Ring

by B. Holzer, DESY Hamburg

Date: 1999, July 3, 7am to 10pm, Logbook XXXVII, p. 191–199

As mentioned in the previous report on HERA machine studies [25] a change in the RF frequency of the HERA electron storage ring is planned in context with the luminosity upgrade project. It will lead to a redistribution of the damping partition numbers and result in a smaller horizontal emittance of the electron beam.
Measurements of the center frequency of the present machine therefore have been performed to investigate the effect and to evaluate the required space in the frequency window of the machine. The center frequency is established – by definition – if the corresponding closed orbit is running through the center of all magnetic elements, namely the quadrupole and sextupole magnets.
For the measurement a stored electron beam at injection energy of $E_e = 12GeV$ was used in the past. The frequency of the 500MHz RF system was shifted slowly and the resulting change of the horizontal and vertical tune was measured.
Although the measurement itself seems to be straight forward the result that had been obtained was surprising: Different values for the center frequency have been obtained using the horizontal or the vertical tune curve. Therefore it was decided to repeat the studies.

Two major changes with respect to the former studies should be mentioned here:

- Unlike to the measurements in December 1998 and June 1999 this time the beam was ramped up to flat top energy of $E_e = 27.5$GeV. In addition the beam optics chosen during the measurements is now the luminosity optics. (The two previous measurements were done at an energy of $E_e = 12$GeV and using the so-called injection optics of the storage ring.)

- A number of ground faults have been found in February 1999 leading to problems in the HERA-e main dipole circuit. It is not clear how long these problems existed before they have been detected. But it is probable that this effect had an influence on the beam orbit and so on the measurement of the center frequency.

## 6.1 Measurement

The procedure of the measurement has been explained in the previous studies report: An electron beam was injected at 12GeV, accelerated to flat top $E_e = 27.5$GeV and

brought to the so-called luminosity file. That means the storage ring was put to luminosity conditions with the exception of the beam collisions itself: No colliding proton beam was present. Tune controller and feed-back system were switched off, the tune indicator however was active as for the procedure the tune measurement was needed.

The frequency of the 500MHz RF system was shifted slowly and the resulting change of the horizontal and vertical tune was measured. The same measurement was repeated after changing the strength of all sextupole magnets in the ring by a small amount. The resulting tune values, plotted as a function of the frequency change, will have a different ascent: The particles running off center through the sextupole magnets will be affected by the stronger or weaker focusing strength of the "off-center sextupole lenses".

At the center frequency however the closed orbit is expected to pass without offset through the sextupoles and the different strengths of these magnets will have no effect on the tune. So the measured tune values will be the same even if the sextupole strengths had been changed.

## 6.2 Result

In figure 1 the tune in the horizontal plane is plotted as a function of the frequency shift. The horizontal plane shows the difference of the applied frequency at the moment of the measurement with respect of the nominal frequency, that was used during the routine luminosity operation. The three curves represent the measured tune values for the standard sextupole settings and for a machine of 10% increased or 10 % decreased sextupole fields respectively.

The straight lines are a least-square-fit through the data. The tune lines cross at a frequency of

$$f_{centre} = -214Hz \tag{6.1}$$

which means that the true center frequency found by the measurement is about 214Hz lower than the frequency used in the standard running conditions of the machine at that time.

The plot resulting from measurements of the vertical tune is shown in the next figure. The lines cross here at a frequency shift of

$$f_{centre} = -22Hz. \tag{6.2}$$

Again we have to conclude that the result of the horizontal and vertical tune shift measured as a function of the applied frequency shift leads to a center frequency which differs in the horizontal and vertical plane. Even more neither the center frequency deduced from the horizontal nor from the vertical measurement is in agreement with the results obtained from the previous machine studies. For completeness in the table the three measurements are summarized:

The different boundary conditions present during the studies are mentioned in the last column of the table. Mainly the ground fault problems could be a possible

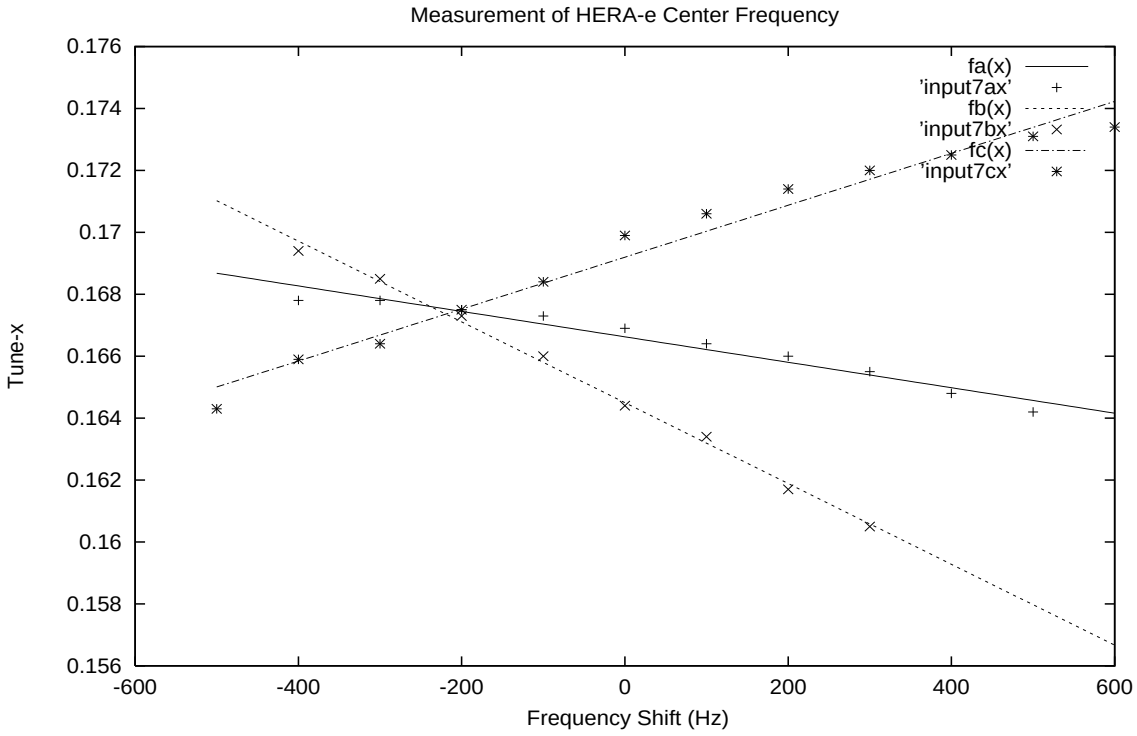


**Figure 6.1**: Measurement of the horizontal tune shift as a function of the changing RF frequency. The crossing point of the fitted lines reflect the center frequency of the machine.

explanation for the different results of the three measurements. In all results obtained so far we get however different values for the center frequency found by measurements in the horizontal and in the vertical plane. Therefore the hypothesis given already in [25] is confirmed: A possible explanation would be that the horizontal and vertical acting sextupole magnets are aligned in the ring with a substantial systematic offset in the horizontal plane with respect to each other.

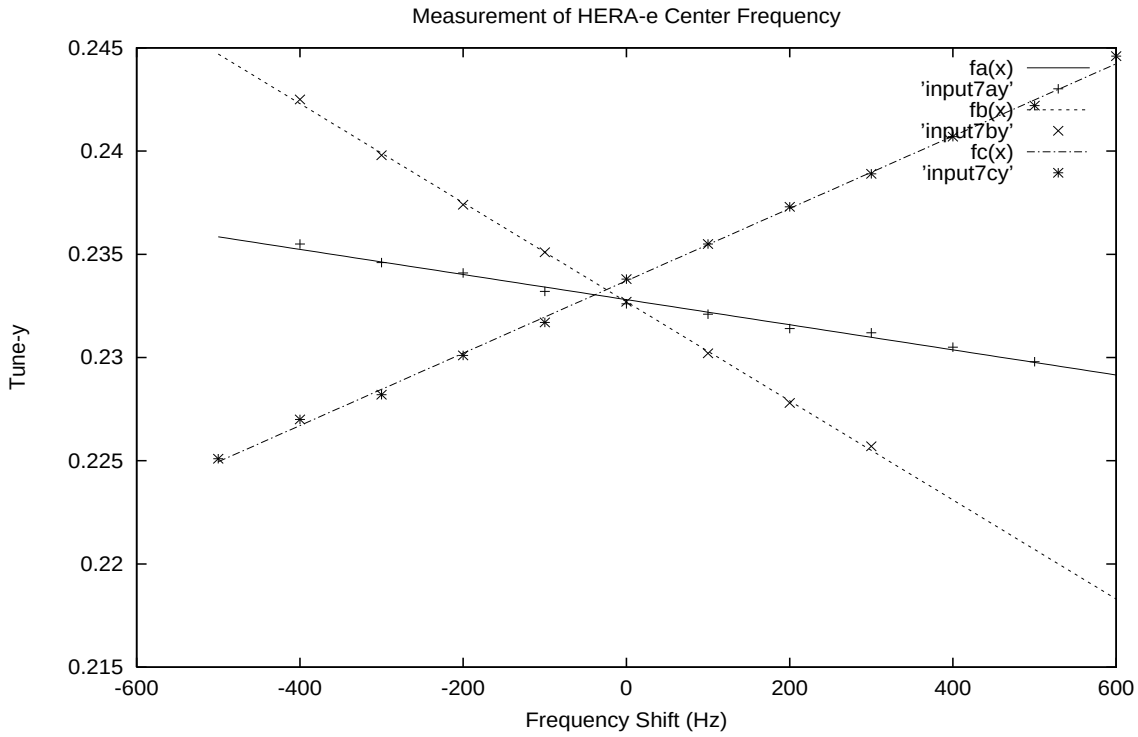


**Figure 6.2**: Measurement of the vertical tune shift as a function of the changing RF frequency.

| Optics | Energy | frequency shift | date | |
|---|---|---|---|---|
| Injection | 12GeV<br>12GeV | horizontal -139Hz<br>vertical +103Hz | Dec. '98 | |
| Injection | 12GeV<br>12GeV | horizontal -277Hz<br>vertical +28Hz | June '99 | ground faults repaired<br>in main dipole chain |
| Luminosity | 27.5GeV<br>27.5GeV | horizontal -214Hz<br>vertical -22Hz | July '99 | different energy and<br>beam optics |

**Table 6.1**: Comparison of the result obtained from three measurements of the HERA-e center frequency. The values of the frequency shift indicated in the table refer to the nominal frequency ($f_0 = 500$MHz) which is used for routine machine operation.

# 7 Detection of a Localized Sources of Coupling and Focusing Perturbations from Injected Beam First Turn Trajectories

by Y. Alexahin, JINR Dubna 141980 Russia,
F. Brinker, and G. H. Hoffstaetter, DESY Hamburg

Date: 1999, Dec. 15, 3pm to 11pm, Logbook XXXIV, p. 145–148

A conventional method for the detection of optics errors consists of the two following steps [26]:

1. check of the optics functions, which can be performed rather accurately by shaking the beam at the betatron frequencies and measuring the excited oscillation amplitude at the pick–ups around the ring;

2. determination of the field errors which would produce the detected deviations from the design optics (if any) by solving the inverse problem.

Besides difficulties inherent to inverse problems, the applicability of the first step to HERA is limited by the lack of the necessary hardware. For the case of coupling it has been instead suggested [27] to determine its sources by exciting large amplitude horizontal betatron oscillations during the first turn after injection with the help of a few correctors (to change the initial phase angle) and to look at the transfer of energy into the vertical degree of freedom [28]. Would there be a strong localized coupler, it could be immediately detected and its strength could be found with a minimum of processing as described below. But in fact more information can be extracted from these data, in particular on the horizontal focusing perturbations.

## 7.1 Basics

With the help of the ideal optical functions [29, 30], one can introduce the normal form variables (complex amplitudes). The one turn transport matrix from some azimuth $s$ once around the ring is given by

$$\underline{M}_0(s) = \cos(\mu)\underline{1} + \sin(\mu) \begin{pmatrix} \alpha(s) & \beta(s) \\ -\gamma(s) & -\alpha(s) \end{pmatrix} . \tag{7.1}$$

The eigensystem of this matrix is

$$\lambda_1 = e^{i\mu} \ , \quad \lambda_2 = e^{-i\mu} \ , \quad \vec{v}_1 = \begin{pmatrix} -\beta \\ \alpha - i \end{pmatrix} \ , \quad \vec{v}_2 = \begin{pmatrix} -\beta \\ \alpha + i \end{pmatrix} \ . \tag{7.2}$$

With some $\xi, \zeta \in \mathbb{C}$ the matrix transforming to the normal form space is therefore

$$\underline{A}^{-1}(s) = \begin{pmatrix} -\xi\beta & -\zeta\beta \\ \xi(\alpha - i) & \zeta(\alpha + i) \end{pmatrix} \ , \quad \underline{A}(s) = \begin{pmatrix} \zeta(\alpha + i) & \zeta\beta \\ -\xi(\alpha - i) & -\xi\beta \end{pmatrix} \frac{1}{-\xi\zeta\beta 2i} \ . \tag{7.3}$$

While the transport matrix from a betatron phase $\Phi_0$ at $s_0$ to $\Phi$ at $s$ is given by

$$\begin{aligned} \underline{M}(s, s_0) &= \frac{\cos(\Phi - \Phi_0)}{\sqrt{\beta_0\beta}} \begin{pmatrix} \beta & 0 \\ \alpha_0 - \alpha & \beta_0 \end{pmatrix} \\ &+ \frac{\sin(\Phi - \Phi_0)}{\sqrt{\beta_0\beta}} \begin{pmatrix} \alpha_0\beta & \beta_0\beta \\ -(1 + \alpha_0\alpha) & -\alpha\beta_0 \end{pmatrix} \ , \end{aligned} \tag{7.4}$$

in normal form variables it is largely simplified,

$$\underline{N}(s, s_0) = \underline{A}(s)\underline{M}(s, s_0)\underline{A}^{-1}(s_0) = \sqrt{\frac{\beta_0}{\beta}} \begin{pmatrix} \frac{\xi_0}{\xi} e^{i(\Phi - \Phi_0)} & 0 \\ 0 & \frac{\zeta_0}{\zeta} e^{-i(\Phi - \Phi_0)} \end{pmatrix} \ . \tag{7.5}$$

By the choice of $\xi(s) = -\frac{e^{i\Phi(s)}}{\sqrt{2\beta(s)}}$ and $\zeta(s) = -\frac{e^{-i\Phi(s)}}{\sqrt{2\beta(s)}}$ the transport matrix in normal form space is the identity and the transformation matrixes are given by

$$\underline{A}^{-1}(s) = \frac{1}{\sqrt{2\beta}} \begin{pmatrix} \beta e^{i\Phi(s)} & \beta e^{-i\Phi(s)} \\ (i - \alpha)e^{i\Phi(s)} & -(i + \alpha)e^{-i\Phi(s)} \end{pmatrix} \ , \tag{7.6}$$

$$\underline{A}(s) = \frac{1}{\sqrt{2\beta}} \begin{pmatrix} (1 - i\alpha)e^{-i\Phi(s)} & -i\beta e^{-i\Phi(s)} \\ (1 + i\alpha)e^{\ i\Phi(s)} & i\beta e^{\ i\Phi(s)} \end{pmatrix} \ . \tag{7.7}$$

The coefficients in normal form space given by

$$\begin{pmatrix} a \\ a^* \end{pmatrix} = \underline{A}(s) \begin{pmatrix} x \\ x' \end{pmatrix} \tag{7.8}$$

and due to $N(s, s_0) = \underline{1}$ they are constant along the trajectory of a particle if it follows the unperturbed betatron oscillation described by $\beta(s)$ and $\Phi(s)$.

For the horizontal oscillations the constant is given by

$$a_x = |a_x|e^{i\Psi_x} = \frac{x - i(\beta_x x' + \alpha_x x)}{\sqrt{2\beta_x}} e^{-i\Phi_x} \tag{7.9}$$

and analogously for the vertical plane. Conversely the coordinate is given by

$$x = \sqrt{2\beta_x}\Re(a_x e^{i\Phi_x}) \ . \tag{7.10}$$

Let there now be a perturbing element at some position $s_p$ which produces an additional kick

$$\Delta x' = -\Delta k_1 l \cdot x \ . \tag{7.11}$$

This kick may be associated with:

a) a quadrupole field error,

b) a horizontal sextupole misalignment $\Delta k_1 = -k_2 x_s$,

c) a momentum error $\Delta k_1 = -k_1 \delta_p$,

d) a horizontal off–momentum dispersive orbit in a sextupole $\Delta k_1 = -k_2 D_x \delta_p$.

Then downstream of the perturbing element equation (7.9) yields

$$\begin{aligned} a_x(s > s_p) &= |a_x| e^{i\Psi_x} = a_{x0} - i\sqrt{\frac{\beta_x(s_p)}{2}} e^{-i\Phi_x(s_p)} \Delta x' \\ &= a_{x0} + i\Delta k_1 l \beta_x(s_p) e^{-i\Phi_x(s_p)} \Re[a_{x0} e^{i\Phi_x(s_p)}] \\ &= a_{x0}[1 + i\frac{\Delta k_1 l \beta_x(s_p)}{2}(1 + e^{-2i(\Psi_{x0}+\Phi_x(s_p))})] \\ &= a_{x0}[1 + \frac{\Delta k_1 l \beta_x(s_p)}{2}(1 + \cos 2(\Psi_{x0} + \Phi_x(s_p)) \\ &+ i\frac{\Delta k_1 l \beta_x(s_p)}{2} \sin 2(\Psi_{x0} + \Phi_x(s_p))] \ . \end{aligned}$$

For a small perturbation $|\Delta k_1| l \beta_x << 1$ the jumps in the phase $\Psi_x = Arg(a_x)$ and the absolute value of $a_x$ are

$$\Delta\Psi_x = \Delta k_1 l \beta_x(s_p) \frac{1}{2}[1 + \cos 2(\Psi_{x0} + \Phi_x(s_p))] \ , \tag{7.12}$$

$$\Delta|a_x| = |a_{x0}| \Delta k_1 l \beta_x(s_p) \frac{1}{2} \sin 2(\Psi_{x0} + \Phi_x(s_p)) \ . \tag{7.13}$$

If the initial vertical amplitude is small compared to the horizontal one then its large jumps are presumably caused by coupling: $y' = n_1 l x$,

$$\begin{aligned} a_z(s > s_p) &= a_{y0} - i\sqrt{\frac{\beta_y(s_p)}{2}} e^{-i\Phi_y(s_p)} \Delta y' \\ &= a_{y0} - i n_1 l \sqrt{\beta_x(s_p)\beta_y(s_p)} e^{-i\Phi_y(s_p)} \Re[a_{x0} e^{i\Phi_x(s_p)}] \ , \end{aligned} \tag{7.14}$$

where $n_1$ is the skew quadrupole field gradient which may originate from either

a) a quadrupole tilt by an angle $\theta$ with $n_1 = -k_1 \theta$,

b) a vertical sextupole misalignment with $n_1 = -k_2 y_s$,

c) a vertical off–momentum dispersive orbit in a sextupole with $n_1 = k_2 D_y \delta_p$.

The complex amplitudes along the ring can be derived from the beam positions at consecutive pairs of adjacent monitors if these are not $n\pi$ apart in betatron phase advance. Eliminating $a_x^*$ from

$$a_x e^{i\Phi_{x1}} + a_x^* e^{-i\Phi_{x1}} = 2\frac{x_1}{\sqrt{2\beta_{x1}}} \ , \quad a_x e^{i\Phi_{x2}} + a_x^* e^{-i\Phi_{x2}} = 2\frac{x_2}{\sqrt{2\beta_{x2}}} \tag{7.15}$$

leads to

$$a_x = \frac{i}{\sin(\Phi_{x2} - \Phi_{x1})} \left( \frac{x_1}{\sqrt{2\beta_{x1}}} e^{-i\Phi_{x2}} - \frac{x_2}{\sqrt{2\beta_{x2}}} e^{-i\Phi_{x1}} \right) . \tag{7.16}$$

And analogously $a_y$ can be determined. Having observed jumps in the amplitudes one may try to derive the strength and location of perturbations from the jump in the phase and in the magnitude using equations (7.12) and (7.13).

## 7.2 First Turn Measurements at HERA-e

During the December 1998 accelerator studies [27] the first turn trajectories were measured with the primary goal of finding sources of coupling between the transverse planes. Horizontal oscillations of the injected beam were excited in turn by three consecutive correctors, CH WR 309, 333, and 356, in order to change the initial betatron phase of the oscillations. The energy offset was approximately -20MeV ($\delta p = -0.17\%$) as adopted for synchrotron injection; the off–momentum reference trajectory has been subtracted from the orbit data. The measurements were repeated with the sextupoles both on and off.

### 7.2.1 Sextupole Offsets in HERA-e

During the accelerator studies [11] several methods were applied to find the central RF frequency in HERA-e, one of them consisted in determination of the average sextupole displacement with respect to the closed orbit [25]. From the dependence of the transverse tunes on the RF frequency at different sextupole settings it was concluded that there might be a systematic horizontal offset between focusing and defocusing sextupoles of about 0.5mm.

As mentioned above, the horizontal sextupole offsets produce focusing perturbations hence can be checked by the first turn method. Figure 7.1 shows the argument of the complex amplitude (its variation gives the difference between the actual and nominal phase advances) of horizontal oscillations excited by the corrector CH WR 309 (left figures) and the corrector CH WR 356 (right figures). A few monitors were excluded from the analysis including the apparently faulty OL 199 and OR 199 monitors.

Ignoring a few spikes which can be attributed to monitor errors, one can see that in the first case (left figures): a) with the sextupoles on there is a strong focusing perturbation in the East straight section (the North and East IPs are located just before monitors #57 and #127); b) the sextupoles shift the total betatron phase advance around the ring by $\approx -1$rad. This shift is compensated by the tune quadrupoles in the top figure. The focussing contribution of the sextupoles becomes apparant when the sextupoles are witched off and the phase increases by about 1rad in the bottom figure.

The sextupoles' contribution to the total chromaticity is $\Delta Q'_x(sext.) \approx 56$ and therefore $2\pi\Delta Q'_x(sext.)\delta_p \approx -0.6$rad of this phase difference is due to the energy deviation of $\delta_p \approx -0.17\%$, leaving a phase shift due to the sextupoles of $\Delta\Psi_x(sext.) \approx -0.4$rad.

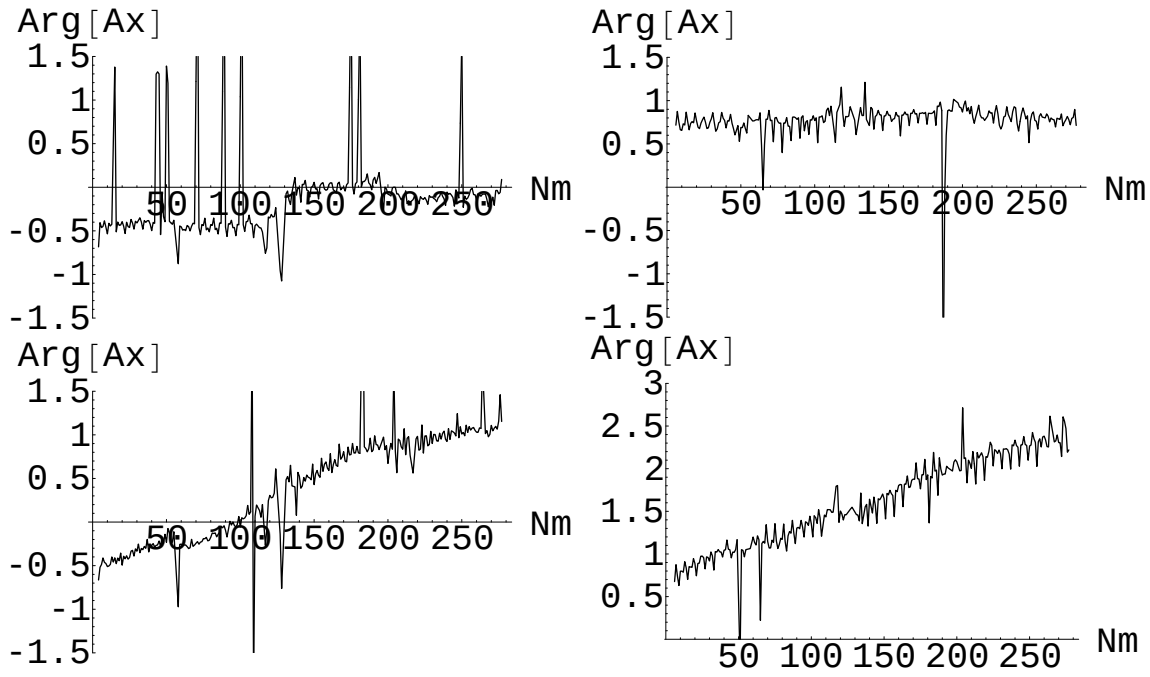


**Figure 7.1**: Relative phase advance of the horizontal betatron oscillations in the HERA electron ring excited by the CH WR 309 (left) and CH WR 356 (right) correctors versus monitor number with the sextupoles on (top) and off (bottom).

Due to the large number of sextupoles ($\approx 200$ for each plane) we may average the trigonometric function in equation (7.12) and obtain for the total sextupole contribution to the phase advance around the ring

$$\Delta\Psi_x(sext.) \approx -\frac{1}{2}\sum_s (k_2 l)_s \beta_{xs} x_{0s} \approx -0.4\text{rad} \; . \tag{7.17}$$

Then with the nominal injection optics we have from the second term

$$734.8\frac{\text{rad}}{\text{m}} < x_{0f} > -439.4\frac{\text{rad}}{\text{m}} < x_{0d} >= 0.4\text{rad} \; , \tag{7.18}$$

where $< x_{0f} >$ is the average horizontal orbit in the focusing sextupoles and $< x_{0d} >$ is that in the defocusing sextupoles. Assuming that the defocusing sextupoles are centered around the design orbit and that therefore $< x_{0d} > \approx 0$, the whole effect is ascribed to the focusing sextupoles. We obtain for their average displacement $< x_{0f} > \approx 0.54mm$ in a fair agreement with the previously mentioned method [25].

In case of exciting the CH WR 356 corrector (right figures), the localized focusing perturbations are not visible. The phase advance difference due to the sextupoles is approximately -1.6rad. The difference to the left figures may be a manifestation of the betatron coupling.

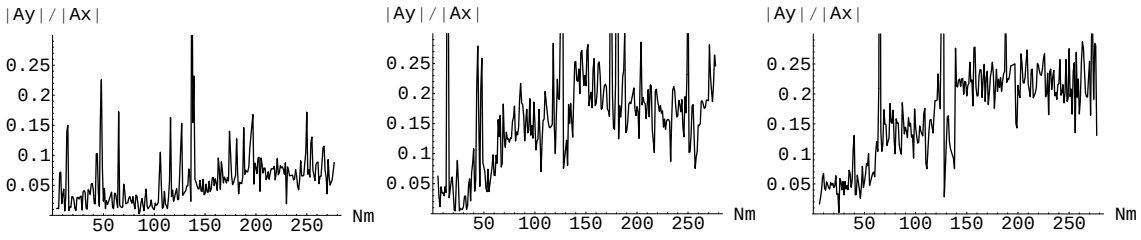


**Figure 7.2**: Ratio of betatron amplitudes versus monitor number for three initial horizontal phases.

### 7.2.2 Transverse Coupling in HERA-e

As has already been mentioned, the first turn measurements were undertaken in an attempt to find sources of coupling. Comparison of the vertical monitor readings with the sextupoles on and off [27] definitely showed that with all three initial phases the coupling is mainly associated with the sextupoles. However, just looking at the raw data did not allow to discern whether they are the strongest couplers.

The picture in the complex amplitudes provides more information. Figure 7.2 shows for the case of switched on sextupoles the absolute value of the vertical amplitude (normalized to the average value of the horizontal one) versus monitor number starting from the injection point with the exciting corrector being (from left to right) CH WR 309, 333, 356.

From the second and especially the third plot it is clear that strong coupling takes place in the vicinity of the North and East IPs (located just before monitors #57 and #127). So just as in the case of the focusing perturbations there is an apparent contradiction: the coupling shows up only in the presence of the sextupoles but in the places where they are absent.

The plausible explanation of this puzzle invokes a strong effect of the sextupoles on the spurious dispersion which may appear larger in some places (e.g. in the straight sections) with the sextupoles on, although usually it is smaller. If there were large multipole components in the fields of the low–beta quadrupoles, then the horizontal and vertical dispersion would produce respectively the focusing and coupling perturbations on the off–momentum orbit.

One can verify such a possibility by simply measuring the dispersion functions in the straight sections. It would be also worthwhile to repeat the first turn measurements with an on–energy injection.

## 7.3 Focusing Perturbations in HERA-p

First turn measurements were also performed with the proton beam excited by the CX WL 252 and 299 correctors. Since the phase between these correctors is $\pi/2$, the pictures looked very much alike with a more pronounced manifestation of coupling in the second case which is presented in figure 7.3.

The striking feature obtained in both cases results in a spectacular "saw–tooth" behavior of the argument of the horizontal amplitude (which is in effect the phase

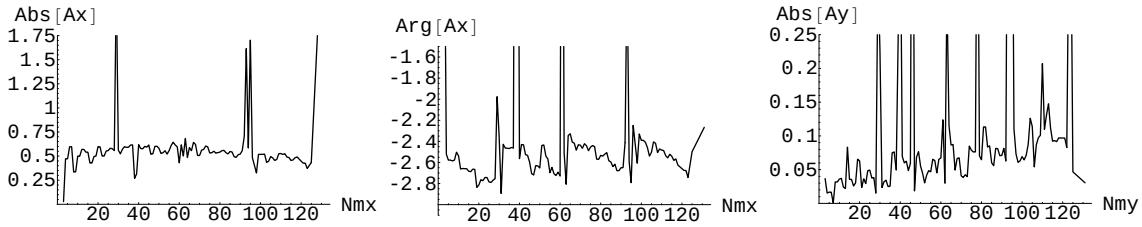


**Figure 7.3**: Complex amplitudes of the proton beam oscillations excited by the CX WL 299 corrector.

advance difference from the design value): It seems that very strong focusing perturbations in all three low–beta insertions are gradually compensated by the arc quadrupoles to fix the tune.

The large phase advance oscillations around IPs suggest that both focusing and defocusing low–beta quadrupoles are overpowered: strong upward shift of the phase at the left QR14 group is compensated by QS10 groups followed by another upward shift at the right QR14 group, the net shift being $\approx 0.4$ rad at all three IPs. Taking the shift per a QR14 group of 0.4 rad and assuming 1/2 for the square of the cosine in equation (7.12) we can estimate the QR14 field error as

$$\frac{\Delta k_1}{k_1} \approx 0.06 \ . \tag{7.19}$$

The QS10 field error is probably of the same order.

To obtain a more accurate estimate, trajectories with other initial betatron phases should be taken. It is desirable to perform measurements with an excitation of the vertical oscillations as well.

## 7.4 Conclusions

- – There are strong localized sources of focusing and coupling perturbations in the North and East straight sections of HERA-e, which manifest themselves only with the sextupoles on.
  - – The proposed explanation can be verified by measuring the dispersion functions in the straight sections and repeating the first turn measurements with an on–energy injection.
  - – There might be strong focusing perturbations in all three low–beta insertions of HERA-p which are compensated by the arc quadrupoles. Possibly the low–beta quadrupoles are overpowered by some 6%.
  - – The coupling sources in HERA-p appear to be evenly distributed around the ring.
  - – To improve the accuracy of the estimates of the low–beta quadrupoles field errors, trajectories with more initial betatron phases should be taken, desirably with excitation of the vertical oscillations as well.

also published as DESY-MDI-99-02

# 8 Improvements of the HERA Electron Beam Loss Monitor System

by K. Wittenburg, DESY Hamburg

Date: 1999, Apr. 29, 1am to Apr. 30, 7am, Logbook XXXVII, p. 50–71

The Pin Diode Beam Loss Monitors at the HERA Electron ring (BLMe) have a high intrinsic suppression of synchrotron radiation background [31]. But even so, the rate of Synchrotron Radiation background (SR) has been too high to identify local beam losses which may be responsible for the lifetime reductions at 27 GeV/c. In the following we describe the changes which were done to improve the background to signal ratio of the BLMe system.

## 8.1 Introduction

The Pin Diode Beam Loss Monitors were originally designed to prevent the superconducting magnets of the HERA proton ring from beam loss induced quenches [32]. The coincidence readout of the two PIN Diode detectors of the BLM and the counting technique are responsible for the high suppression of background from the synchrotron radiation relative to the signal from showers of high energy particles. A similar BLM System was installed in 1993 at the HERA electron ring to observe the local losses during the unexpected lifetime reductions. This system was very helpful to study the behavior and to determine the main source of the lifetime reduction [33]. After the integrated ion getter pumps were replaced with Non-Evaporative-Getter (NEG) pumps, the lifetime reductions have become less significant but are still present at a beam energy of 27.6 GeV.

The use of the BLMe system for a localization of the losses is limited by the high quantity of SR at this high beam energy. The huge amount of SR photons at the BLM location (on the inside of the beam pipe) is responsible for a high probability of conversion of two photons at the same time (within about 30 ns) in the two diodes. This kind of background cannot be distinguished from electromagnetic showers from real beam losses. Unfortunately, the count rate of showers was about one order of magnitude smaller than the background rate. Therefore an improvement of the signal to background ratio was very important to improve the detection of beam losses at high electron beam energies.

## 8.2 Hardware Improvements

Two effects contribute to the background rate:

a) A high energy Photo and Compton electron produced by a SR photon conversion in the first diode can reach the other diode and creates a coincident signal in the two diodes.

b) The high photon rate of the SR gives a high probability for the coincident conversion of two photons in the two diodes.

### 8.2.1 Photo and Compton Electrons

One can find in [33] a detailed description how a copper inlay between the two diodes reduces the probability of background counts due to Photo and Compton electrons. Figure 8.1 shows the main result of [33], namely that one can expect a background reduction due to a copper inlay by about a factor 5 at high photon fluxes as in HERAe. Note that this factor increases with the decrease of the photon flux at the monitor! The efficiency of the BLM to beam losses is not changed by this inlay.

### 8.2.2 High Photon Rate

A reduction of the high photon flux helps in 2 ways: First the probability for a coincident conversion of two photons is reduced and secondly the background rate of Photo and Compton electrons is also reduced. A reduction can be achieved by additional lead shielding.

### 8.2.3 Experiments

Our first try was to add lead around the BLM, but not at the side facing the beam pipe. In this case, there was no observable reduction in the background rate. This indicates, that the main part of the synchrotron radiation hitting the BLMs comes from the inner beam pipe (see figure 8.2). Therefore, adding a layer of lead between the pipe and the BLM to the existing 5mm layer of lead can be expected to reduce the background. Unfortunately, the signal from showers will also be reduced because some of the charged particles created in the shower will stop in the additional lead layer. Nevertheless, one can gain in the signal to background ratio because the lead absorbs the low energy SR-photons more efficiently than the high energy shower particles. Therefore, we installed at some monitors a layer of 12 cm additional lead and the copper layer between the two diodes. Figure 8.3 shows the comparison between four different BLMs with and without these changes. The monitors were at equivalent locations in the north and in the south of HERAe. The changes reduce the background rate by a factor 200.

Two local bumps were driven with maxima close to the BLMs to study the response of the BLMs to showers; one in the north (BLM NR357; modified) and an equivalent bump in the south (SR357; unchanged). The lifetime of the beam and the local count rate of the BLMs were observed at different amplitudes of each bump. Note that the beam optic of HERAe at the two locations is the same. Figure 8.4 shows the results of this experiment. The count rate of the modified BLM were reduced by about a factor of 10 in respect to the unchanged one. Therefore the signal

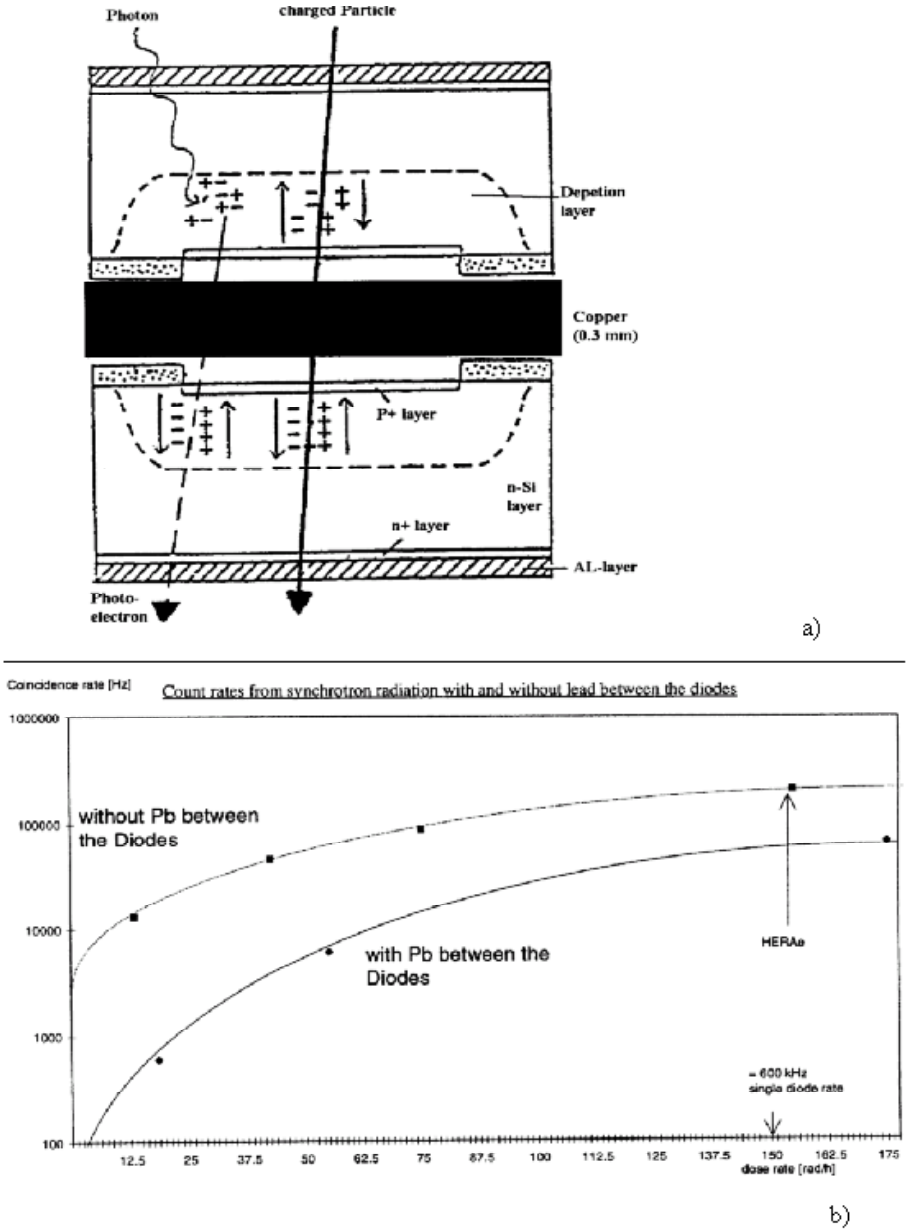


**Figure 8.1**: (from [33]): a) The copper inlay and b) the reduction of the background rates (actually it was measured with a lead inlay, but copper has the same effect!)

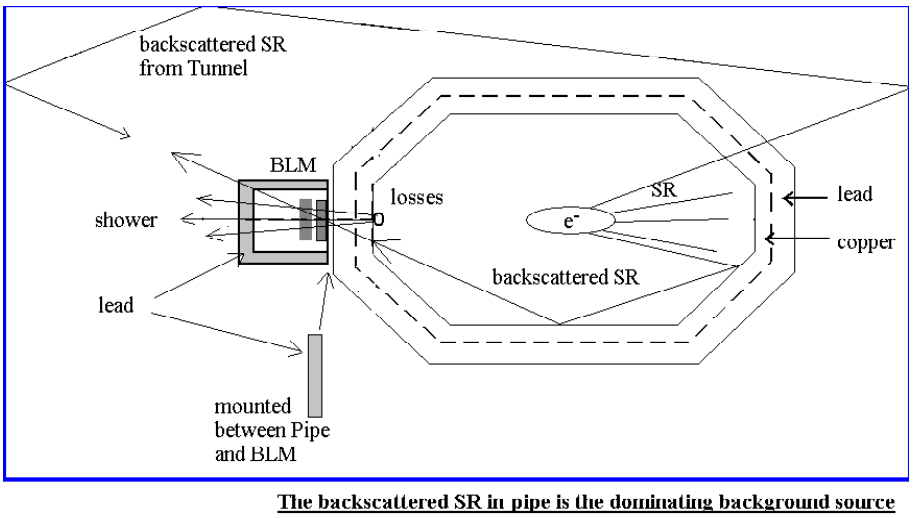


**Figure 8.2**: The directions of synchrotron radiation and losses.

to background ratio has been improved by about a factor 20 due to the modifications of the BLM.

These studies were done at a beam energy of 12 GeV, in order to keep the background level as low as possible. However, the result is valid for all energies, because the parameters of the shower particles reaching the BLMs depend only a little on the beam energy.

## 8.3 Conclusions

In order to improve the signal to background ratio of the HERAe BLMs, the following two steps where performed: 1) Installing a thin copper layer between the two PIN Photodiodes of the BLM to suppress coincidences coming from Photo and Compton electrons which make a signal in both diodes, and 2) adding a 12 mm lead layer between the beam pipe and the BLM.

These steps led to an improvement of the signal to background ratio by about a factor 20. Unfortunately, there was no time to study other combinations of lead shields, but the achieved improvement is sufficient to study the lifetime problem of HERAe in more detail.

## 8.4 Acknowledgements

We would like to thank Atoosa Meseck for her help in driving carefully the bumps. Mr. H. Schultz, F. Ridoutt, I. Kroupchenkow, M. Bieler and Ch. Montag did the soldering on all 250 BLMs. The help of MVA in dismounting and remounting all BLMs and lead shields is greatly acknowledged. Many thanks to Mark Lomperski for his very useful comments to the manuscript.

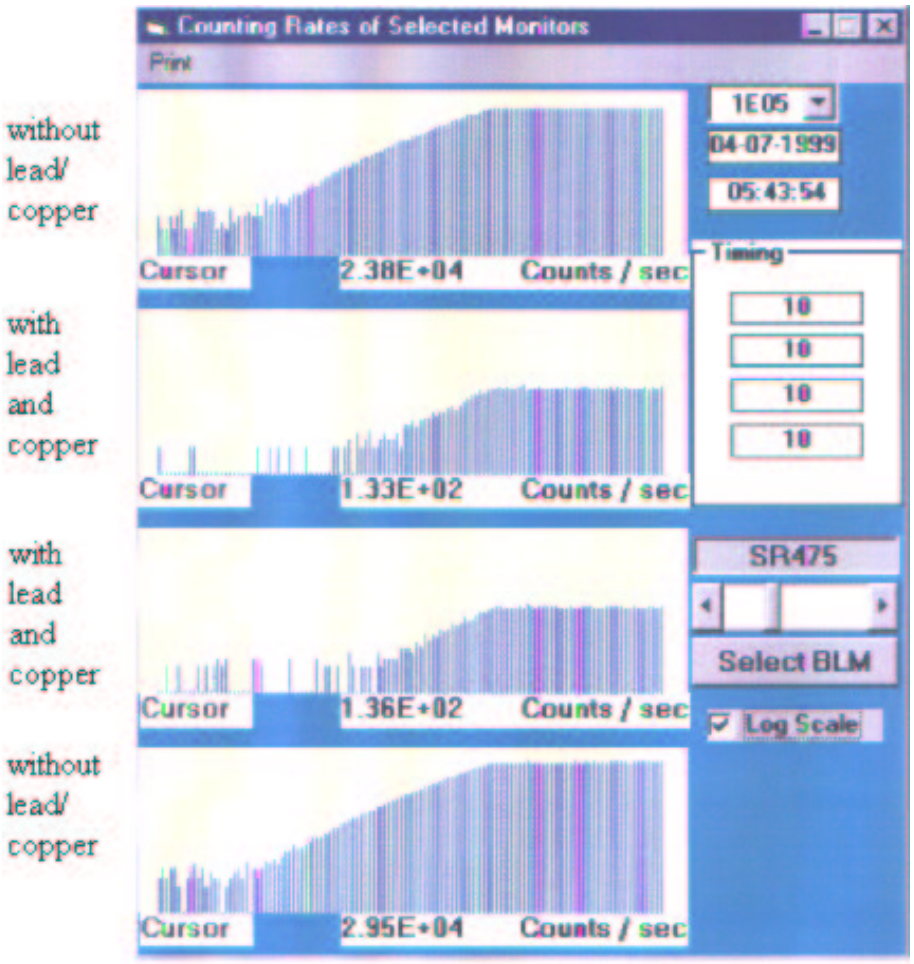


**Figure 8.3**: Four different BLMs during ramping of HERAe. The upper and lower one are unchanged BLMs while the two in the center are equipped with a copper layer between the diodes as well as an additional lead layer between the BLMs and the beam pipe. The numbers below each picture is the count rate at maximum. The scale is logarithmic.

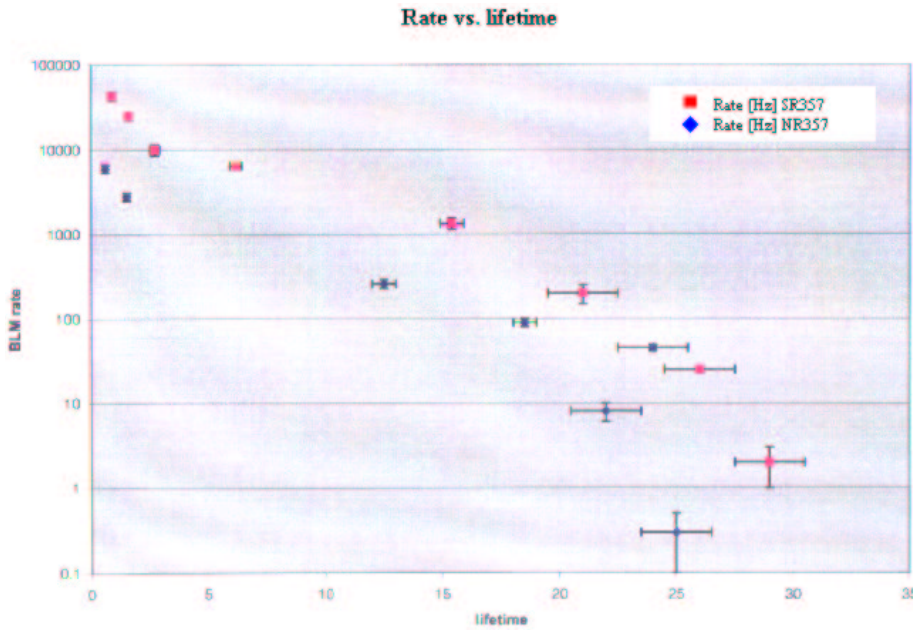


**Figure 8.4**: BLM count rates versus lifetime of the HERAe beam. The lifetime of the HERAe beam was adjusted by the amplitude of a local bump in the north or south region around the adjacent BLM, respectively.

# 9 Experiment zum transienten Beamloading im HERA Elektronenring

by M. Ebert, K. Rutsch, and F. Willeke, DESY Hamburg

Date: 1999, Apr. 29, 4pm–6pm, Logbook XXXVII, p. 59–65

## 9.1 Motivation

Wird der HERA-e Ring mit Elektronen betrieben, können im Prinzip Ionen im Strahl eingefangen werden, was zur Begrenzung der Strahllebensdauer, zum Aufblähen der Emittanz sowie zu Instabilitäten führen kann. Außerdem besteht der Verdacht, daß der Elektronenstrahl unter dem Einfang von Staubteilchen leidet. Beide Effekte sollten durch kurze Bunchzüge unterdrückt werden. Enthalten die kurzen Bunchzüge die gleiche Gesamtladung, so ist die Luminosität unabhängig von der Bunchzuglänge, zumindest solange die Strahl-Strahlgrenze für den Protonenstrahl nicht erreicht wird. Kurze, intensive Bunchzüge sind also ein wünschenswerter Betriebsmodus.

Allerdings wird bei großen Bunchlücken von bis 30% des Maschinenumfangs starkes transientes Beamloading beobachtet. Dies führt dazu, daß die einzelnen Bunche eine unterschiedliche Hochfrequenzamplitude und -Phase erfahren und sich damit eine Bunchpositions-abhängige synchrone Phase ergibt. Mit den üblichen Formeln werden für den HERA Luminositätsbetrieb mit 126 Bunchen ca. 11° Phasendifferenz erwartet.

Der HERA Elektronenring leidet unter starken Multibunchinstabilitäten, die durch die parasitische Impedanz der 82 Kupferkavitäten angetrieben werden und die nur durch ein aktives breitbandiges Rückkopplungssystem (longitudinales Multibunchfeedback) unter Kontrolle gehalten werden können. Die Dynamik ist bei der Digitalisierung der analogen Phasensignale auf ±1° begrenzt. Ein mittlerer, für alle Bunche gleicher Phasenoffset wird in analoger Weise vor der Digitalisierung elektronisch kompensiert. Bunchpositionsabhängige Phasenoffsets können nur bis ca. 10° kompensiert werden. Damit wird die Eingangsdynamik des digitalen Feedbacksystem effektiv um einen Faktor zwei reduziert. Der Verlust von 50% der Eingangsdynamik des Feedbacksystems führt zu Problemen bei der Elektroneninjektion. Deswegen muß bei kurzen Bunchzügen mit dem Ausbruch von Instabilitäten mit teilweisem oder totalen Strahlverlust gerechnet werden.

Aus dieser Problematik ergibt sich der Wunsch, die transienten Effekte zu kompensieren. Aus diesem Grunde wurden die Experimente, die hier beschrieben sind durchgeführt.

## 9.2 Strahlbedingungen bei dem Experiment

HERA-e wird normalerweise mit drei gleichlangen Bunchzügen gefüllt, die jeweils 63 Bunche im Abstand von 96ns enthalten und die auf den Bunchpositionen 1, 71 und

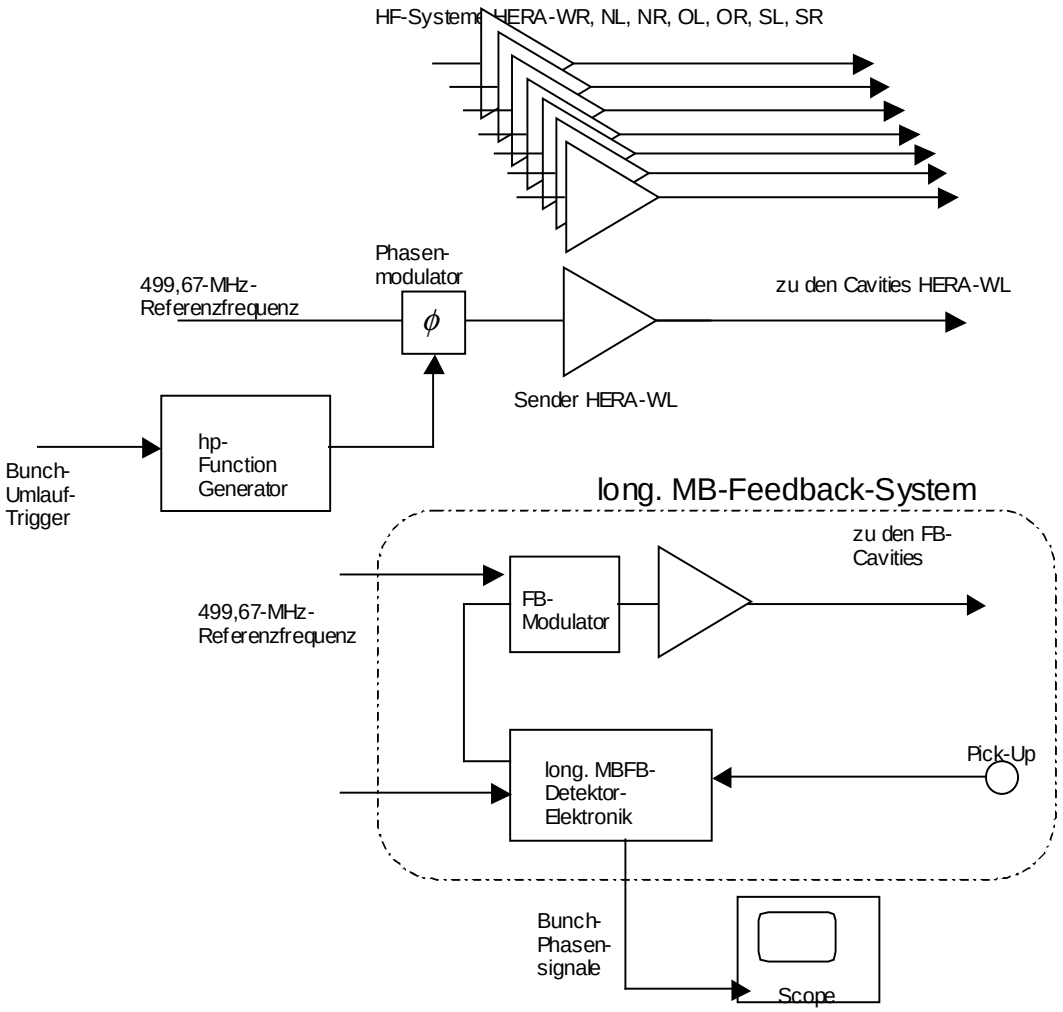


**Figure 9.1**: Prinzipskizze des Messaufbaus.

141 beginnen. Zwischen den Bunchzügen ergibt sich eine Lücke von 7 Leerbunchen und am Ende des dritten Bunchzuges eine größere Lücke von 16 Leerbunchen. In dem hier beschriebenen Experiment wurde der dritte Bunchzug weggelassen. Somit wurden 126 Bunche gefüllt. Die Länge der großen Lücke beträgt 87 Leerbunche. Die Experimente wurden bei einer Strahlenergie von 12GeV durchgeführt. Die Strahlintensität betrug zwischen 25mA und 40mA. Gemäß den üblichen Formeln beträgt die maximale Phasendifferenz zwischen den Bunchen ca. 8° bei 30mA Strahlstrom in 126 Bunchen.

$$\Delta\Phi = \frac{1}{2}\frac{R_s}{Q}\frac{\omega_{RF}}{U_0} I_B (T_r - T_B) = 8.15^\circ \ , \tag{9.1}$$

$$R_s = 1.7 G\Omega \ , \quad Q_{ext} = 9000 \ , \quad \omega_{RF} = 2\pi \cdot 500\text{MHz} \ , \tag{9.2}$$

$$U_0 = 94\text{MV} \ , \quad I_B = 30\text{mA} \ , \quad T_r = 21\mu\text{s} \ , \quad T_B = 12.5\mu\text{s} \ . \tag{9.3}$$

($\Delta\Phi_{max}$: maximale Phasendifferenz zwischen Bunchen, $R_s$: totale Shuntimpedanz, $Q$=Gütefaktor, $\omega_{rf}$: HF Kreisfrequenz, $U0$: Umfangsspannung, $I_B$: Bunchstrom, $T_r$:Umlaufzeit, $T_B$: Länge des Bunchzuges, Referenz: [34].)

## 9.3 Durchführung und Resultate

Der Sender WL wurde in seiner Phase mit einem umlaufsynchronen, verzerrten sinusförmigen Signal moduliert. Ziel ist die effektive Cavitiyspannung für die ersten Bunche durch eine negative Phasenverschiebung zu reduzieren. Dabei wird versucht einen möglichst sägezahnförmigen Verlauf zu erzielen. Die Bandbreite der Cavities beträgt ca. 60kHz. Die Phasenmudulationstiefe betrug ±30°. Der Sender wurde leistungsgeregelt bei 800kW betrieben. Die Summe der Cavity Spannungen betrug 20MV. Das Modulationssignal wurde in Amplitude und Verzerrungsgrad optimiert, um eine möglicht gleichmäßige HF-Phaselage aller Bunche zu erzielen. Mit einer optimalen Modulationstiefe von ±30° konnte die Phasendifferenz zwischen den Bunchen um (30-40)% reduziert werden. Bei diesen Versuchen fällt jedoch der Sender WL mehrfach mit einer Cavity Vakuummeldung aus. Das Cavityvakuum steigt bis auf 10-6mbar.

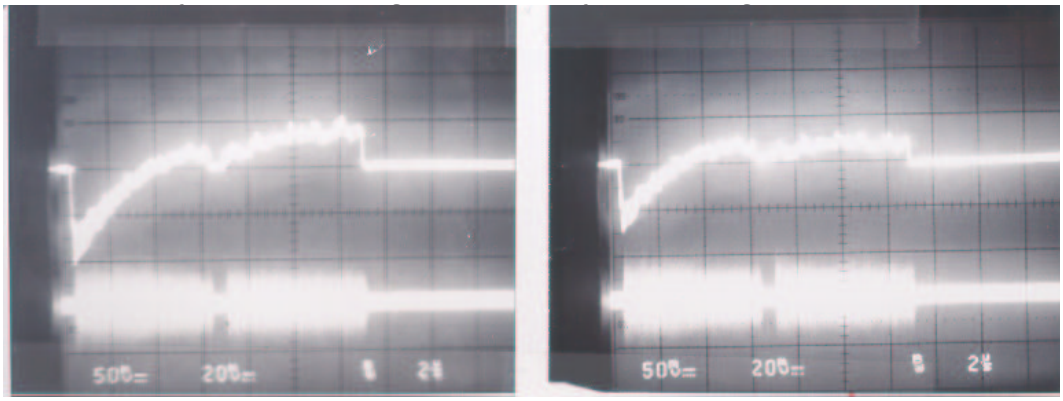

**Figure 9.2**: Die beiden Photos zeigen Oszillographenaufnahmen der Bunchphasen: Die obere Spur zeigt die mittlere Phase entlang des Bunchzuges, die untere Spur zeigt die Phasenozillation um die mittlere Phase. Das linke Bild zeigt die Phasenvariation ohne Kompensation, das rechte Bild zeigt die Phasenvariation mit Kompensation. Die Phasenmessung ist nicht kalbriert. Der Phasenhub im linken Bild sollte laut Rechnung ca. 8° betragen. Durch die Kompensation reduziert sich des Phasenhub um etwa die Hälfte.

## 9.4 Zusammenfassung

Durch Umlauf-synchrone Modulation der Phase des Senders WL läßt sich die maximale Phasendifferenz zwischen den Bunchen eines kurzen Bunchzuges von 126 Bunchen mit einer Lücke von 8sec von etwa 8° auf 5° reduzieren. Durch die Modulation des Senders kommt es zu Vakuumeinbrüchen in den Cavitäten, vermutlich durch Überschläge im Kopplerbereich. Um eine praktikable Kompensation zu erzielen,

müßten vermutlich alle Sender moduliert werden, um die Belastung jedes einzelnen Systems zu minimieren. Um vollständige Kompensation zu erreichen, müßten die Sender auch in ihrer Amplitude moduliert werden.

# 10 Measurement of the Beta Function and the Dispersion in the HERA Proton Ring

by Bernhard Holzer and Atoosa Meseck, DESY Hamburg

Date: 1999, Dec. 13, 3pm to 11pm, Logbook XXXXI, p. 25–27
Date: 1999, Dec. 16, 4pm to 6pm, Logbook XXXXI, p. 47–48

In the double ring collider HERA the two counter rotating beams are guided and focused in separate magnetic lattices. Only a small number of common magnets are acting on both beams to establish the separation scheme needed in the two interaction regions NORTH and SOUTH. The spot sizes of the electron/positron and of the proton beam have to be matched therefore in a dedicated way and in contrast to the "conventional" single ring colliders, errors in the machine optics lead not only to a change in the luminosity but to unwanted distortions in the interaction of the two beams. Therefore the beta function and the dispersion function in the HERA proton ring was studied.

In the run year 1999 during several occasions therefore the beta function of the two beams was measured. Previous results, obtained from measurements at the proton mini beta magnets (the so called "QR14, QS10 quadrupole lenses") indicated a possible error of the beta functions in the two interaction regions. During the machine studies in December 1999 this topic was studied in more detail.

The beta function was measured in both planes at the proton low beta quadrupoles, where due to the high beta values of up to $\beta \approx 2000m$ the beam is most sensitive to measurements. Moreover it was measured at the location of the HERA wire scanners as for studies of the transverse shape of the proton beam the exact value of the beta function at the wire position was needed.

In addition, measurements of the HERA-B experiment installed in hall WEST of HERA indicate that a possible mismatch of the dispersion function might be present in the proton ring: First results of the reconstructed hits of the proton beam at the wire target show a slightly asymmetric pattern in the outer and upper wire target of HERA-B: See figure 10.1. A possible explanation of the effect would be a distortion in the machine optics affecting the horizontal and vertical dispersion functions.

As the asymmetry of the hit distribution shown in the plot is mainly determined by "empty bucket" contributions, i.e. by reactions coming from buckets that should not be filled by particles, a possible source of the hits would be unbunched protons that left the bucket and are drifting slowly outside the machine. They would drift on dispersive orbits due to the constant energy loss they suffer and would be a possible explanation of the pattern shown in the figure. Therefore in addition to the measurement of the beta functions at dedicated positions in the ring a measurement of the dispersion function has been performed to study the problem.

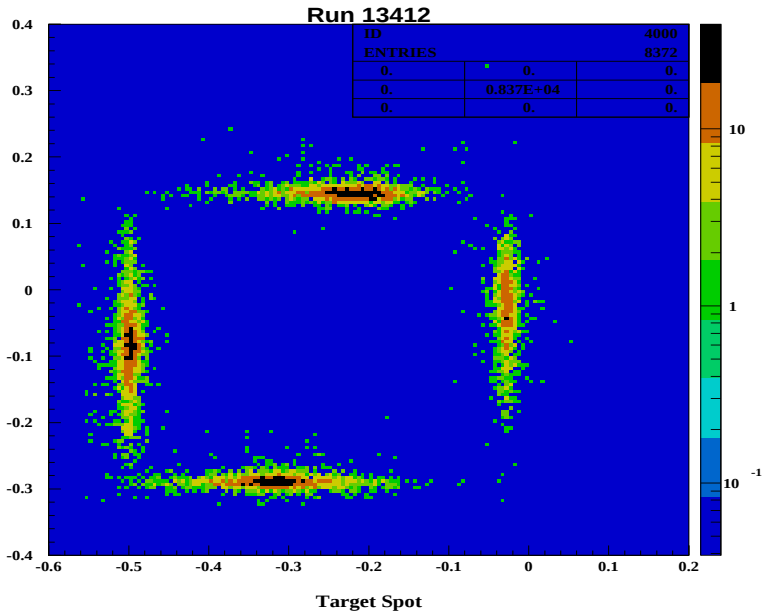


**Figure 10.1**: Reconstruction of hits at the HERA-B wire target. The hit distribution shows a slight asymmetry which is mainly dominated by particles from "empty bucket" locations being not kept inside the proton RF separatrix. A slight mismatch of the dispersion functions in the ring would be a possible explanation of the pattern.

## 10.1 Measurement of the Beta Function

The measurement of the beta function was done in the usual way by changing single powered quadrupole lenses in the machine and measure the effect on the tune in both planes. Protons were accelerated to 920 GeV beam energy and put to the luminosity file. To avoid unwanted perturbations of the measurement due to the beam beam interaction, no electrons or positrons were filled in the lepton ring. However the synchronization of the two rings was active to center the proton beam orbit and to establish luminosity conditions in the usual way. Beside of that however no special orbit corrections were performed as it was decided to study the optics under "routine conditions."

In figure 10.2 the theoretical proton beam optics is shown in the straight section SOUTH or NORTH. The quadrupole lenses used for the measurement are named in the figure: The horizontal focusing magnet *QR14* and the vertical lens *QS10*. In the case of the horizontal lenses 6 magnets of the same type are acting in series, 3 per side. The three vertical acting half quadrupoles *QS10* are supported by one conventional quadrupole type *QR10* and all in all 8 magnets are used to focus the beam in the vertical plane.

A gradient error due to a change of the current in a quadrupole lens leads to a shift in the tune of the stored beam. The tune shift $\Delta Q$ is proportional to both the magnitude of the applied gradient change and the value of $\beta$ at the location of the magnet.

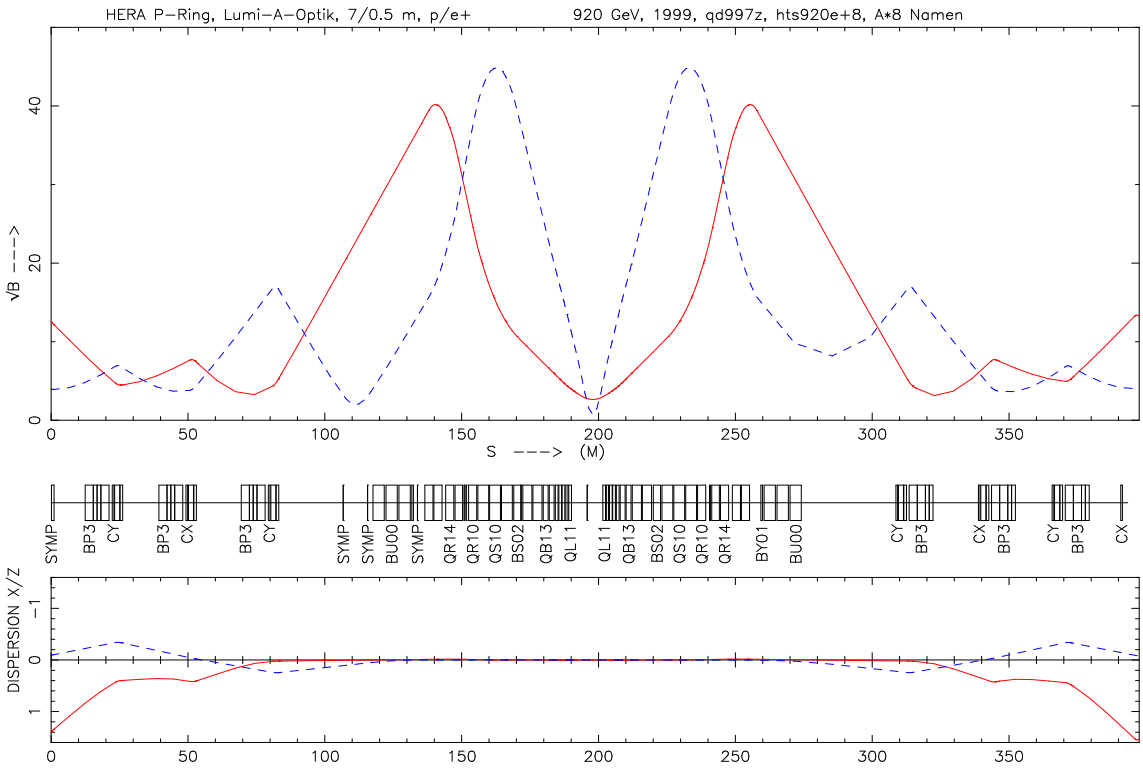


**Figure 10.2**: Proton beam optics for the luminosity case. The plot shows the theoretical optics in the horizontal (solid line) and vertical plane (dashed line) in the straight sections NORTH or SOUTH of the HERA proton machine. In the lower part of the figure the magnetic lattice is shown with the name conventions of the quadrupole lenses used for the measurements.

$$\Delta Q = \frac{1}{4\pi} \oint \beta(s) \Delta K(s) ds$$

The K-value represents in the usual way the gradient of the magnet normalized to the particle momentum. $K = \frac{g}{p/e}$ . The result of the measurements are shown in the next figures. The horizontal axis shows the current in the corresponding quadrupole lens. The vertical axis indicates the measured tune which is proportional to the beta function: The calibration of a QR-type quadrupole magnet used for this measurement is given by the formula

$$\eta = \frac{I}{K * L * p} = 22.44$$

Here the usual units for the current I [A], the normalized quadrupole strength K $\frac{1}{m^2}$ and the momentum p $\frac{GeV}{c^2}$ are used. L is the length of the magnet in meter. Given the formula for the tune shift from above, the product of the current change applied and the beta function at the position of the $n$ quadrupole lenses is obtained as

$$\Delta I * \beta = \frac{\Delta Q * \eta * p * 4 * \pi}{n}$$

| Position | experimental results | | theoretical values | | | |
|---|---|---|---|---|---|---|
| | $\beta_x[m]$ | $\beta_y[m]$ | $\beta_x[m]$ | $\beta_y[m]$ | $\frac{\Delta\beta_x}{\beta_x}$ | $\frac{\Delta\beta_y}{\beta_y}$ |
| QR14-NORTH | 1246 | 330 | 1472.4 | 439.2 | 0.154 | 0.248 |
| QR14-SOUTH | 1221 | 366 | 1472.4 | 439.2 | 0.171 | 0.166 |
| QS10 NORTH | 287 | 1444 | 273.2 | 1825.6 | 0.051 | 0.209 |
| QS10 SOUTH | 287 | 1516 | 273.2 | 1825.6 | 0.051 | 0.169 |
| QR24 WEST | 110 | 80 | 114.2 | 105.7 | 0.037 | 0.243 |
| QR54 WEST | 38 | 183 | 27.7 | 293.8 | 0.371 | 0.377 |
| QR56 WEST | 240 | 28 | 234.6 | 20.1 | 0.010 | 0.400 |

**Table 10.1**: Summary of the measured beta functions compared to the theoretical values.

In the plots shown below the tune $Q$ obtained for a given current is plotted versus the current, that had been applied. The points in the plot represent the measured values, the lines are linear fits to the data.

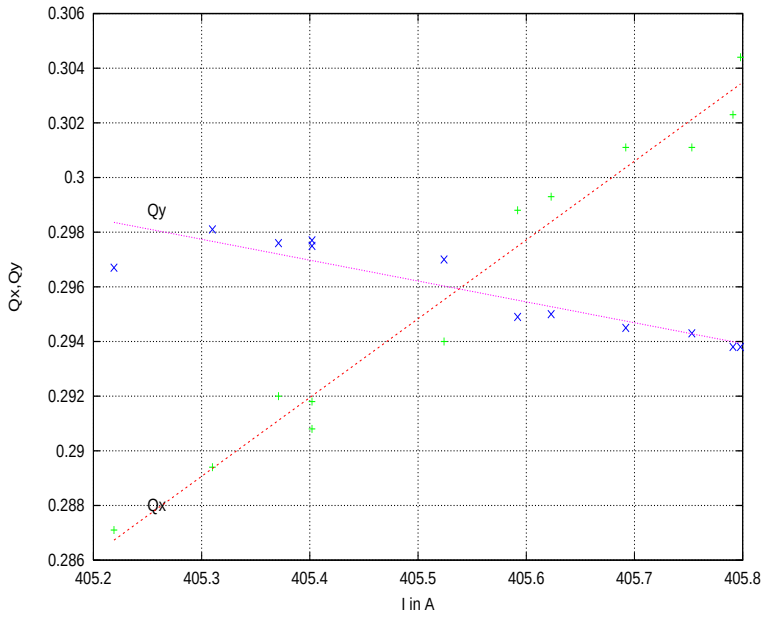


**Figure 10.3**: Result of the measurement of the HERA beta function in the quadrupole lens "QR14-North". Plotted are the tune values measured as a function of the current applied in the quadrupole magnet.

For the measurements at the proton wire scanner the quadrupole lenses QR24, QR54 and QR56 are used. Figure 10.8 shows the optical parameters in that region. The wire scanner in the horizontal plane is located at WR 124m, for the vertical plane at WR 84m.

The results of the measurement are summarized together with those of the mini beta insertion mentioned above. The table shows in addition the theoretical values of the beta function and the relative error $\Delta\beta/\beta$.

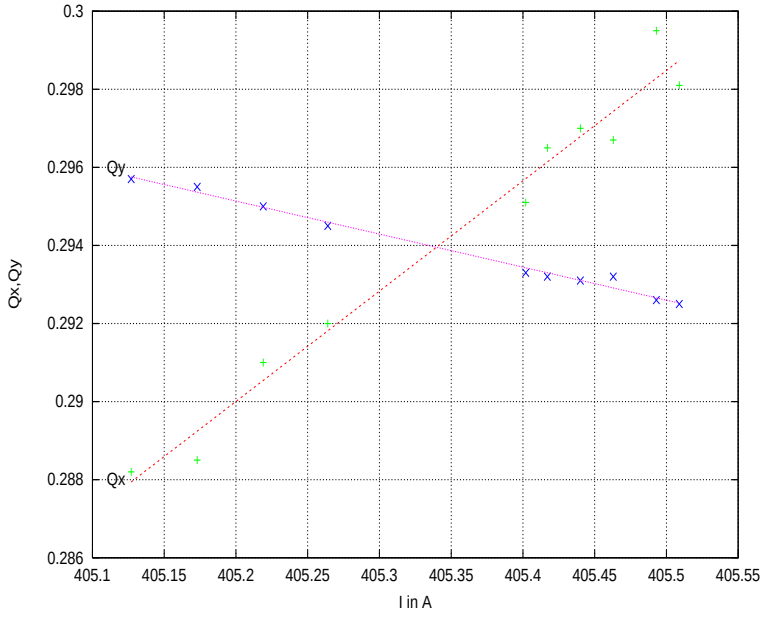


**Figure 10.4**: Measurement of $\beta$ in quadrupole lens "QR14-SOUTH".

## 10.2 Measurement of the Dispersion Function

For the measurement of the dispersion function in HERA-p the rf-frequency of the machine was shifted and the resulting orbit displacement was measured. During normal luminosity conditions the rf-frequency of the proton ring has to be locked to the rf-system of the electron ring to center the two stored beams in the longitudinal direction at the interaction regions NORTH and SOUTH. For the measurement of the dispersion however this would restrict the applicable frequency shift needed. Therefore the so-called e/p-synchronization was switched off during the measurement. The proton RF was shifted from its design value in steps of 100 Hz to about 500 Hz and after each step the resulting orbit displacement was measured for the complete ring in both transverse planes. For a constant magnetic field the momentum of the particle beam is related to the frequency shift applied via the momentum compaction factor $\alpha = (\frac{1}{\gamma_{tr}})^2$.

$$\frac{\Delta f_0}{f_0} = \frac{\Delta p}{p} * (\frac{1}{\gamma^2} - \frac{1}{\gamma_{tr}^2})$$

For the luminosity case where the beam energy is 920 GeV the contribution of the first term can be neglected and

$$\frac{\Delta f_0}{f_0} = -\frac{\Delta p}{p} * \alpha$$

In HERA the momentum compaction factor is in the luminosity optics $\alpha = 1.28 * 10^{-3}$. For the given momentum deviation the beam will run on a dispersive orbit which is shifted with respect to the nominal orbit by

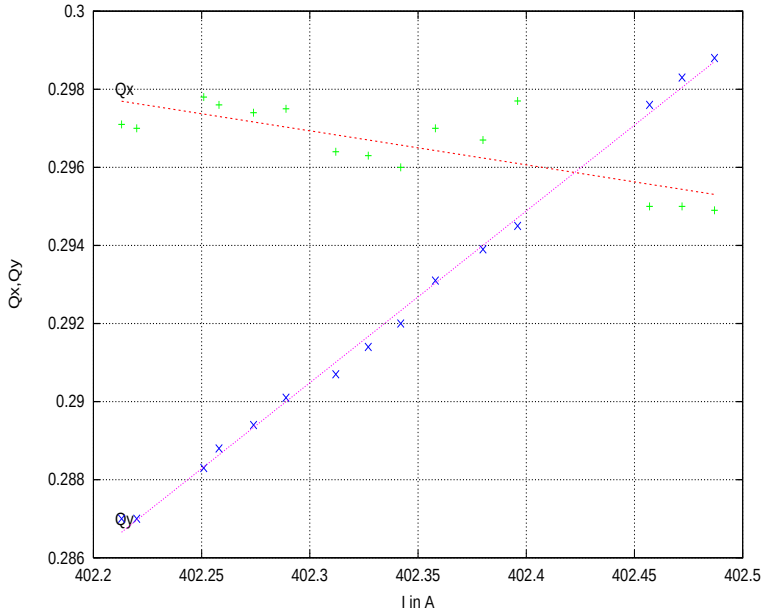


**Figure 10.5**: Measurement of $\beta$ in quadrupole lens "QS10-NORTH".

$$\Delta x = D_x * \frac{\Delta p}{p}$$

From the difference orbits therefore the dispersion function can be calculated at each beam position monitor in the ring. The result is shown in figure 10.11 for the horizontal and in figure 10.12 for the vertical plane. The solid line is connecting the measurement points that refer to beam position monitors. The dashed line represents the theoretical curve for the ideal machine. The error bars indicate the fluctuation of the measurement result for the different steps of the RF frequency shift that had been performed.

As explained in the introduction to this articles, the horizontal and vertical dispersion of the HERA proton ring is of special interest at the point where the proton beam is interacting with the wire target of the HERA-B experiment. In figure 10.11 and 10.12 the number of the beam position monitor is used as the horizontal axis. The relevant BPM in the case of HERA-B is monitor number 127 which is located at position WR-10m in the ring lattice. As can be seen in the plots the resulting dispersion at this position is $D_x = -892mm$ and $D_y = -228mm$ in the horizontal and vertical direction. The table below shows the measured and the expected theoretical values of the dispersion function at the HERA-B wire target.

In simulations with the program PETROS the dispersion was calculated in both planes for a non ideal machine (F. Stulle, priv. com.): Transverse misalignments of the quadrupole magnets had been assumed of about $\Delta x \approx \Delta y \approx 0.15mm$ at 1 $\sigma$ of a Gaussian error distribution, and a roll angle of $\Delta\alpha \approx 0.066mrad$. The relative error of the quadrupole strengths in the simulation was $\Delta k/k = 7 * 10^{-5}$. These misalignments are within the range of the tolerances assumed for the real machine. The resulting orbit has been corrected in the simulation using 15 correctors in both

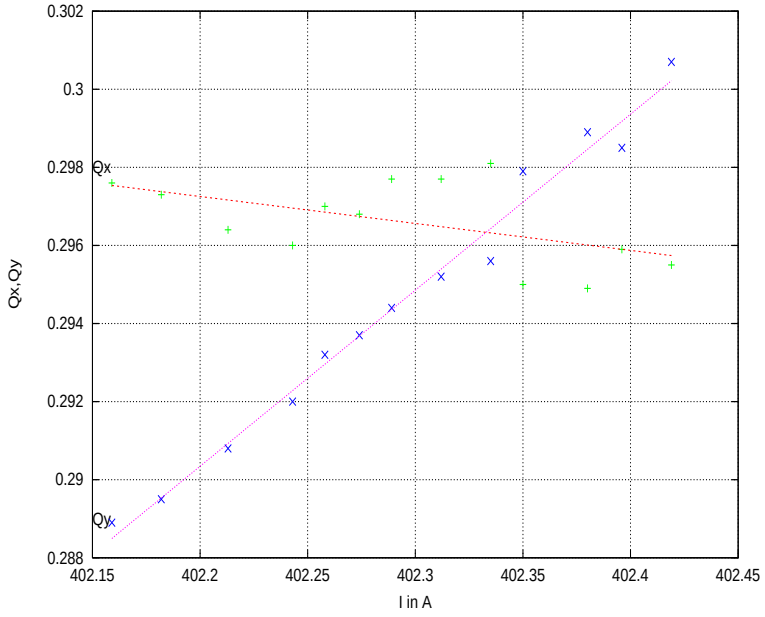


**Figure 10.6**: Measurement of $\beta$ in quadrupole lens "QS10-SOUTH'.'

| | measured values | theoretical values |
|---|---|---|
| hor. Dispersion | -89.2 cm | -50.3 cm |
| vert. Dispersion | -22.8 cm | 0.0 cm |

**Table 10.2**: Measured Dispersion in horizontal and vertical plane in the HERA proton ring. The values refer to the position WR-9m, where the HERA-B wire target is installed. The results for the complete machine is shown in figure 10.11 and 10.12.

planes and afterwards the dispersion was determined. In figure 10.13 the orbit in both planes for the distorted machine is plotted after the correction and in figure 10.14 the dispersion function is shown.

We conclude that at least a part of the measured dispersion values obtained in both planes could be explained by tolerances in the alignment and strength of the magnets. It is proposed therefore to repeat the measurement of the dispersion function, after a careful correction of the orbit. It cannot be excluded at that moment that a part of the dispersion beat is resulting from an additional source i.e. a mismatch of the optics in the ring.

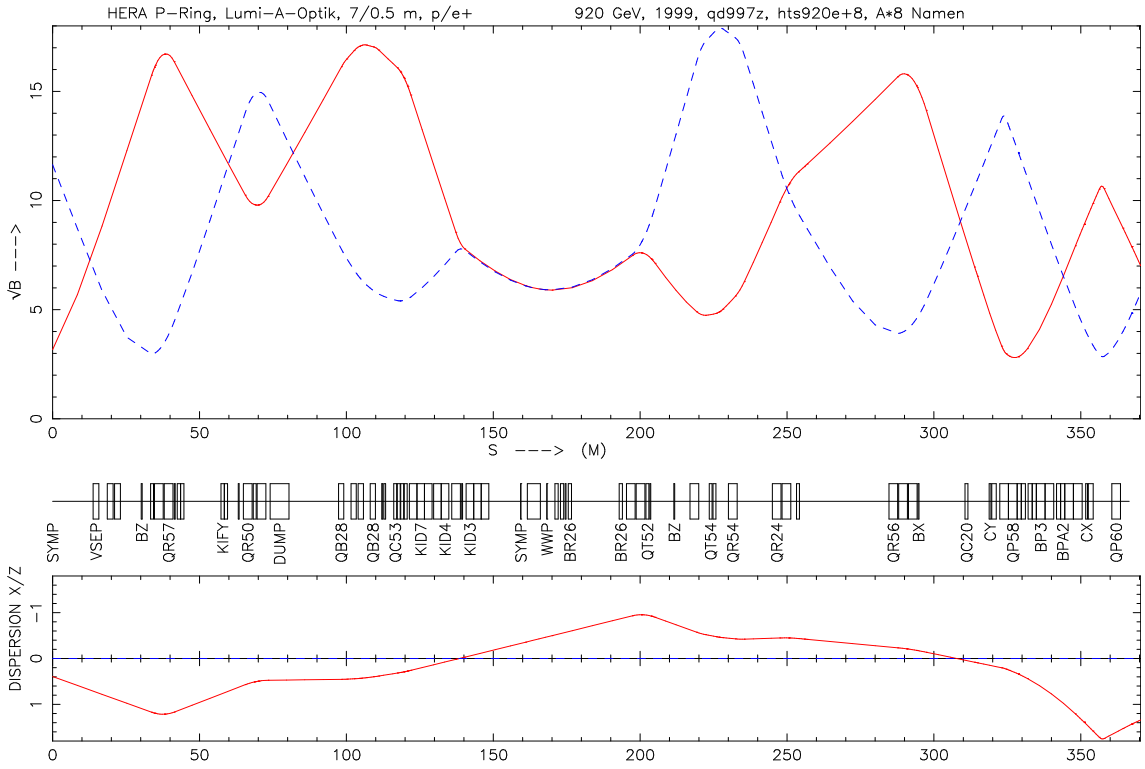


**Figure 10.7**: Beta function in the straight section WEST where the wire scanners are installed. The horizontal scanner is at position WR 124 m, the vertical one at position WR 86m.

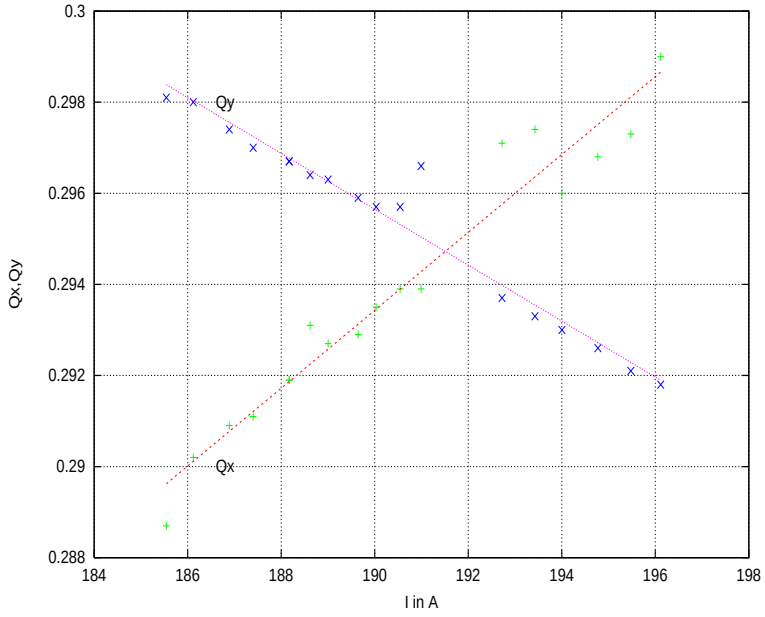


**Figure 10.8**: Measurement of $\beta$ in quadrupole lens "QR24-WEST".

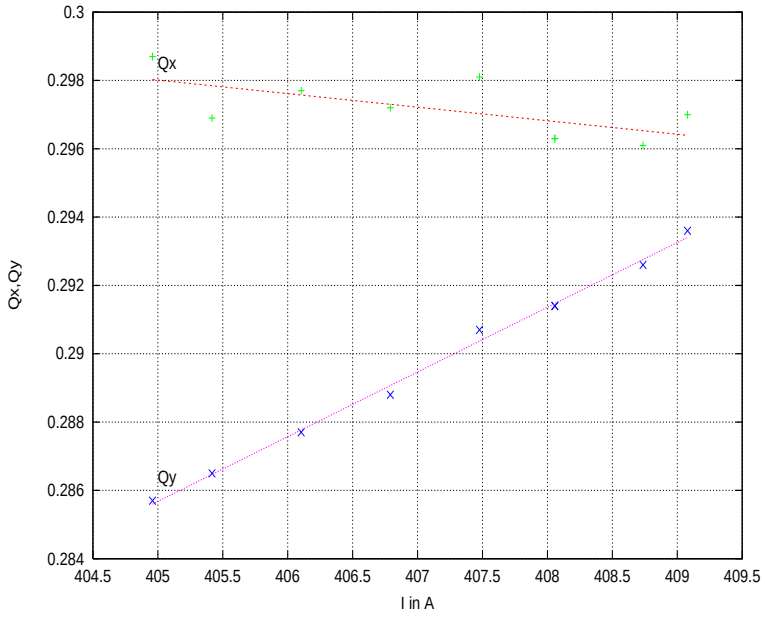


**Figure 10.9**: Measurement of $\beta$ in quadrupole lens "QR54-WEST".

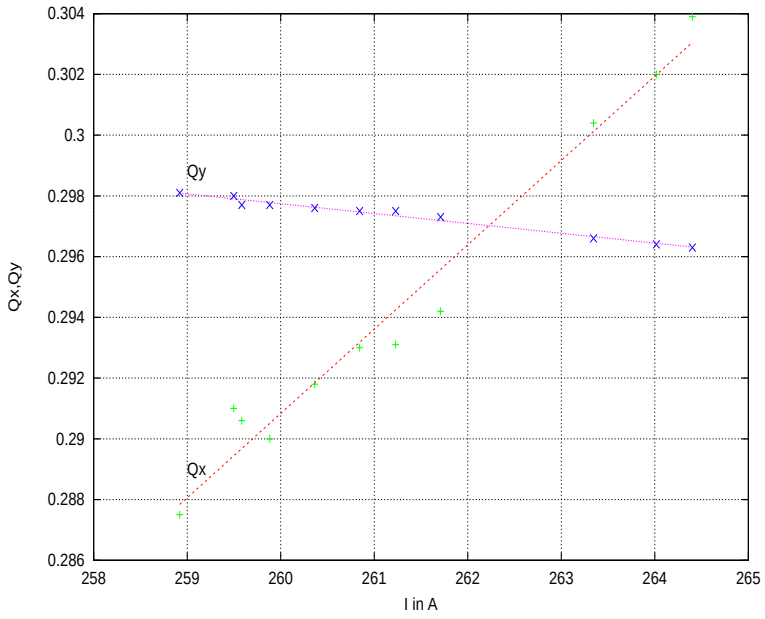


**Figure 10.10**: Measurement of $\beta$ in quadrupole lens "QR56-WEST".

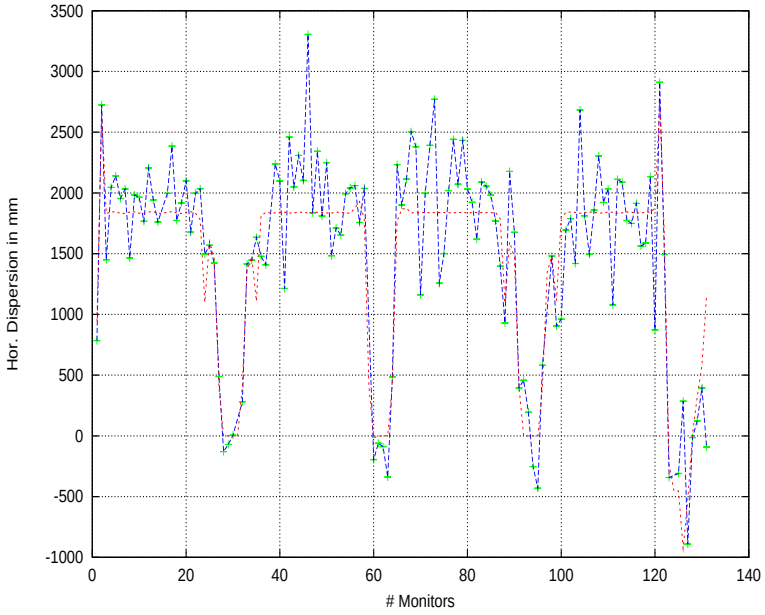


**Figure 10.11**: Result of the measurement of the horizontal dispersion function in the HERA proton ring. Plotted is the measured value of the dispersion at the beam position monitors. These values are connected by a solid line to guide the eye. The dashed line connects the theoretically expected values of the dispersion – again at the BPM locations.

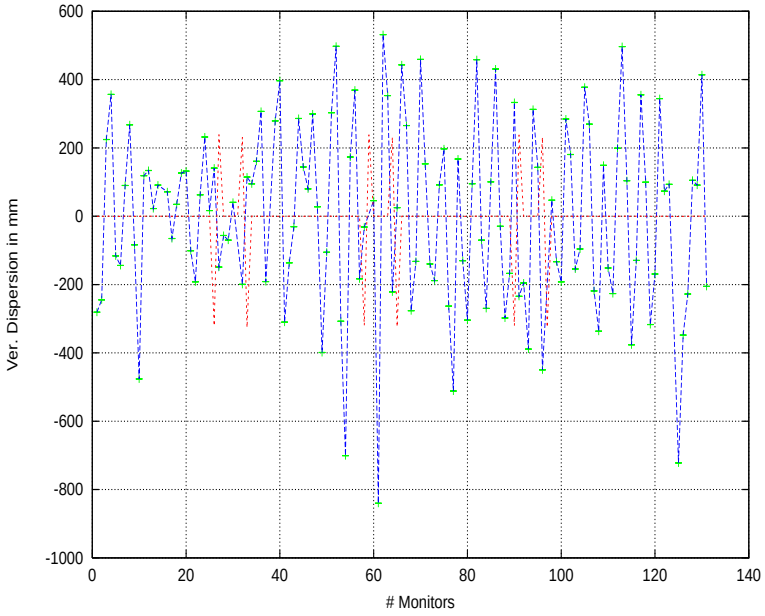


**Figure 10.12**: Result of the measurement of the vertical dispersion function in the HERA proton ring. Plotted is the measured value of the dispersion at the beam position monitors. These values are connected by a solid line to guide the eye. The dashed line connects the theoretically expected values of the dispersion – again at the BPM locations.

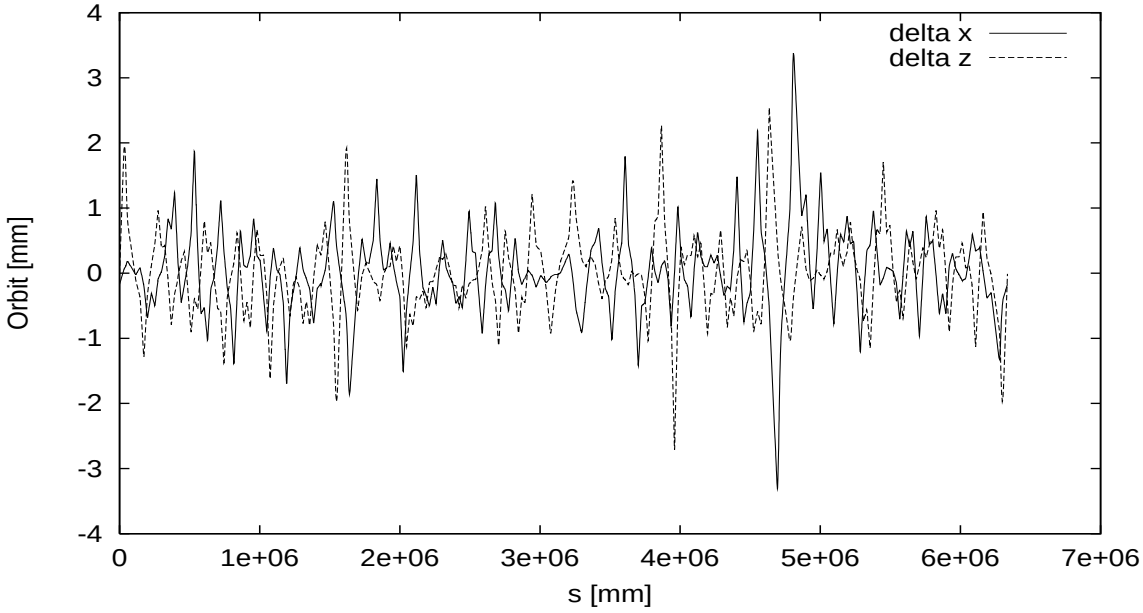


**Figure 10.13**: Result of a simulation or the HERA proton beam orbit for a distorted machine. A Gaussian error distribution has been assumed for the transverse misalignment of the quadrupole lenses, their roll angle and their strengths. Afterwards an orbit correction had been applied. The remaining orbit distortions are reflected by the beat of the dispersion functions shown in the next figure.

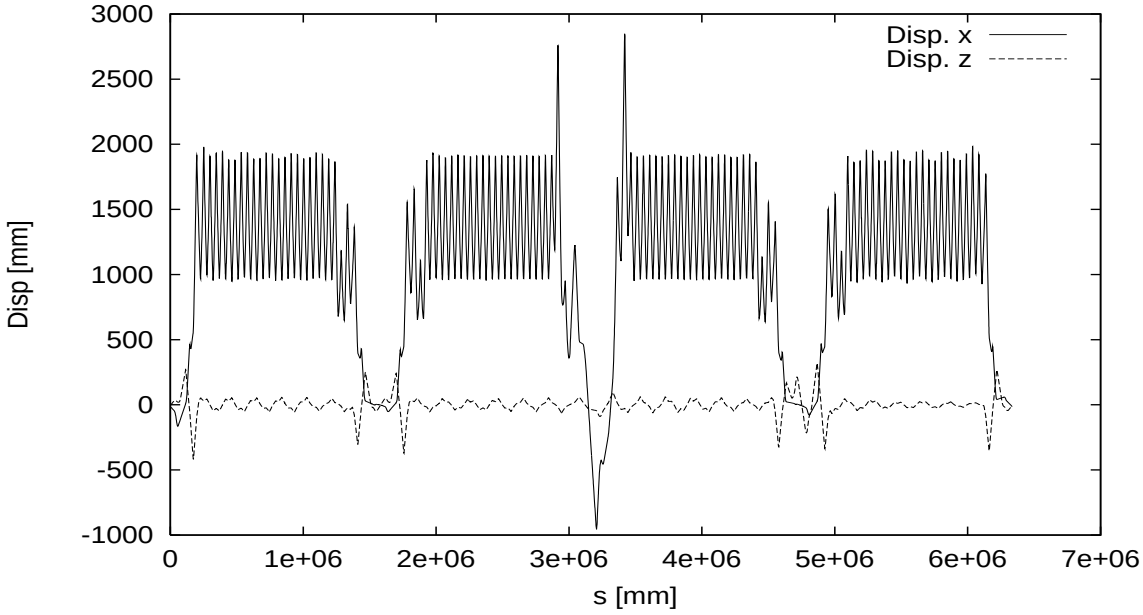


**Figure 10.14**: Dispersion function for the horizontal (solid line) and vertical plane (dashed line) calculated for the distorted machine as described in the previous figure.

# 11 Comparison Between Coasting Beam at 820GeV and 920GeV

by S. Spratte, University of Dortmund

Date: 1999, May 1, 0am to 6am,Logbook XXXVII, p. 74–75

Coasting beam inside the HERA proton ring is observed and monitored by the HERA–B target group since 1997. Coasting beam does not only disturb the HERA–B trigger system which relies on bunched proton interactions, but it also shows a correlation with high and spiky background conditions at the other experiments. Measurements have been carried out to solve these problems and to detect the source of the coasting beam.
One possible source of coasting beam is the proton synchrotron radiation. In this case different proton energies should have an impact on the amount of coasting beam. An 820GeV run was performed during machine studies in order to compare the coasting beam production with that of 1999 at 920GeV. If the coasting beam production differs significantly, the proton synchrotron radiation would be a source for the production of coasting beam. Data collected with the HERA–B wire target at proton energies of 820GeV in 1997 are also presented to verify the results.

## 11.1 Introduction

The HERA–B target group uses the Flash ADC system MPFA40 [35] to measure and to monitor the contribution of individual bunches to the interaction rate. This FADC system samples the time structure of the interaction rate that is measured by scintillator counters with the fourfold bunch crossing frequency of 41.67 MHz. Therefore every 24 ns a signal is recorded. 880 bytes per readout cycle of the FADCs are recorded to study the interactions in a time slice of a complete HERA turn of 21.12 $\mu$s. A rate of 70 Hz is achieved for the read out. 5000 succeeding measurements are summed up in order to get reasonable statistics. This leads to bunch contribution measurements that are averaged over a time of about one minute.

Figure 11.1 shows the averaged number of interactions in time intervals of 24 ns. In this case an interaction rate of about 10 MHz was produced by an *inner* wire: The HERA bunch structure is clearly visible.

The timing was adjusted in such a way that interactions from the first bunch are located at sample number 61.

In contrast one observes a different time structure for interactions that are produced by the *outer* wires. Figure 11.2a) shows a comparable measurement but for an outer target wire at an interaction rate of about 30 MHz. In addition to the bunched signal as shown by the inner wires, the outer wires also exhibit a significant amount

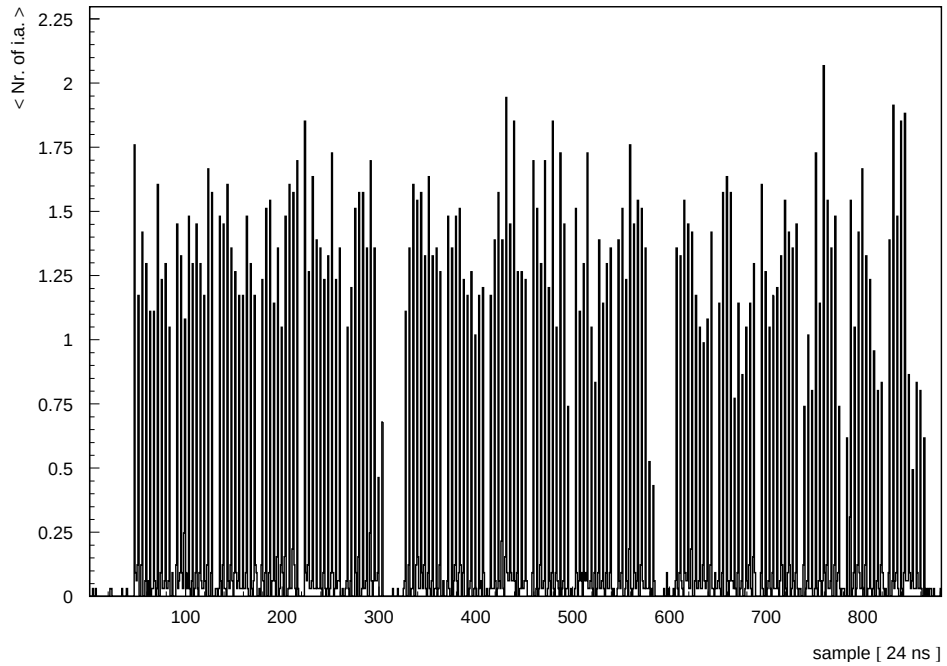


**Figure 11.1**: Measurement of the bunch contribution to the HERA–B interaction rate in 24 ns intervals for the complete HERA ring. The first bunch is located at sample number 61.

of continuous background to the interaction rate. These interactions are not correlated with filled proton bunches and they are distributed equally along the complete HERA ring. For example, clear signals can be observed at samples 1 to 60 where the kicker gap is located. Also between the individual bunches interactions take place on the target wire. The continuous background is interpreted as the coasting beam DC component of the proton beam. If an outer wire is positioned at a distance larger than $6\sigma$ from the beam center, then the bunch correlated interactions typically completely disappear. Only the DC component is left, as it is shown in figure 11.2b). Hence the FADC measurement allows to differentiate between interactions coming from protons outside the filled buckets and bunch correlated interactions.

All observations concerning coasting beam inside the HERA proton storage ring can be explained by discussing the particle trajectories in the longitudinal phase space of protons with an energy deviation $\frac{\triangle E}{E} < 0$: If the energy deviation is larger than the maximum energy deviation allowed for the stable longitudinal phase space, the protons will cross the separatrix; that means they will leave the stable bound region defined by the RF–voltage. In case of the HERA proton storage ring the energy deviation of the unbunched protons from the centroid particle is larger than $2 \cdot 10^{-4}$... $3 \cdot 10^{-4}$ allowed for the stable longitudinal phase space depending on the used RF–voltage. The negative horizontal dispersion $D_x$ of the HERA proton optics at the location of the wire target lead to a transverse offset $x = D_x \frac{\triangle E}{E} > 0$ for the

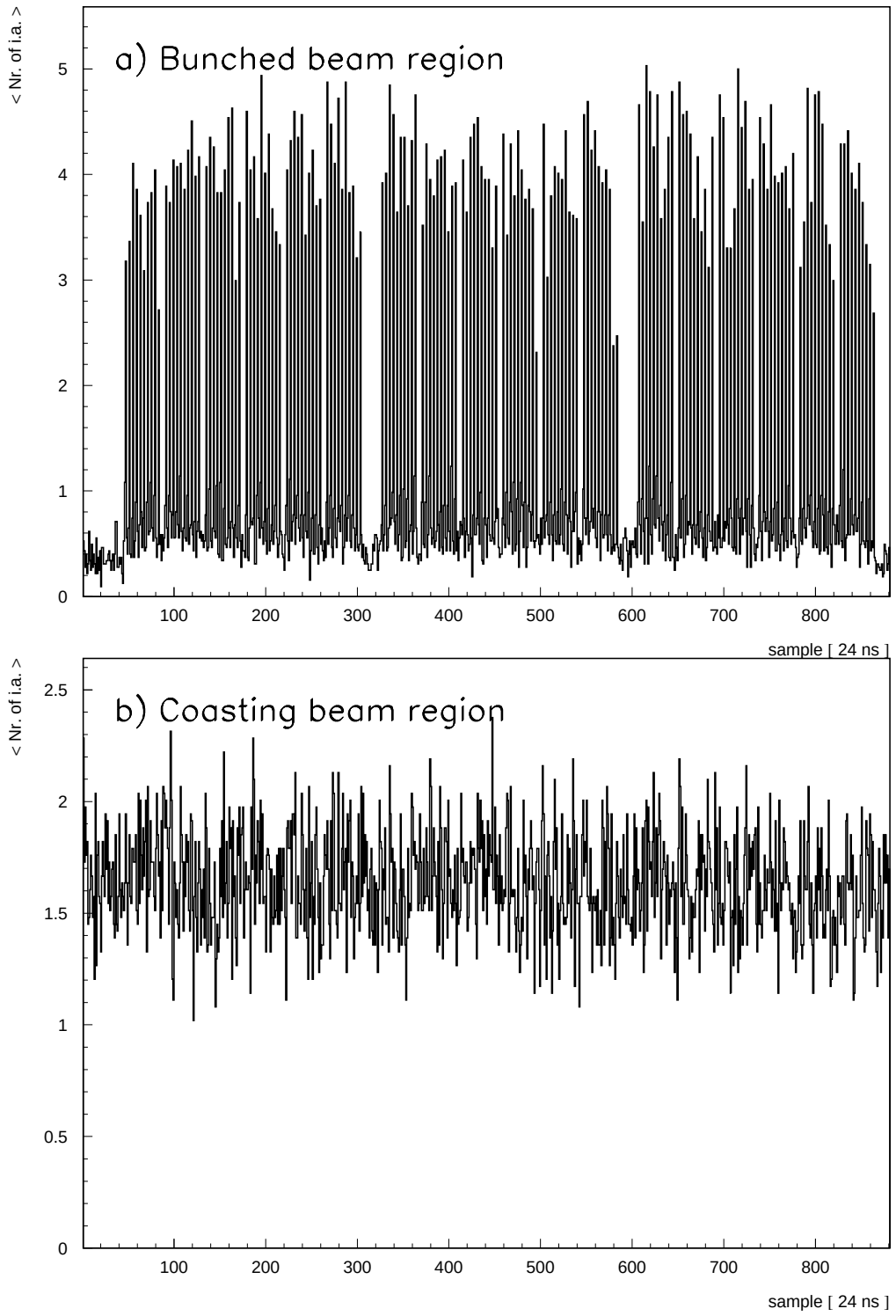


**Figure 11.2**: The time structure of the proton interaction for an outer target wire at different distances of the wire to the beam center: a) wire $\approx 4\sigma$ from the beam center and b) wire $\geq 6\sigma$ from the beam center.

coasting protons. They are shifted to the outer side. A more detailed discussion can be found in [36].

As a consequence, the outer transverse beam region at the target location can be divided into two different parts observed at different wire positions relative to the beam center $\triangle x_{wire-beam}$. There is no sharp border between these two regions and a border can therefore be specified only approximately:

- *Coasting beam region ($\triangle x_{wire-beam} > \approx 6\sigma$)*
  This region is characterized by a uniform time structure for the proton interactions with the wire (figure 11.2b)).

- *Bunched beam region ($\triangle x_{wire-beam} < \approx 6\sigma$)*
  This region is characterized by a time structure with clearly bunch correlated interactions that are superimposed by a fraction of continuous background of coasting beam (figure 11.2a)).

Measurements of all components of the HERA–B detector verify the observed time structures for the proton interactions. This confirms that we observe real target interactions even inside the bunch gaps. With help of the vertex detector for instance one can additionally demonstrate that the interactions produced by protons from the continuous component (coasting beam region) are shifted with respect to the beam center. This is shown in figure 11.3, where tracks, reconstructed by the HERA–B vertex detector, are represented in the x–y target plane while an inner and an outer wire was in operation. The beam center is also denoted. At that time, the outer wire is located inside the coasting beam region, shown in figure 11.2b). The shift in the y–direction indicates also a vertical dispersion besides the horizontal dispersion at the location of the target wires. The distance to the beam center amounts $\approx 4\sigma$ for the inner wire and $\approx 7\sigma$ for the outer wire.

As a consequence of the outer transverse beam shape, the outer wire has to move through the coasting beam region before reaching bunch correlated interactions. A typical movement evolution for an outer wire is shown in figure 11.4, where the interaction rate and the nominal wire position of the outer II wire is shown as a function of the time. This measurement was performed on January 20th, 1999. After reaching the coasting beam region at $17^{\underline{07}}$ h, the wire needs 18 minutes to reach the bunched beam region at approximately $17^{\underline{25}}$ h. At that time, the bunch correlated interactions appear.

Also the decrease in the movement velocity of the wire at the time the wire approaches the bunched beam region is a significant characteristic for the transition between the two regions described above.

## 11.2 Comparison Between the Amount of Coasting Beam for 820GeV and for 920GeV Protons

Besides noise of the RF–System and inter beam scattering the proton synchrotron radiation contributes to the energy loss of the protons. At the HERA proton storage ring the energy loss amounts 6 eV and 10 eV per turn for 820GeV and 920GeV

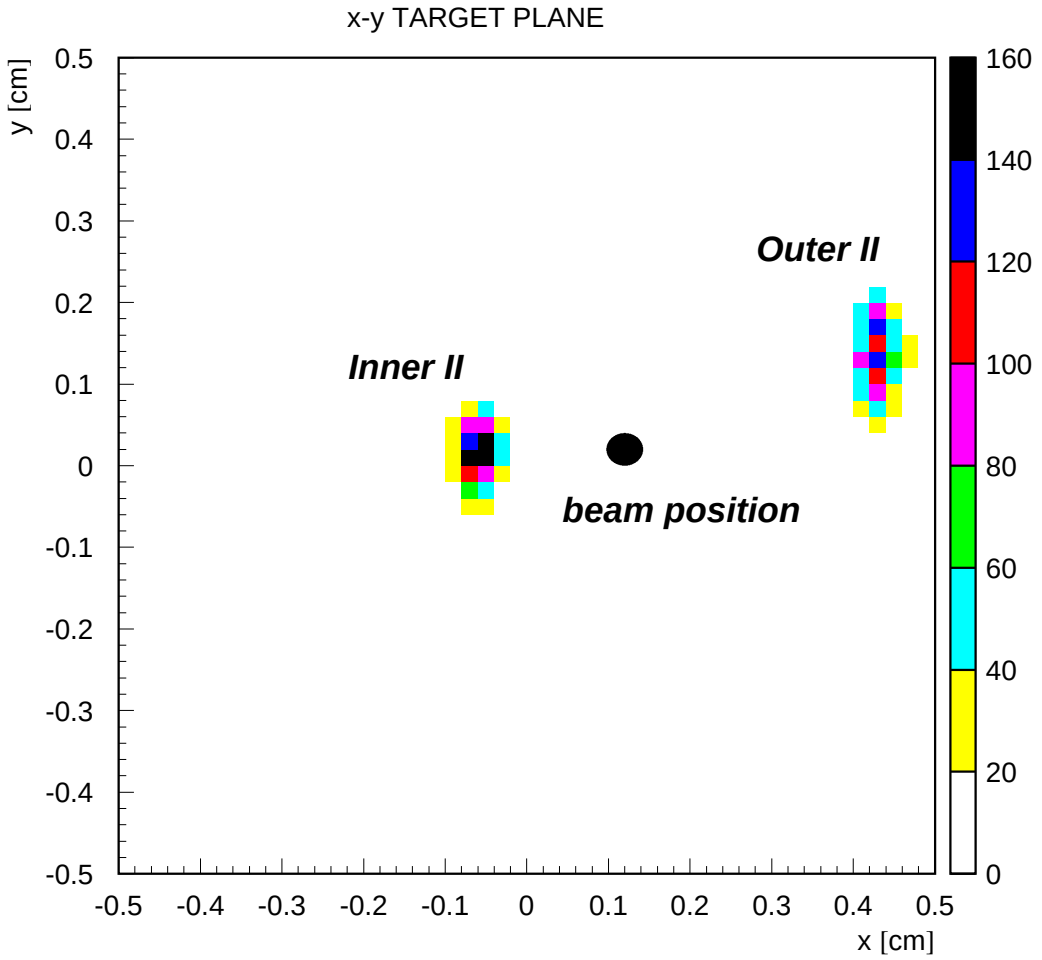


**Figure 11.3**: Target spots for an inner and an outer target wire inside the x–y target plane reconstructed by the HERA–B vertex detector.

respectively [37]. If the energy loss due to proton synchrotron radiation has a significant impact on the production of coasting beam, a correlation between the amount of produced coasting beam and the proton energy should be observed.

The following parameters that parameterize the population of coasting beam within the transverse tails (coasting beam region) are measured to quantify the amount of coasting beam and its spatial distribution as it is observed by the HERA–B target:

- $N_{IA}$ – the integrated number of target interactions, calculated from the interaction rate $R_{IA}$ until the wire reaches the bunched beam region:

$$N_{IA} = \left( \frac{1}{n} \sum_{i=1}^{n} R_{IA}(i) \right) \cdot \triangle t_{cb} = \overline{R}_{IA} \cdot \triangle t_{cb}$$

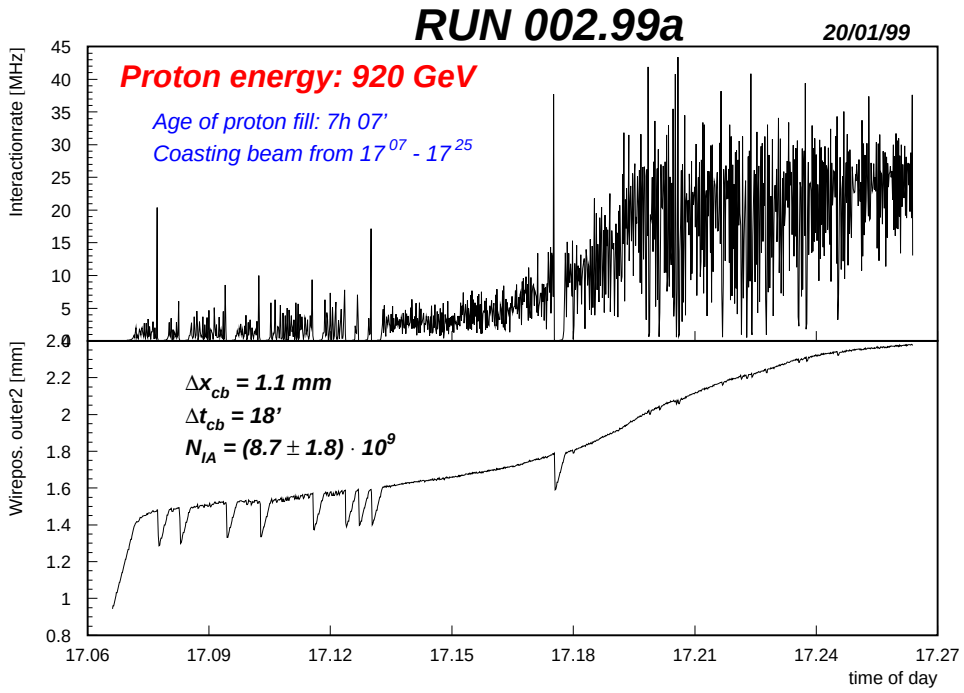


**Figure 11.4**: Interaction rate and nominal wire position for the outer II wire. The wire reaches the coasting beam region at $17^{\underline{07}}$ h and has passed through it at $17^{\underline{25}}$ h. At the beginning the wire is retracted several times by 200$\mu$m automatically by the emergency system due to spikes inside the interaction rate.

Due to the well known fact that collimators at locations with a large horizontal dispersion also scrape the coasting beam, this parameter does not measures the number of produced coasting beam protons directly but is strongly correlated to this number.

- $\triangle x_{cb}$ – the range the outer wire has moved within the coasting beam region. It measures the width of the transverse tails. Note that this parameter in addition depends on aperture limitations like collimator settings for instance.

- $\triangle t_{cb}$ – the time the outer wire needs to move through the coasting beam region until it reaches the bunched beam region.

In order to compare the parameters, two dedicated measurements are chosen at 820GeV in 1997 and 920GeV in 1999. Since $N_{IA}$ increases with time as it is shown in figure 11.7, the age of the proton fill of both runs nearly match and amounts slightly more than 7 hours at the moment of the measurement. The interaction rate and the nominal wire position as a function of time is shown in figure 11.4 for the measurement in 1999. The same measurements for the corresponding run on June 28th, 1997 are plotted in figure 11.5. The parameters listed above are also notified.

The comparison of the characteristic values for $\triangle x_{cb}$ and $\triangle t_{cb}$ leads to a comparable width of the transverse beam tail. Although the values depend on aperture

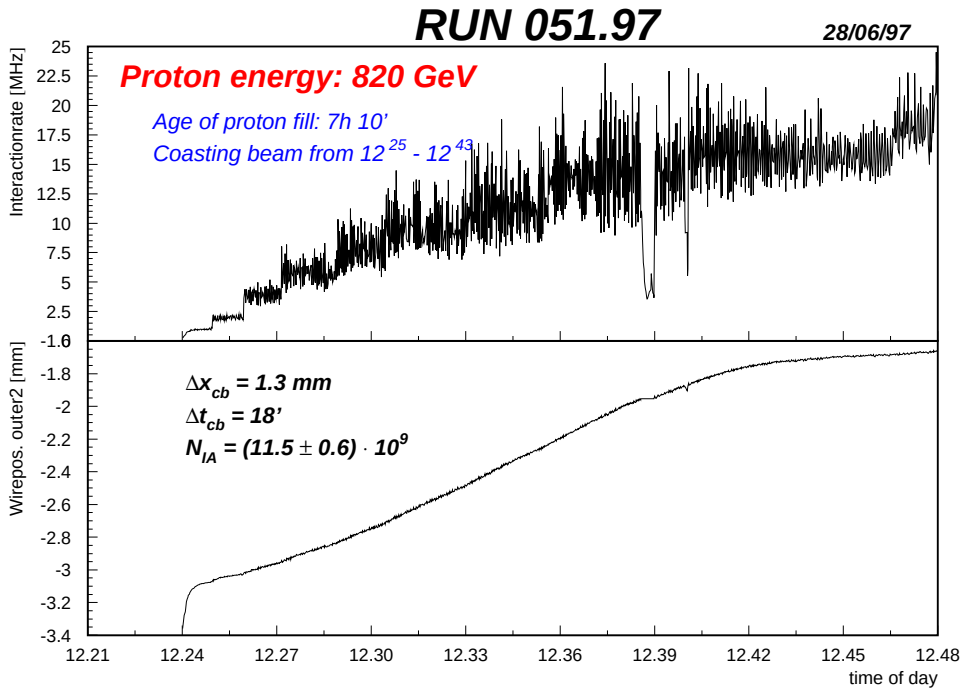


**Figure 11.5**: Interaction rate and nominal outer wire position for a measurement in 1997 with a proton energy of 820GeV. The wire reaches the coasting beam region at $12\underline{25}$ h and reaches the bunched beam region at $12\underline{43}$ h. At that time the wire movement velocity decreases significantly.

limitations, one clearly realizes that the wire has to scrape in the order of 1mm in both cases until the bunch correlated interactions appear. Moreover the transverse tails are populated with coasting beam significantly for both measurements. In contrast to the expectation, the tails seem to be more populated for the 820GeV protons. This result is verified by figure 11.7 where $N_{IA}$ is shown as a function of the age of the proton fill for different measurements at 820 and 920GeV protons. The amount of coasting beam characterized by $N_{IA}$ is at least not smaller for 820GeV protons than for 920GeV protons. This follows especially from the cluster of data points at an age of approximately 5 hours.

The interaction rate and the nominal wire positions of the measurement at 820GeV that took place on May 1st, 1999 during machine studies are shown in figure 11.6a) and b) respectively. $N_{IA}$ that is also notified and included in figure 11.7 is in a good agreement with the results at 820GeV collected in 1997. In consideration of some uncertainties due the impact of aperture limitations, no significant difference between the population of coasting beam within the transverse tails at different proton energies is found.

As described in section 1, the interaction rate adds from a bunch rate $R_{BX}$ that is calculated from bunch correlated interactions and a coasting beam rate $R_{CB}$, considering the interactions between filled bunches:

$$R_{IA} = R_{BX} + R_{CB}.$$

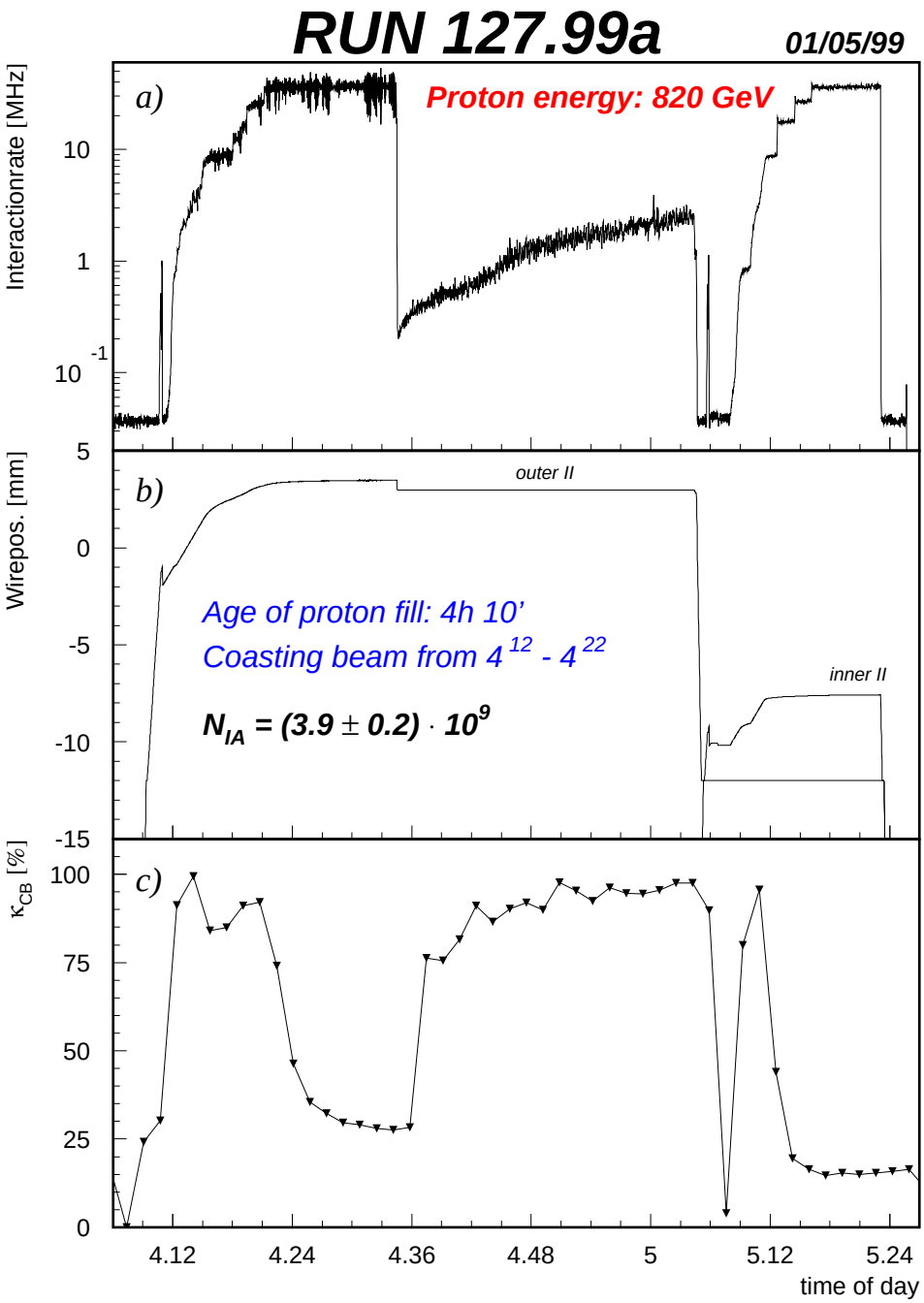


**Figure 11.6**: a) Interaction rate, b) nominal wire positions and c) $\kappa_{CB}$ for the 820GeV run during machine studies. The outer wire is moved first, followed by the inner one at $5\underline{05}$ h. For the inner wire one observes a contribution of coasting beam to the interaction rate of about 15%.

Therefore the relative contribution of the coasting beam rate to the interaction rate $\kappa_{CB} = \frac{R_{CB}}{RIA}$ is correlated with the existing amount of coasting beam inside the HERA

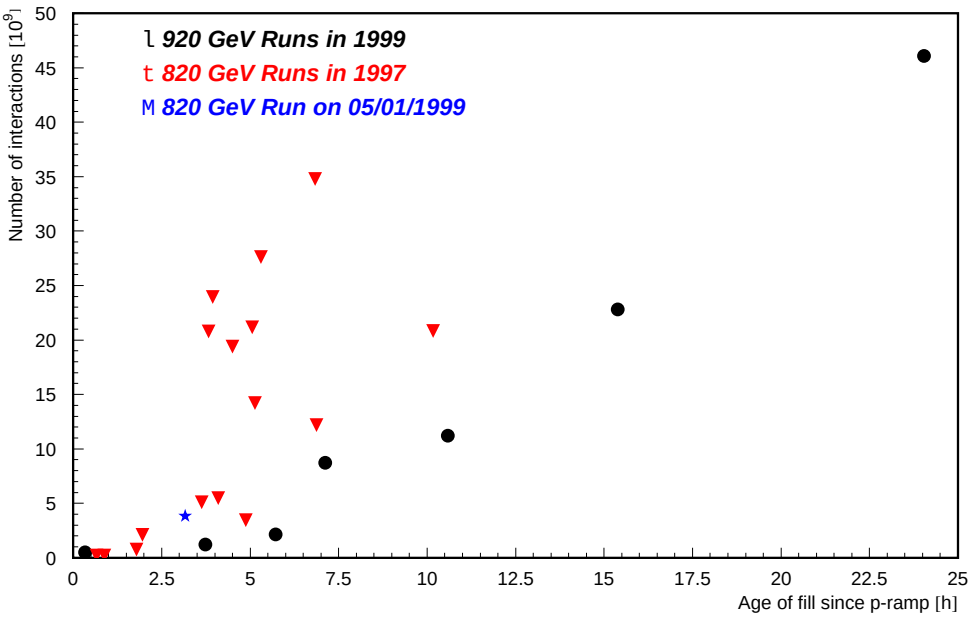


**Figure 11.7**: Total number of interactions within the coasting beam region as a function of the age of a proton fill for different measurements in 1999 and 1997. The dependence on the age of the proton fill is clearly visible. A difference between the values could be realized for 820GeV and 920GeV protons, especially at 5 hours. The value for the measurement on 1st of may, 1999 fits completely into the data from 1997.

proton storage ring. Figure 11.8 shows the three different rates for a measurement on March 17th, 1999 when an *inner* wire was moved first to an interaction rate of 1 and 10 MHz, followed by an *outer* wire. For a better understanding, the time structure of the interactions, resulting from the FADC data, is also shown for the two different target wires. At that time the target interactions are produced by the outer wire the interaction rate of nearly 10 MHz is completely dominated by the coasting beam rate, whereas the coasting beam rate for the inner wire contributes about 10%.

To get an overview about the share of coasting beam rate in the interaction rate, $R_{CB}$ was calculated for run periods at which a stable and constant interaction rate of 10 MHz was established. In table 11.1 the mean ratio $\kappa_{CB} = \frac{R_{CB}}{R_{IA}}$ out of a set of measurements is presented for each wire orientation. The resulting RMS value is added as the statistical error.

First of all it strikes that the values for $\kappa_{CB}$ is different for different wires, both for 820GeV protons and 920GeV protons. Due to the horizontal dispersion at the location of the target wires $\kappa_{CB}$ is largest for the outer wires and smallest for the inner ones. The different values for the above and below wires imply an existing vertical dispersion. This result is verified by the measurements of the HERA–B vertex detector displayed in figure 11.3 that shows a cluster of interactions shifted to the outer and upper direction. These interactions are exclusively caused by the coasting beam protons and this already indicates a higher coasting beam rate in this

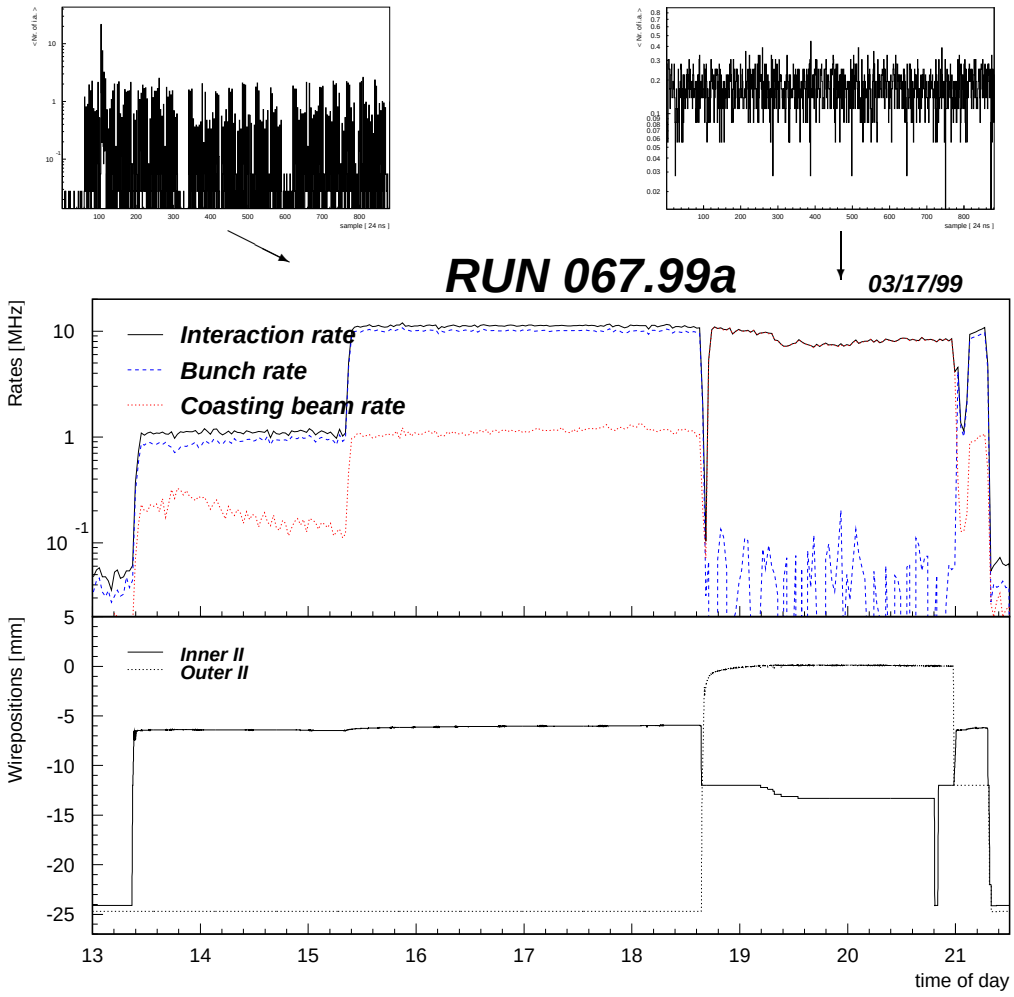


**Figure 11.8**: Interaction rate, bunch rate and coasting beam rate depending on the time of day for a dedicated run in 1999. Additionally the time structures for two different dates and wires are plotted. The amount of coasting beam is ≈10% for the inner wire, while the interaction rate caused by the outer wire is totally dominated by coasting beam protons.

direction.

Furthermore the ratio of coasting beam rate to interaction rate increases significantly from 1997 to 1998. Therefore it seems that the amount of coasting beam increases if the proton energy changes. In contrast, the measurement of $\kappa_{CB}$ for the 820GeV run during machine studies gives a value of

$$\kappa_{CB} = (15 \pm 6)\% \quad ,$$

as it is shown in figure 11.6c) for 15:15<t<15:24. The large uncertainty results from

the small amount of statistics, because this measurement was carried out only for a couple of minutes at the end of the run. Our measurement on 1st of May, 1999 during machine studies indicates that the increase of the contribution of coasting beam to the interaction rate is not caused by the change of the proton energy, because the value for $\kappa_{CB}$ does not correspond with the values from 1997.

| Wires | $\overline{\kappa}_{CB}$ (1997) | $\overline{\kappa}_{CB}$ (1998) | $\overline{\kappa}_{CB}$ (1999A) |
|---|---|---|---|
| above | $(16.3 \pm 2.2)\%$ | $(18.8 \pm 2.5)\%$ | $(24.8 \pm 2.9)\%$ |
| below | $(4.6 \pm 1.0)\%$ | $(14.2 \pm 1.5)\%$ | $(13.5 \pm 1.7)\%$ |
| inner | $(1.5 \pm 0.2)\%$ | $(8.1 \pm 0.4)\%$ | $(8.4 \pm 0.6)\%$ |
| outer | $> 20\%$ | $> 35\%$ | $> 35\%$ |
| | 820GeV | 920GeV | 920GeV |

**Table 11.1**: The mean share of coasting beam rate in the interaction rate for the different target wire orientations. The given value was averaged over measurements for time periods, the interaction rate amounted 10 MHz.

## 11.3 Conclusions

The FADC system of the rate measurement setup of the HERA–B target group allows to identify two different regions of the outer transverse beam tail at the location of the HERA–B target. The *coasting beam region* is observed for distances between the outer wire and the beam center which are $>\approx 6\sigma$. Within this region the target interactions are not correlated with proton bunches. For distances between the wire and the beam's center which are $<\approx 6\sigma$, a *bunched beam region* has been observed. Within this region bunch correlated interactions appear but they are superimposed by a continuous background of interactions caused by coasting beam protons.

The amount of coasting beam can be quantified by different parameters for the two regions: (1) The total number of target interactions $N_{CB}$ which are observed while the coasting beam is scraped off until bunch correlated interactions appear is a measure of the coasting beam protons in the transverse beam tail. (2) The parameter $\kappa_{CB}$ that gives the share of coasting beam in the interaction rate can characterize the amount of coasting beam within the bunched beam region.

The results for protons with energies of 820GeV and 920GeV were presented. It was shown that the population of the outer transverse tails with coasting beam protons seems to be slightly higher for protons with an energy of 820GeV than for protons with 920GeV. A significant impact of proton synchrotron radiation is not observable. Some uncertainties still exist due to the impact of aperture limitations like collimators.

The contribution of coasting beam rate to the interaction rate is quantified by $\kappa_{CB}$ measured at a constant interaction rate of 10 MHz. This parameter increases significantly between 1997 and 1998. However, the measurement of $\kappa_{CB}$ at the 820GeV run in 1999 during machine shifts does not coincide with the results for

the runs in 1997 at 820GeV. In consideration of this measurement even for the bunched beam region no clear indication for the proton synchrotron radiation to have a significant impact on the production of coasting beam is observed.

# 12 Coasting Beam Studies

by Ch. Montag, DESY Hamburg

Date: 1999, May 1, 1am–5am, Logbook XXXVII, p. 74 (820GeV studies)
Date: 1999, May 1 , 3pm–5pm , Logbook XXXVII, p. 77 (Increased emittance)
Date: 1999, July 9 , 2am–4am , Logbook XXXVII, p. 213–214 (Collimators)
Date: 1999, July 10, 1am–7am , Logbook XXXVII, p. 223 (208MHz RF only)
Date: 1999, July 19, 2pm–4pm , Logbook XXXVII, p. 280–282 (Kicking)
Date: 1999, July 20, 10am–1pm, Logbook XXXVII, p. 288–289 (Kicking)

Since several years HERA–B has suffered from a coasting beam contribution in the proton beam and in summer 1998 it has additionally been realized that background spikes in the HERA collider experiments ZEUS and H1 are correlated to this coasting beam. Therefore some investigations to determine the debunching mechanism as well as to remove the unbunched protons were carried out (see also [39]). This report shows the present status of these studies.

## 12.1 Some Facts

Until 1997 unbunched protons were observed by HERA-B only. Therefore there was some suspicion that the coasting beam is produced by the interaction of protons with the HERA-B wire target, where the protons lose a certain amount of energy. These energy losses add up and finally exceed the RF acceptance, thus leading to a debunched beam contribution.

Since unbunched protons were almost exclusively observed with the outer target wire, together with the negative dispersion at the HERA-B target this means that the momentum deviation of the coasting beam is negative, $\Delta p/p < 0$.

## 12.2 Measurement of the Coasting Beam Contribution

The coasting beam contribution in the HERA proton beam is measured using the difference of the total current and the bunch current,

$$I_{\text{coasting beam}} = I_{\text{total}} - I_{\text{bunched}} \ . \tag{12.1}$$

The total current $I_{\text{total}}$ is determined using a DCCT, while the bunched current is measured by integrating the current only over a time range of $\pm$15nsec around the nominal bunch center positions [38].

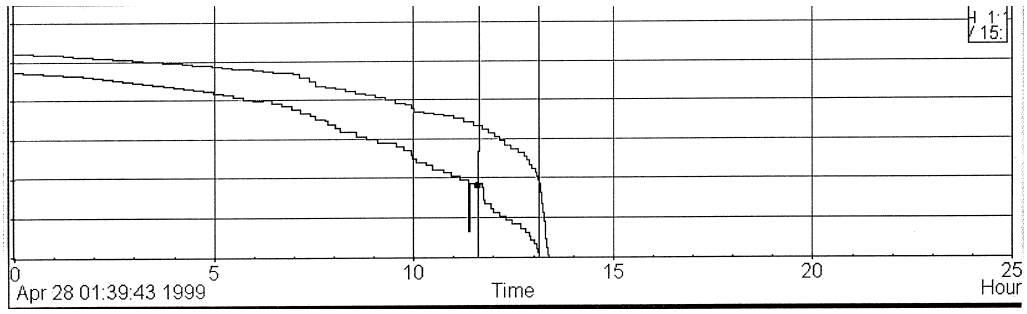


**Figure 12.1**: Total proton current (upper curve) and bunched current (lower curve) during moving-in a HERA-B target wire.

## 12.3 Possible Production Mechanisms of Coasting Beam

### 12.3.1 Energy Loss at the HERA-B Wire Target

As already mentioned, the energy loss of the protons at the HERA-B wire target can produce coasting beam when this energy loss is larger than the distance to the separatrix. Therefore the coasting beam contribution was measured while a target wire was moved towards the beam. As figure 12.1 shows, the bunched current drops by about 0.4mA at 11:30, while the total current remains constant. This shows that in some cases the wire target indeed contributes to the production of coasting beam. On the other hand, the coasting beam also occurs when the HERA-b wire target is not used.

### 12.3.2 Coasting Beam at 820GeV

Until 1997 coasting beam was mainly observed at HERA-B. Therefore one might expect that the proton energy increase from 820 to 920GeV has an influence on the effect of the coasting beam in the experiments H1 and ZEUS. During the machine studies in May 1999 the direct measurement of the coasting beam contribution described above was used to determine coasting beam production at 820GeV. Figure 12.2 shows the development of coasting beam at 820GeV during approximately 4 hours after the ramp. During this time the coasting beam increased by about 250$\mu$A, which does not significantly differ from observations at 920GeV. In addition the HERA-B outer target wire was moved towards the beam in order to confirm this observation by scraping off the coasting beam. This measurement also did not show any significant qualitative difference compared to the situation at 920GeV [40]. A more detailed description of the differences between coasting beam at 820GeV and 920GeV can be found in section 11.

### 12.3.3 Effect of the Collimators

Since there was some suspicion that coasting beam might be produced by energy loss at a rough surface of some collimator jaws, the influence of various jaws on

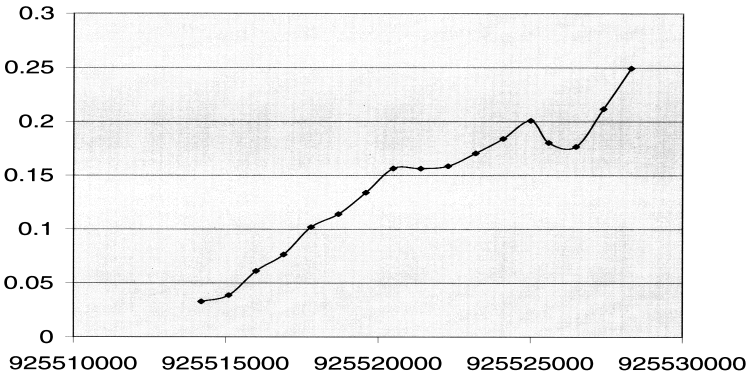


**Figure 12.2**: Coasting beam contribution at 820GeV during about 4 hours after ramp on May 1, 1:00 to 5:20. The dip near the end is caused by the HERA-B wire scraping away the coasting beam.

the coasting beam production rate was studied. During these measurements, various jaws were moved to the beam, but no significant change in the coasting beam production rate, compared with the situation with open collimators, was found.

### 12.3.4 Coasting Beam with one RF System Only

Due to technical problems with the 208MHz RF system, there was a single run with the 52MHz system only. In this case the beam was injected with the 208MHz system switched on and the bunch rotation in PETRA switched off. After injection the 208MHz RF system was switched off and the beam was ramped to 920GeV. During about 7.5 hours, the coasting beam increased to about 16mA, which shows that coasting beam is also produced without the 208MHz system. Therefore this system alone cannot be responsible for coasting beam production. This measurement should be repeated under better defined conditions.

### 12.3.5 Coasting Beam at Increased Transverse Emittance

One possible production mechanism for coasting beam is intra-beam scattering, leading to momentum deviations exceeding the RF acceptance. Since the growth rates due to this process depend on the six-dimensional phase space volume of the bunches, increased transverse emittances should lead to a smaller growth rate in the longitudinal phase space. Therefore, the coasting beam production rate should also be significantly smaller. In order to study this effect, the transverse emittance of the stored proton beam was increased by a factor of about 2.5 at 150 GeV. After ramping this beam, no coasting beam was measured after 1.5 hours, which might indicate that intra-beam scattering is a possible source for coasting beam.

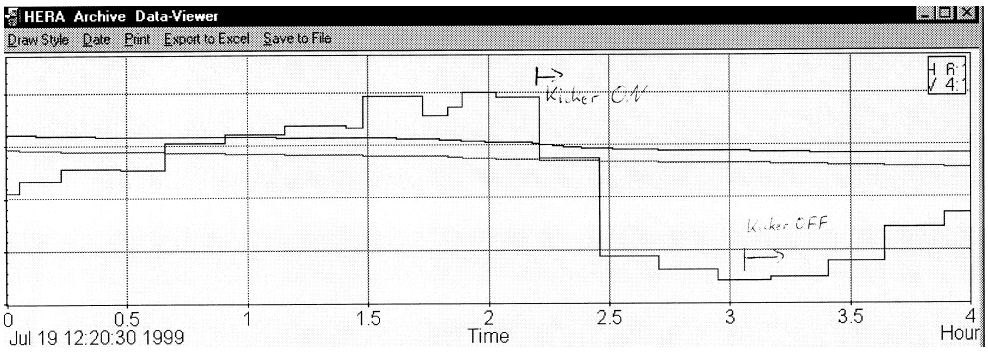


**Figure 12.3**: Total proton current (upper line), bunch current (middle) and coasting beam contribution (lower line) vs. time during kicking.

## 12.4 Removing the Coasting Beam by Resonant Kicks

In case the production mechanism of the coasting beam cannot be found and finally eliminated, some method to remove the coasting beam must be developed. A possibility is to use the transverse feedback kickers to remove the coasting beam in the dump kicker gap. Since these kickers are rather weak, this has to be done resonantly, with the kicker frequency being the betatron frequency of the coasting beam. During previous studies in 1998 it was observed that the impedance mismatch between power amplifier and kicker, and the resulting reflection of the signal, leads to an excitation of several bunches in the first train of ten bunches behind the dump kicker gap. Since the kicker signal is modulated at 10.4MHz, this effect could be minimized by adding about 1.5m of cable between amplifier and kicker, thus shifting the reflected signal in such a way that it hits the bunches just when it is approximately zero. Additionally, the kicker frequency sweep was chosen such that it does not cover the betatron frequencies ($f_{\mathrm{hor}} = 13.8\mathrm{kHz}$, $f_{\mathrm{vert}} = 14.1\mathrm{kHz}$) of the bunched beam. Since the relative momentum deviation $\Delta p/p$ of the coasting beam is negative while the chromaticities are positive, the betatron frequencies of the coasting beam are below these values.

In July this improved system was tested. With a kicker frequency sweeping from 13.2 to 13.5kHz and a sweeping period of 500msec, applied over 4 of the 15 bunch positions in the dump kicker gap, the coasting beam contribution was reduced by about 500$\mu$A after some 30 minutes of kicking, which can be seen in figure 12.3. During this time, no effect on the bunched beam was observed. It turned out that the success of this method is quite sensitive to the correct tune values.

# 13 Hera-p Tail Shaping Using Dipole Kicks

by Ch. Montag, DESY Hamburg

Date: 1999, Apr. 29, 8am–6pm, Logbook XXXVII, p. 53–64

In December 1998 and April 1999 the feasibility of increasing the particle density in the transverse tails of the HERA proton beam by application of dipole kicks was investigated (see also [39]).

After accelerating 180 bunches to 920GeV, a target wire was moved into the beam halo until a rate of 10 or, respectively, 40MHz was reached. After stopping the wire movement, the beam was excited at the third harmonic of its horizontal betatron frequency using the horizontal feedback kickers. Since the betatron frequency of the protons is amplitude dependent [41], a narrow band noise of ±50Hz around the center frequency was used. Figure 13.1 shows the resulting interaction rate at the HERA-B wire target with and without this excitation. Additionally the

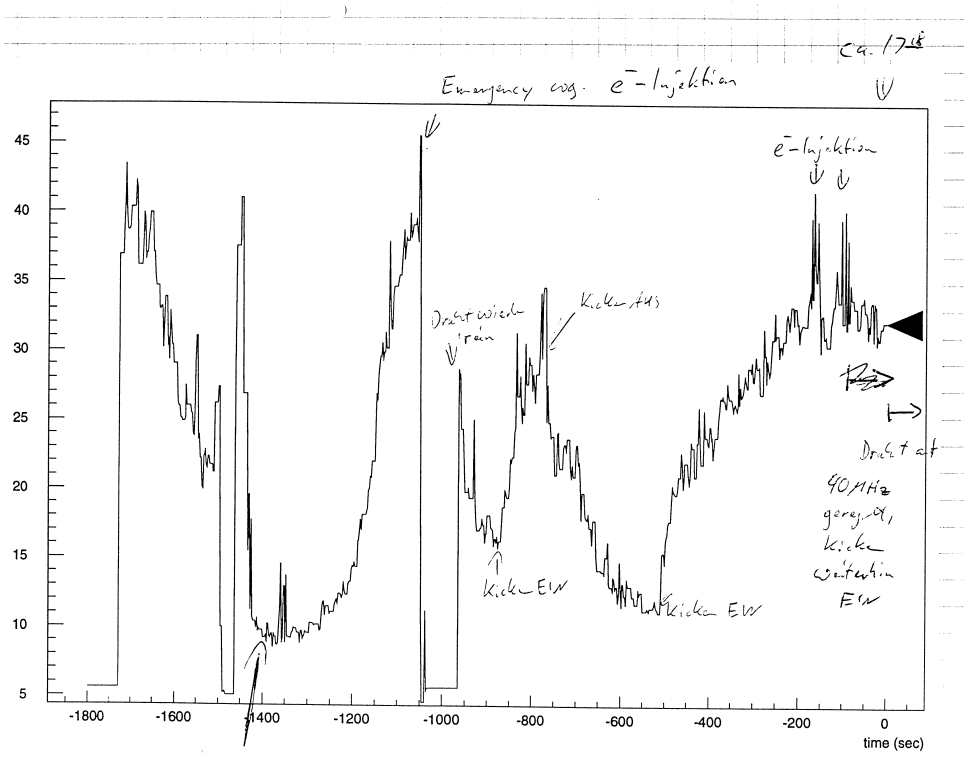


**Figure 13.1**: Interaction rate at the HERA-B wire target with a noise excitation of ±50Hz around the third harmonic of the betatron frequency. The kicker was switched on at −1400sec and −870sec off at −750sec and on again at −500sec.

motion of the target wire with position control switched on and a nominal rate of

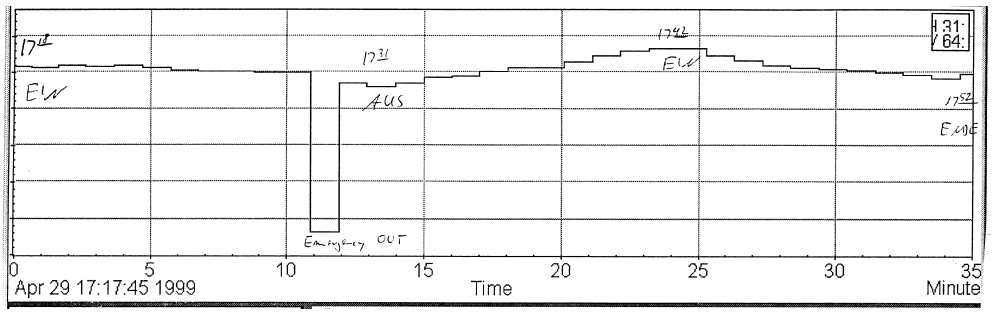


**Figure 13.2**: Target position at constant interaction rate of 40MHz at the HERA-B wire target, with and without noise excitation. Without excitation (from minute 12 to 24 according to the horizontal axis), the wire slowly moves towards the beam center by about 50$\mu$m. When the excitation is switched on (at minute 24), the wire moves back by the same amount.

40MHz was observed as shown in figure 13.2. Without excitation, the wire moves slowly towards the beam center in order to keep the interaction rate constant. With the excitation kicker switched on, the wire retracts from the beam. This latter observation indicates that the excitation amplitudes used during this experiment were larger than required.

Before and after these studies, the proton beam emittance was measured using the wire scanners. According to these measurements the emittance increased by roughly 20% during about 1.5 hours of excitation. This is a relevant increase, since the statistical error appear to be less than 20%, although there has not been a detailed analysis of the errors of the wire scanner. Concerning the impact on the luminosity at the colliding beam experiments ZEUS and H1, this emittance growth is certainly not tolerable. However, this method might be applicable at smaller kick amplitudes in connection with the wire position feedback, thus probably leading to an interaction rate stabilization. Alternatively, it is also planned to study the effect of tune modulation [42] on the interaction rate stability.

# 14 Stabilization of HERA–B Interaction Rates Using Tune Modulation

by Ch. Montag, DESY Hamburg and K. Ehret, University of Dortmund
and S. Issever, University of Dortmund

Date: 1999, Dec. 14, 10pm to Dec. 15, 7am, Logbook XXXXI, p. 36–42
Date: 1999, Dec. 18, 1am to Dec. 18, 5am, Logbook XXXXI, p. 60–67

During the machine study period in December 1999, the feasibility of stabilizing the interaction rate of stored protons at the internal HERA–B wire target by means of tune modulation was studied. Although the collimators were placed at about 4 to 5$\sigma$ it could nevertheless be shown that tune modulation leads to an increased interaction rate stability, while the luminosity at the colliding beam experiments ZEUS and H1 is not affected.

## 14.1 Introduction

The HERA–B experiment [43] uses an internal wire target inserted into the halo of the stored HERA proton beam. While machine performance was improved during recent years, this halo practically vanished. Therefore the wire target has to be moved close to the beam core at about 3 to 4 $\sigma$ in order to keep the actual rate constant at the design rate of five interactions per bunch crossing. As it was observed, this leads to a high sensitivity of the interaction rate to beam orbit jitter of very small amplitudes. To overcome this situation, it has been suggested to artificially create some beam halo by means of tune modulation [42]. This was expected to have the advantage of not affecting the beam core, thus leaving the luminosity at the colliding beam experiments ZEUS and H1 constant. During the machine study period in December 1999, the feasibility of improving the interaction rate stability at HERA–B by means of tune modulation has been tested experimentally.

To study the horizontal phase space structure under the influence of tune modulation, a model accelerator consisting of two linear maps and two interaction points has been used. The horizontal and vertical tunes of the accelerator are given by the sum of the phase advances due to the linear maps and due to the beam-beam tune shift. A tune modulation is simulated by a harmonic modulation of the phase advances of the linear maps. The horizontal beam–beam kick for $\sigma_{z,e} < \sigma_{x,e}$ is in good approximation calculated as [44]

$$\begin{aligned}\Delta x' &= C \cdot \Im \left[ W\left(\frac{x+iz}{(2(\sigma_{x,e}^2-\sigma_{z,e}^2))^{1/2}}\right)\right. \\ &\left. - \exp\left(-\frac{x^2}{2\sigma_{x,e}^2}-\frac{z^2}{2\sigma_{z,e}^2}\right)\cdot W\left(\frac{x\frac{\sigma_{z,e}}{\sigma_{x,e}}+iz\frac{\sigma_{x,e}}{\sigma_{z,e}}}{(2(\sigma_{x,e}^2-\sigma_{z,e}^2))^{1/2}}\right)\right], \quad (14.1)\end{aligned}$$

| | | |
|---|---|---|
| proton gamma factor | $\gamma_p$ | 983 |
| number of positrons per bunch | $N_b$ | $1.4 \cdot 10^{10}$ |
| hor. tune | $Q_x$ | .298 |
| hor. $\beta$-function at IP | $\beta_x^*$ | 7.0m |
| classical proton radius | $r_p$ | $1.54 \cdot 10^{-18}$m |
| hor. positron beam size | $\sigma_{x,e}$ | $200\mu$m |
| vert. positron beam size | $\sigma_{z,e}$ | $54\mu$m |
| hor. proton beam size | $\sigma_{x,p}$ | $200\mu$m |
| vert. proton beam size | $\sigma_{z,p}$ | $54\mu$m |

**Table 14.1**: Parameters used for the simulation of the tune modulation effect (figure 14.1).

with

$$C = -\frac{2\pi\Delta Q_x \sigma_{x,e}(\sigma_{x,e}+\sigma_{z,e})}{\beta_{x,p}^*} \cdot \left(\frac{2\pi}{\sigma_{x,e}^2-\sigma_{z,e}^2}\right)^{1/2}, \tag{14.2}$$

$$\Delta Q_x = \frac{\beta_{x,p}^* r_p N_b}{2\pi\gamma_p(\sigma_{x,e}+\sigma_{z,e})\sigma_{x,e}}, \tag{14.3}$$

$$W(x+iz) = \frac{a}{1-ip(x+iz)} + \frac{b}{(1-ip(x+iz))^2} + \frac{c}{(1-ip(x+iz))^3}, \tag{14.4}$$

$$\begin{aligned} x,\, z &> 0, \\ a &= 0.34802, \\ b &= -0.09588, \\ c &= 0.74786, \\ p &= 0.47047, \end{aligned}$$

and

$$\begin{aligned} \Delta x'(-x,z) = \Delta x'(-x,-z) = -\Delta x'(x,z), \\ \Delta z'(x,-z) = \Delta z'(-x,-z) = -\Delta z'(x,z). \end{aligned}$$

For the simulations the parameters given in table 14.1 are used. To illustrate the effect of tune modulation, figure 14.1 shows the horizontal phase space without tune modulation (top) and with tune modulation (bottom). Note that in contrast to the value given in table 14.1 the number of positrons per bunch has been increased to $2 \cdot 10^{12}$ to enlarge the effect on the proton motion.

## 14.2 Experimental Set–up

The tune modulation signal is provided by a PC with a DATEL PC420 wave generator board that can be controlled remotely from the HERA control room. This signal is fed into the chopper power supplies of the QP40 and QP42 quadrupoles in HERA West. QP40 is usually used to control the horizontal tune $Q_x$, and QP42

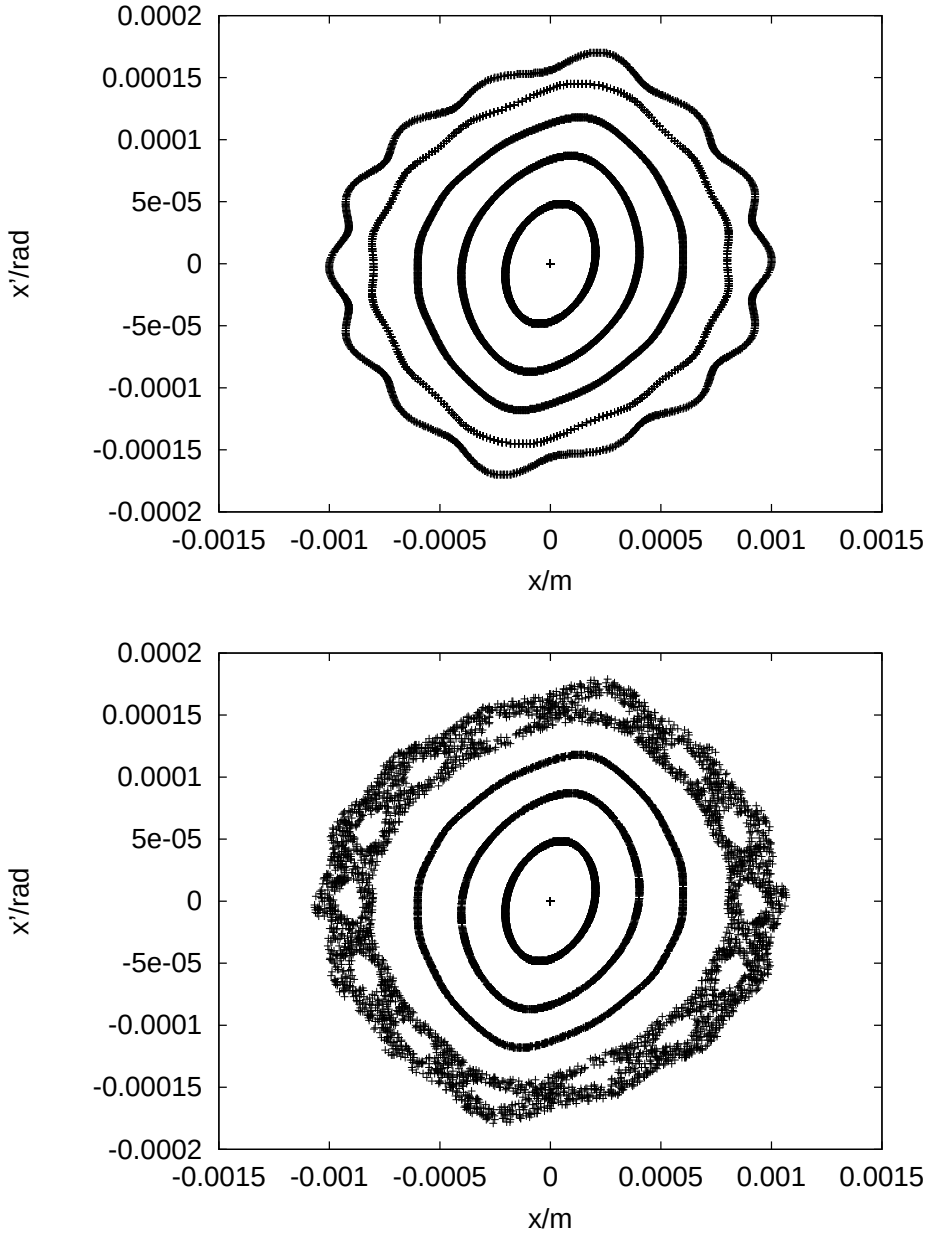


**Figure 14.1**: Horizontal phase space of the model accelerator without (top) and with (bottom) tune modulation. As an example, a tune modulation with two "frequencies" of $(250\text{turns})^{-1}$ and $(1000\text{turns})^{-1}$ and a modulation depth of $\Delta Q_x = 5{\cdot}10^{-4}$ has been chosen here. Together with the HERA revolution frequency of roughly 50kHz these "frequencies" correspond to 50Hz and 200Hz, respectively. The positron bunch population is $N_b = 2 \cdot 10^{12}$, which corresponds to 50 times the HERA–e design current.

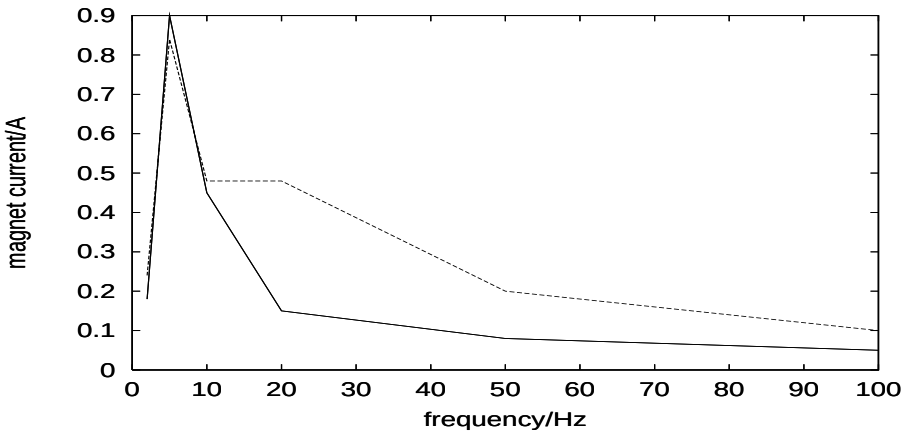


**Figure 14.2**: Measured AC magnet current as a function of frequency for an input voltage of 1V and two DC magnet currents of 30A (lower) and 60A (upper curve), respectively [45].

for the control of $Q_z$. Due to the large inductance of the quadrupole magnets, high frequency signals are effectively suppressed, while low frequencies of a few Hz are suppressed by internal feedback loops of the power supplies. Figure 14.2 shows the AC magnet current (peak value) as a function of the modulation frequency for 1V modulation amplitude of the power supply input signal and DC currents of 30A and 60A, respectively. In both planes a magnet current of 1A corresponds to a tune change $\Delta Q$ of about $5 \cdot 10^{-3}$. For the tune modulation experiments 180 proton bunches with a total current of 75mA and 189 positron bunches of a total current of about 20mA were filled, and the beams were brought into collision at Zeus and H1. To protect the high energy physics detectors, the collimators had to be closed using the automatic "to–beam–procedure" with a limiting collimator rate of 1000Hz for all jaws. The resulting collimator setting is given in table 14.2, together with the one sigma beam sizes at the various jaws, assuming an emittance of $5 \cdot 10^{-9}$m in both planes. The proton tunes were set to the nominal values of $Q_x = .298$ and $Q_z = .292$, respectively.

## 14.3 Measurements

Two kinds of experiments were performed for different tune modulation settings. To proof the diffusion enhancement in the beam tails, a single target wire (Inner I) was first moved towards the beam until an interaction rate of 10MHz without tune modulation was reached. After several minutes this wire was retracted by 100$\mu$m and fixed at that position, resulting in a reduced interaction rate of about 200kHz. When the tune modulation with up to two frequencies was switched on, the interaction rate increased immediately and decreased to a stable level after a few minutes (see figure 14.3). Table 14.3 shows the achieved stable interaction rates

| jaw | position/mm | $\sigma$/mm | half aperture/$\sigma$ |
|---|---|---|---|
| WR94 Outer | $-11.11$ | 0.815 | |
| WR94 Below | $-3.70$ | 0.640 | |
| WR33 Below | $-2.72$ | 0.513 | |
| WL19 Inner | 0.85 | 0.554 | 5.2 |
| WL19 Outer | $-4.92$ | 0.554 | 5.2 |
| WR105 Above | 0.34 | 0.724 | 5.1 |
| WR105 Below | $-7.10$ | 0.724 | 5.1 |
| WR150 Inner | $-6.58$ | 0.426 | 8.1 |
| WR150 Outer | 0.34 | 0.426 | 8.1 |
| WR150 Above | $-3.05$ | 0.636 | 4.1 |
| WR150 Below | $-2.18$ | 0.636 | 4.1 |

**Table 14.2**: Collimator setting during the tune modulation experiment on Dec. 18, 1999. The last column shows the free half aperture in case two opposing jaws were used. To calculate the free aperture, a proton beam emittance of $\epsilon = 20\pi$mm mrad was used. The collimator settings on December 14th/15th were practically the same.

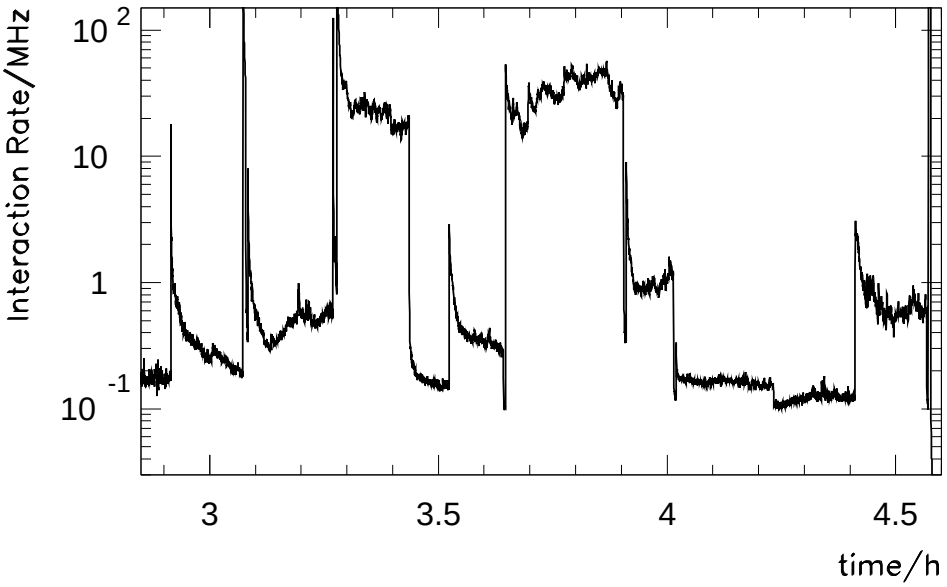


**Figure 14.3**: Interaction rate at the fixed target wire for different tune modulation settings, as given in table 14.3.

| time/h | $f_1$/Hz | $U_1$/V | $f_2$/Hz | $U_2$/V | rate/MHz |
|---|---|---|---|---|---|
| 2.8 | 0 | 0 | 0 | 0 | $0.18 \pm 0.03$ |
| 2.92 | 40 | 2.5 | 190 | 2.5 | $0.27 \pm 0.03$ |
| 3.08 | 20 | 2.5 | 190 | 2.5 | $0.35 \pm 0.04$ |
| 3.27 | 10 | 2.5 | 190 | 2.5 | $23 \pm 5$ |
| 3.4 | 0 | 0 | 0 | 0 | $0.16 \pm 0.02$ |
| 3.52 | 10 | 2.5 | 0 | 0 | $0.35 \pm 0.05$ |
| 3.65 | 10 | 2.5 | 190 | 2.5 | $30 \pm 0.8$ |
| 3.9 | 10 | 1.875 | 190 | 1.875 | $0.9 \pm 0.15$ |
| 4.02 | 10 | 1.25 | 190 | 1.25 | $0.17 \pm 0.02$ |
| 4.23 | 10 | 0.625 | 190 | 0.625 | $0.12 \pm 0.015$ |
| 4.42 | 10 | 2.5 | 0 | 0 | $0.6 \pm 0.1$ |

**Table 14.3**: Tune modulation parameters used during the experiments on Dec. 15th, and measured stable interaction rates at the HERA–B target (see figure 14.3).

together with the tune modulation frequencies and amplitudes, with

$$U(t) = \sum_i U_i \sin(2\pi f_i) \tag{14.5}$$

being the power supply AC input signal that translates into AC magnet current according to figure 14.2. For a fixed target wire, figure 14.4 shows the interaction rates, after they have stabilized, as a function of the total quadrupole magnet current for different modulation frequency settings. In a second step the effect of tune modulation on interaction rate stability at the internal HERA–B wire target was measured. For this purpose the wire position feedback was switched on, thus keeping the mean interaction rate constant at 10MHz and, later, at 40MHz. Since the target wire Inner I was destroyed during the previous experiment, Inner II was used instead. The resulting interaction rate fluctuation was measured for different settings of the tune modulation. Figure 14.5 shows the interaction rate stability with and without tune modulation. As it can be easily recognized, tune modulation does indeed lead to an increased interaction rate stability. This can be explained by the fact that the real positron bunch population during the experiments was smaller by about two orders of magnitude compared to the number used for the phase space plots shown in figure 14.1. Figure 14.6 shows the horizontal phase space for a positron bunch population of $N_b = 1.4 \cdot 10^{10}$ and tune modulation parameters which had been used during one of the experiments (last row of table 14.3). Since the revolution frequency of HERA is roughly 50kHz, a tune modulation frequency of 10Hz corresponds to 1/5000turns in this simulation, while 200Hz correspond to 1/250turns. While the top graph shows the horizontal phase space without tune modulation, the middle

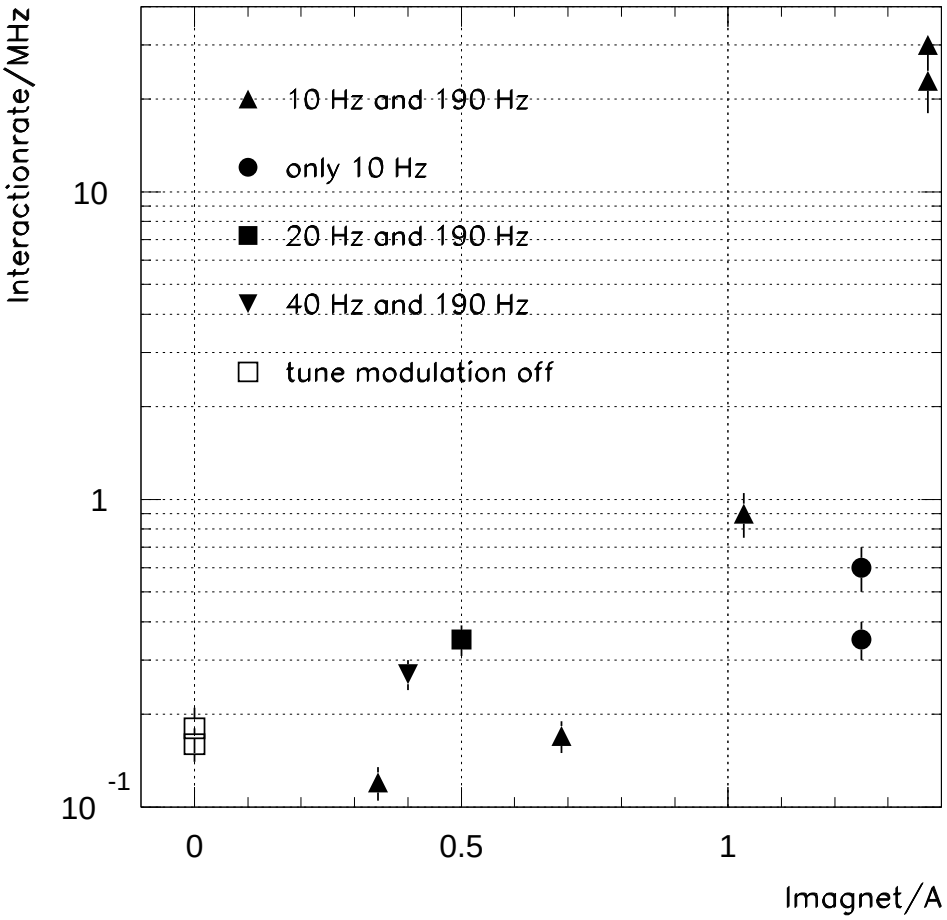


**Figure 14.4**: Interaction rate at the fixed target wire as a function of the total quadrupole magnet current, for different modulation frequency settings.

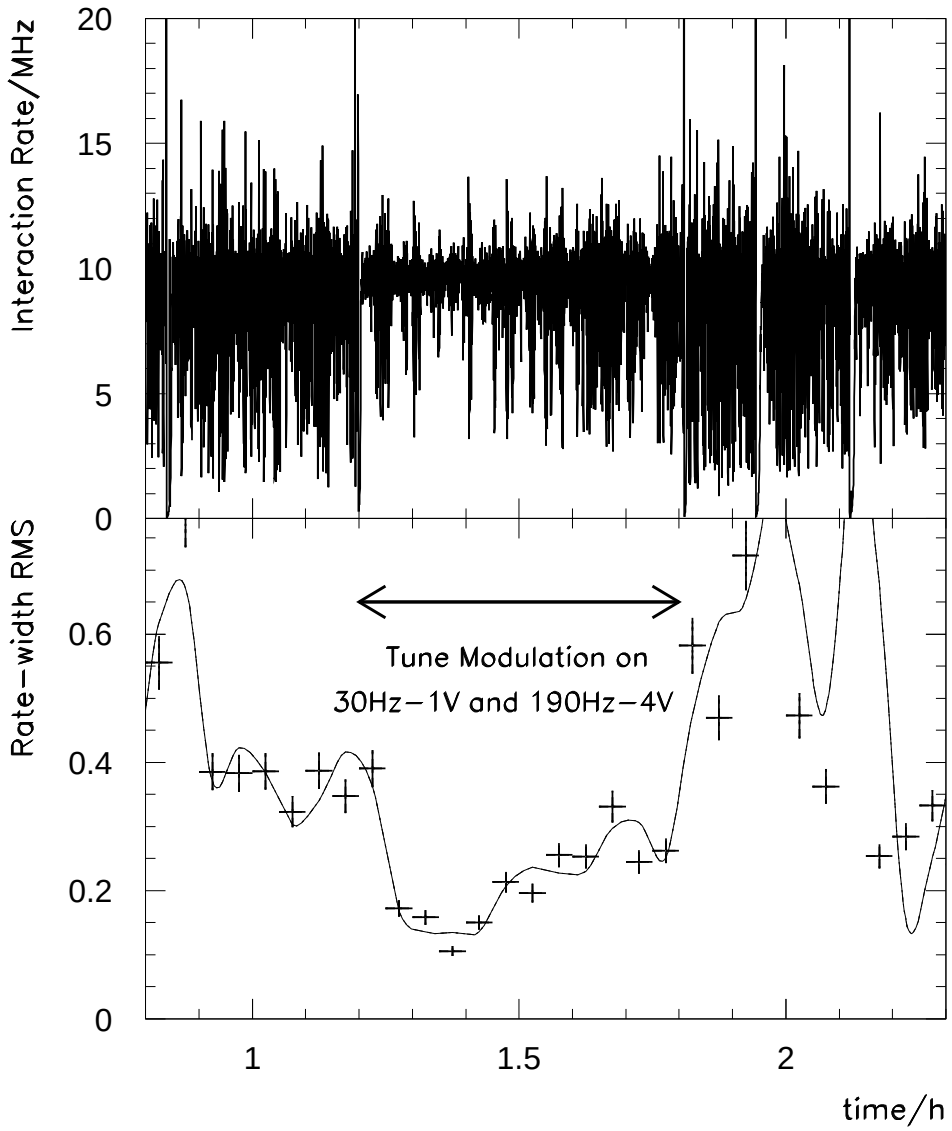


**Figure 14.5**: Interaction rate at the position–controlled target (above), and corresponding relative rms width of the rate fluctuations (below). The tune modulation was switched on from 1.2hours to 1.8hours.

one gives the phase space structure for the following parameter set:

$$\begin{aligned} f_1 &= 1/5000\text{turns}^{-1}, \\ f_2 &= 1/250\text{turns}^{-1}, \\ \Delta Q_1 &= 0.015, \\ \Delta Q_2 &= 0.001. \end{aligned} \tag{14.6}$$

At $5\sigma$ amplitude the resonance islands of the 10th order resonance appear. In the last plot of figure 14.6 the modulation depth $\Delta Q_1$ has been increased to $\Delta Q_1 = 0.015$, while the other parameters are kept constant. Now the islands of the 10th order resonance overlap and form a stochastic layer.

When the target wire Below I was used instead of Inner II, the interaction rate was significantly less stable, but the stability was improved compared to the situation without tune modulation.

## 14.4 Conclusion

It has been shown successfully that tune modulation might be a reasonable way to improve the interaction rate stability at HERA–B. During all the experiments the specific luminosity at the collider experiments ZEUS and H1 did not suffer at all as shown in figure 14.7. However, the applied tune modulation depth had to be extremely large due to the small positron current and the tight collimator setting. To improve this situation further studies, both theoretically and experimentally, are necessary. Since no negative impact on luminosity or background conditions was observed, it should be possible to perform further experiments parasiticly during regular luminosity runs.

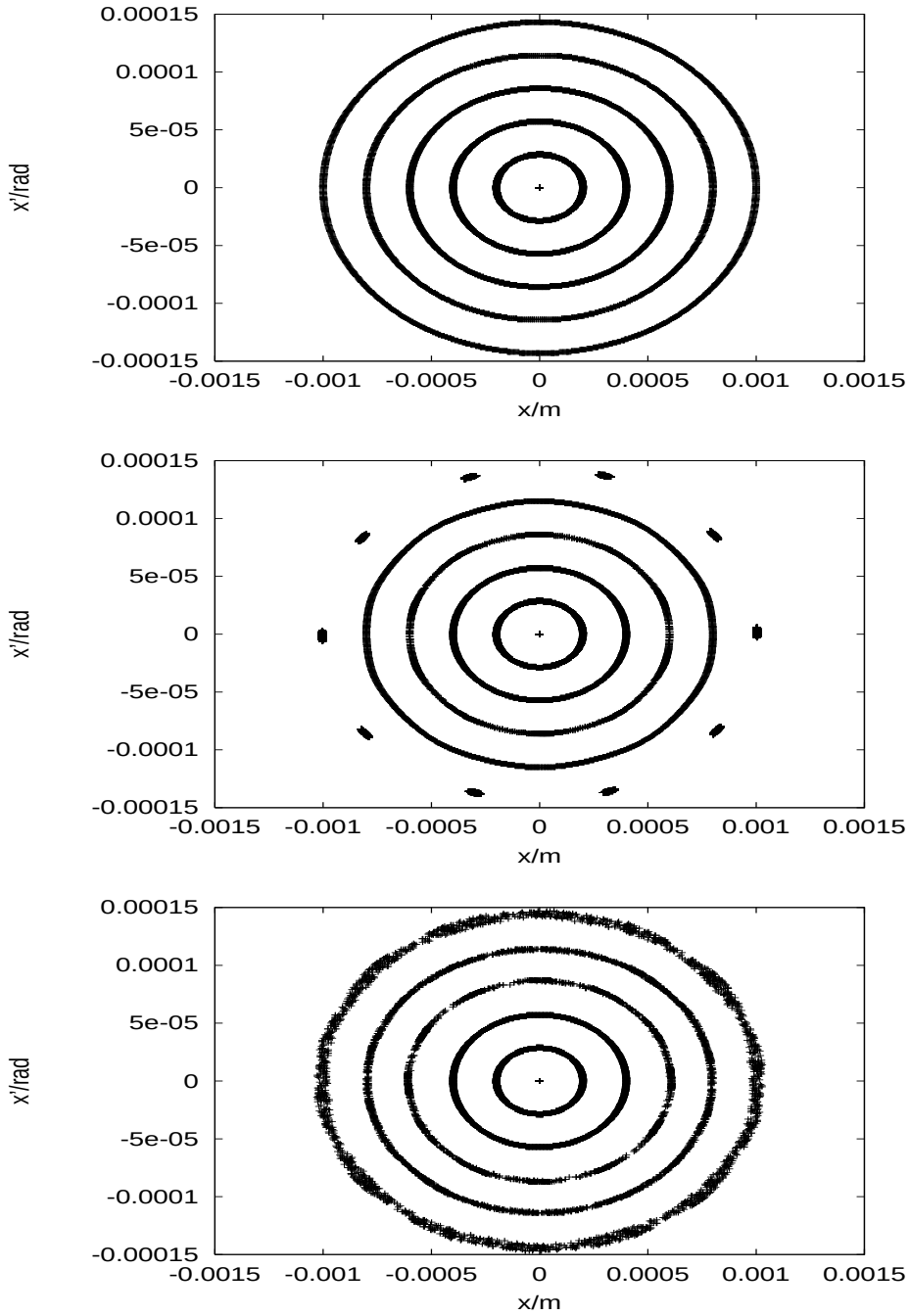


**Figure 14.6**: Horizontal phase space for a realistic positron bunch population of $N_b = 1.4 \cdot 10^{10}$, without tune modulation (top), with tune modulation parameters according to equation 14.6 (middle), and with enhanced modulation depth $\Delta Q_1 = 0.015$.

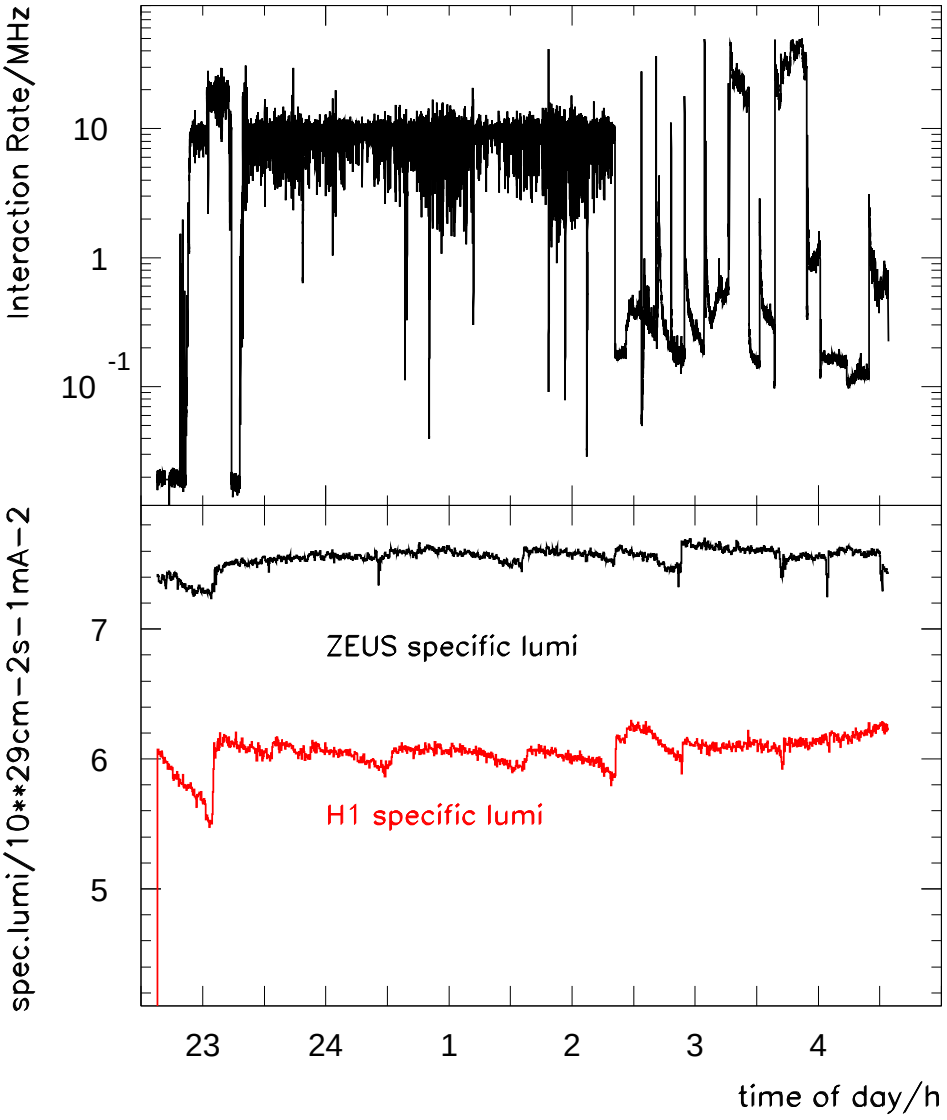


**Figure 14.7**: Specific luminosity at the colliding beam experiments ZEUS and H1 during the tune modulation studies on December 14th/15th, together with the HERA–B interaction rate.

# 15 Longitudinal Beam-Transfer-Function Measurements for HERA–p

by E. Vogel, W. Kriens, and U. Hurdelbrink, Desy Hamburg

Date: 1999, Dec. 15, 3pm to 11pm, Logbook XXXXI, p. 44

The emittance of the bunches in the proton storage ring from HERA blows up during ramping and at injections. For reducing these effect we started to set up an RF feed–forward system. With the now working detection of the complex 52 MHz bunch Fourier components we are able to detect dipole multi bunch oscillations in the time domain. To better understand these oscillations and the resultant emittance blow up, we measured the integral beam phase under harmonic oscillations of the RF phase. Out of these measurements follows the order of magnitude from the damping time of coherent multi bunch oscillations. The damping depends on the operating conditions of both RF systems. We also observed the dependence on the bunch length and hysteresis effects.

## 15.1 Theoretical Expectations

To measure the longitudinal beam-transfer-function (BTF) one excites dipole oscillations in the proton beam by a sinusoidal modulation of the RF phase. The ratio between the amplitude of the excitation and the amplitude of the beam oscillation is the amplitude of the BTF. From the phasing between the excitation and the beam oscillation follows the phase of the BFT.

We expected out of simple theoretical considerations a asymmetric BTF. The amplitude is

$$A_{BTF} = \int d\omega \frac{\omega^2 n(\omega)}{\omega^2 - \omega_{\mathrm{mod}}^2 + 2i\alpha\omega_{\mathrm{mod}}} \tag{15.1}$$

and the phase applies

$$\varphi_{BTF} = \int d\omega \tan^{-1}\left(\frac{2\alpha\omega_{\mathrm{mod}}}{\omega^2 - \omega_{\mathrm{mod}}^2}\right) n(\omega) \tag{15.2}$$

where $\omega$ is the eigenfrequency of each Proton, $n(\omega)$ the frequency distribution in a bunch, $\omega_{\mathrm{mod}}$ the modulation frequency and $\alpha$ the damping constant.

We suppose the frequency distribution

$$n(\omega) = \begin{cases} \frac{e^{-\frac{1}{2\sigma^2}\arccos^2(\frac{2\omega}{\omega_{sc}}-1)}}{\sqrt{2\pi}\sigma} & \text{for } \omega \le \omega_{sc} \\ 0 & \text{else} \end{cases} \tag{15.3}$$

where $2\sigma$ is the bunch length and $\omega_{sc}$ the synchrotron frequency in the core. This distribution is plotted in Figure 15.1.

One gets the shape of the BTF at parameter settings, figure 15.2 and figure 15.3.

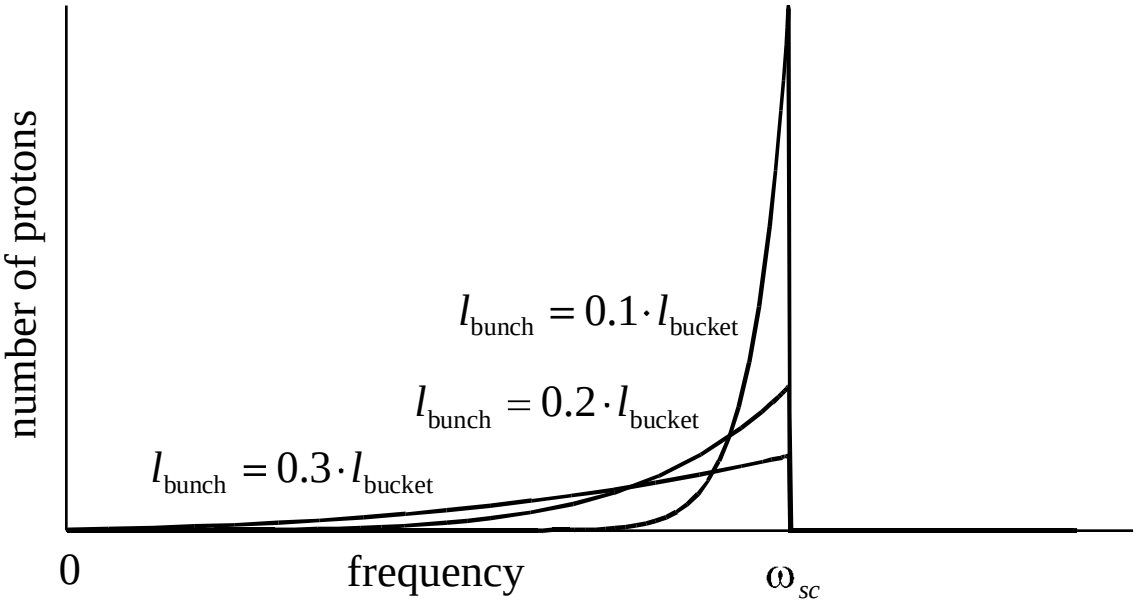


**Figure 15.1**: Number of protons with a specific eigenfrequency. As longer the bunch as more protons have lower eigenfrequencies.

## 15.2 Principle of the Excitation

For our measurements we unpicked the existing narrow band phase loop II. Inside this loop an ADC converts an analog Signal to a frequency shift of the RF reference. With the 100 kHz clock of this ADC we are able to shift the RF frequency for $\Delta t = 10\,\mu s$ and switch this shift afterwards off see figure 15.4. The time between this shifts given is the period time of the needed phase modulation frequency for the BTF measurements.

In figure 15.4 one can see the resulting phase shift caused by this mechanism. Because $\frac{\Delta t}{1/f_{\text{mod}}} \ll 1$ for $f_{\text{mod}} = 1\text{Hz}$ to $f_{\text{mod}} = 100\text{Hz}$ one gets the phase change of

$$\begin{aligned} \Delta\phi(t) &= 2\pi\Delta f_{RF}\Delta t f_{\text{mod}} t && (15.4)\\ &\quad +2\Delta f_{RF}\Delta t \left(\frac{\sin 2\pi f_{\text{mod}} t}{1}\right. && (15.5)\\ &\quad \left. +\frac{\sin 4\pi f_{\text{mod}} t}{2} + \frac{\sin 6\pi f_{\text{mod}} t}{3} + \ldots\right) . && (15.6) \end{aligned}$$

For the BTF measurements only the main frequency is relevant:

$$\Delta\phi_{BTF}(t) = 2\Delta f_{RF}\Delta t \sin 2\pi f_{\text{mod}} t \; . \qquad (15.7)$$

The also produced higher frequencies are principally not wanted, they can be viewed as perturbations.

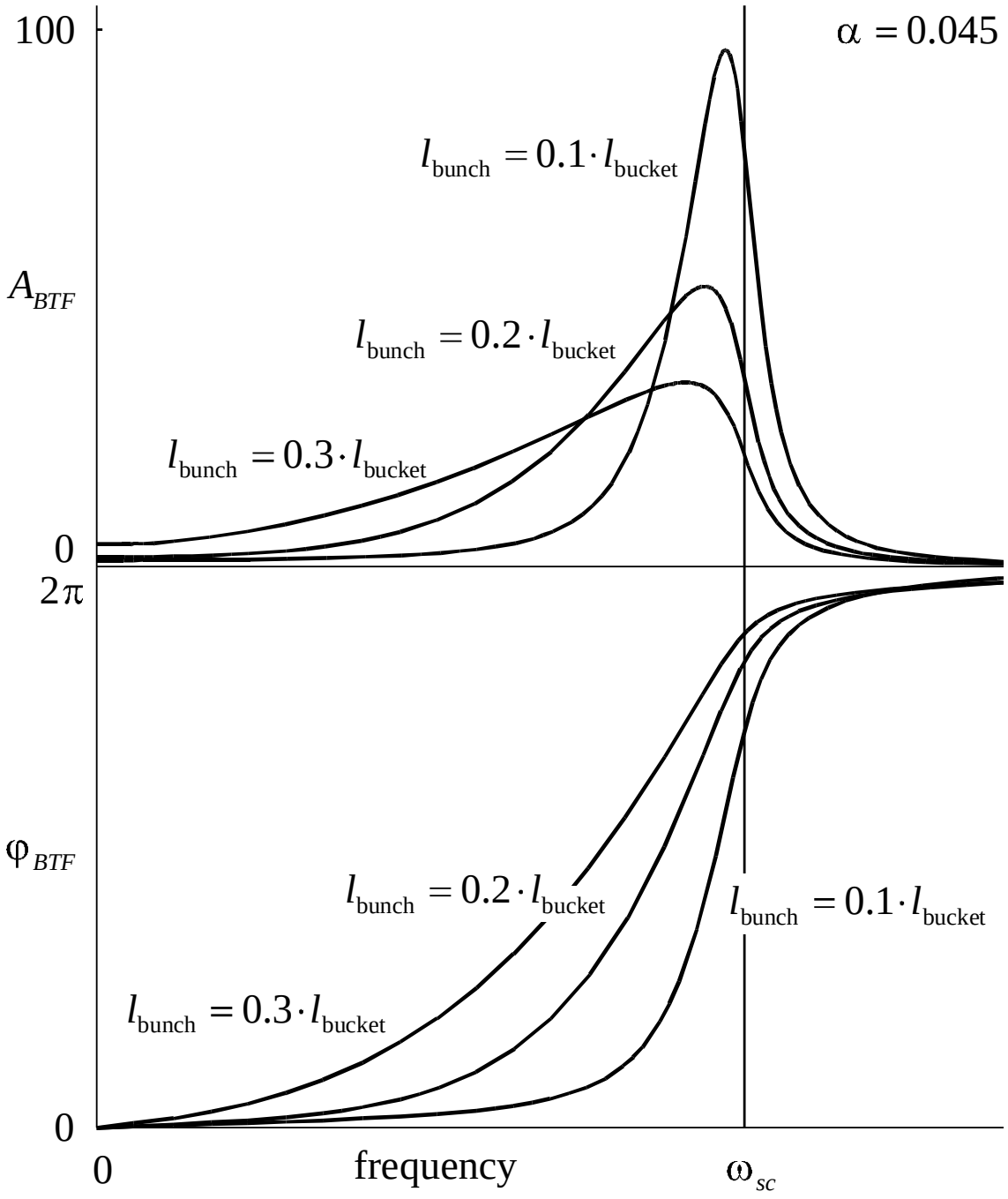


**Figure 15.2**: As longer the bunch as lower is the maximal amplitude of the BTF and as lower the frequency is at this point. All this curves was computed with the same damping constant $\alpha = 0.045$.

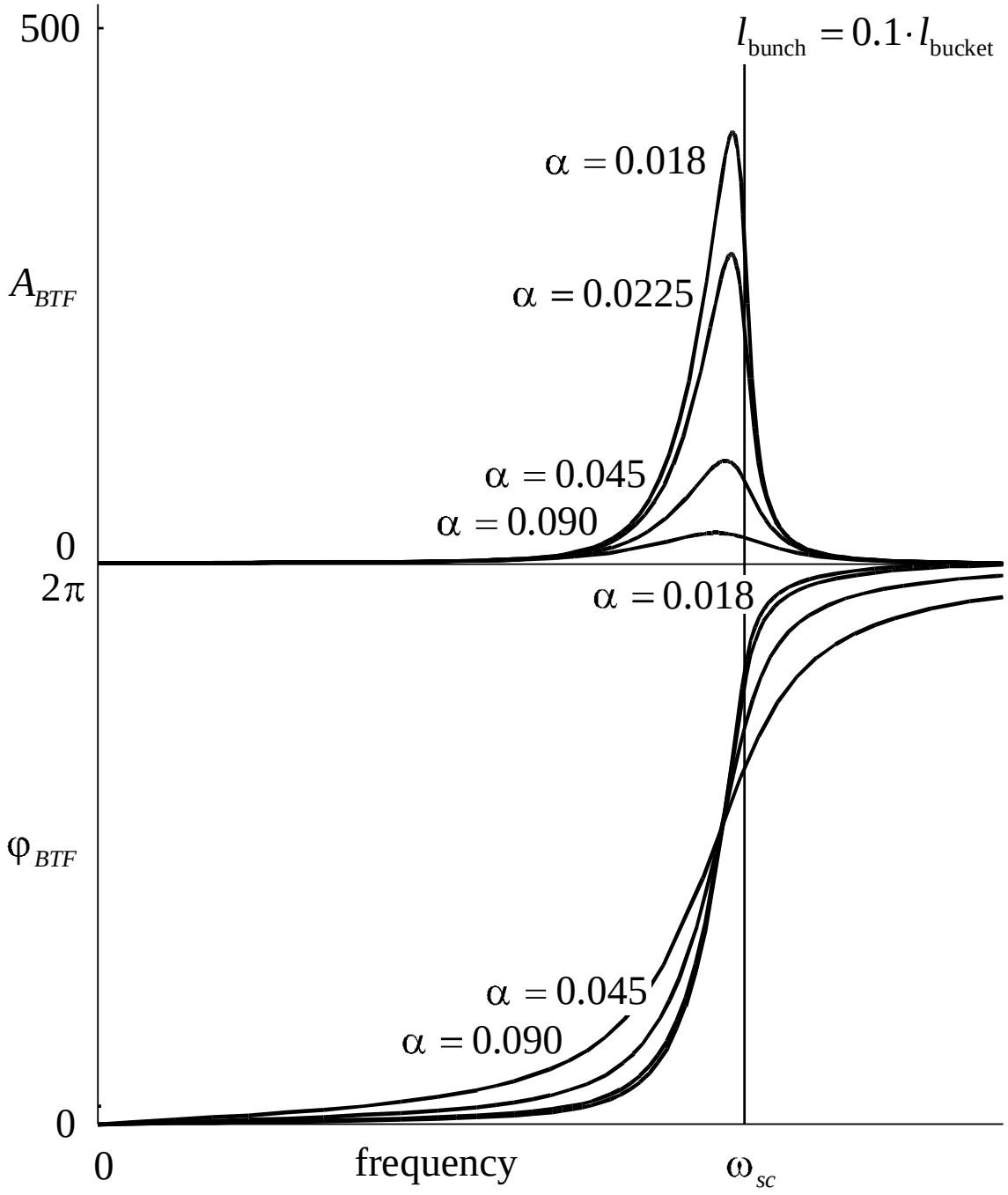


**Figure 15.3**: A variation of the damping at constant bunch length of $l_{\text{bunch}} = 0.1\ l_{\text{bucket}}$ also varies the maximal amplitude of the BTF.

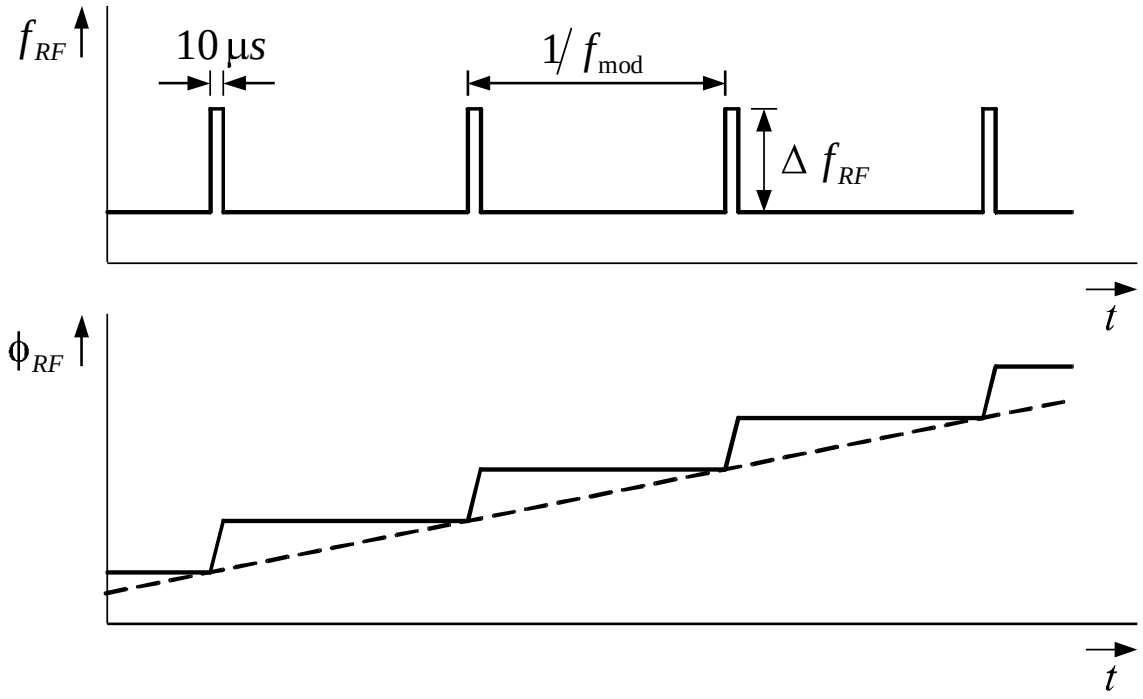


**Figure 15.4**: A shift of the RF frequency for $10\mu s$ each $\frac{1}{f_{\mathrm{mod}}}$ leads to a stepwise change of the RF phase with a step length of $\frac{1}{f_{\mathrm{mod}}}$.

## 15.3 Results of our Measurements

First we started with the study of the influence of the 208 MHz System on the damping behavior. We observed a much higher damping when the 208 MHz System was switched on compared to machine state without 208 MHz voltage inside the cavities. These measurements were made at 40 GeV. See figure 15.5 to 15.9.

At 70 GeV we verified a synchrotron frequency above 50 Hz, see figure 15.10.

We also made measurements at 300 GeV and 920 GeV figure 15.11 and 15.12.

Since we were able to estimate the multi bunch oscillation status with the assistance of the new longitudinal multi bunch display, we are able to rate the quality of the measurements at the different excitation frequencies.

An interesting point is the hysteresis effect when we started the scan from lower frequencies. One excites most the protons which have eigenfrequencies near the actual excitation frequency. These Protons gets a higher oscillation amplitude and therewith a lower eigenfrequency. With a scan from lower frequencies one goes like a snowblower through the frequency distribution. A scan from higher frequencies works like a snow pusher. This results in a inflated BTF. See figure 15.13.

## 15.4 Conclusions

We have seen a big influence on the damping by the 208 MHz System. The damping of synchrotron oscillations is much higher with the 208 MHz System.

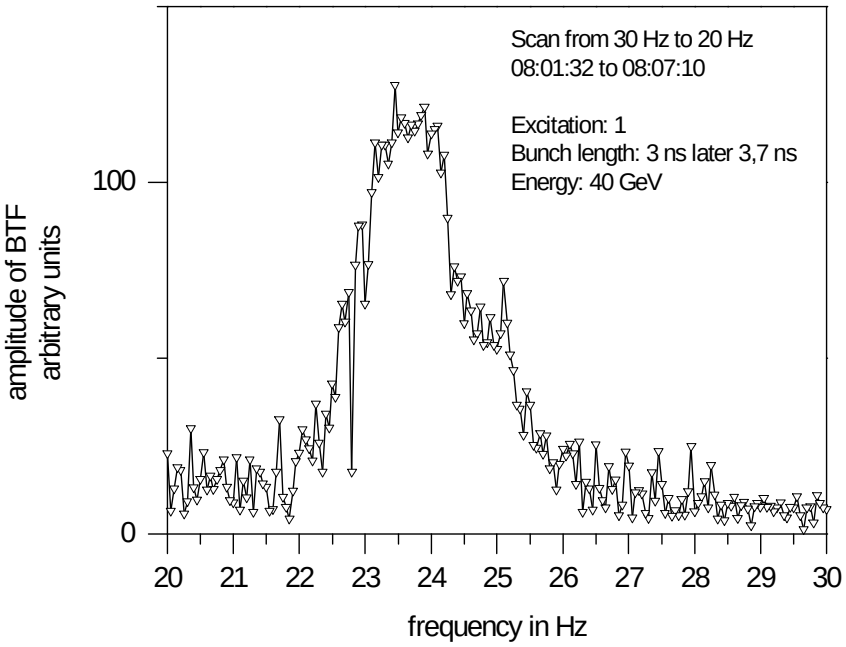


**Figure 15.5**: Standard situation i.e. 52 MHz and 208 MHz system on.

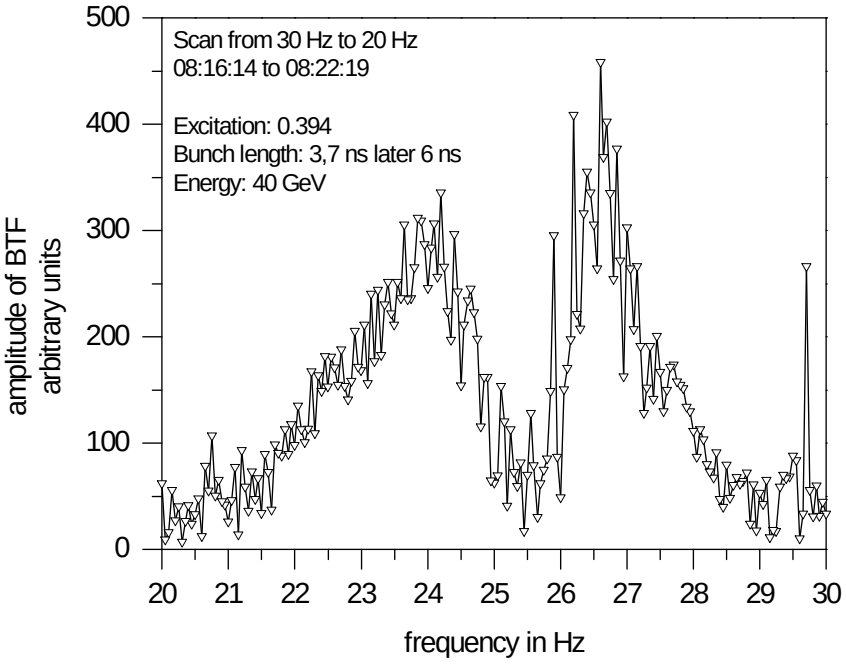


**Figure 15.6**: BTF with 52 MHz on and 208 MHz system off but with working 208 MHz fast feedback loop. The 208 MHz tuners was in standby positions.

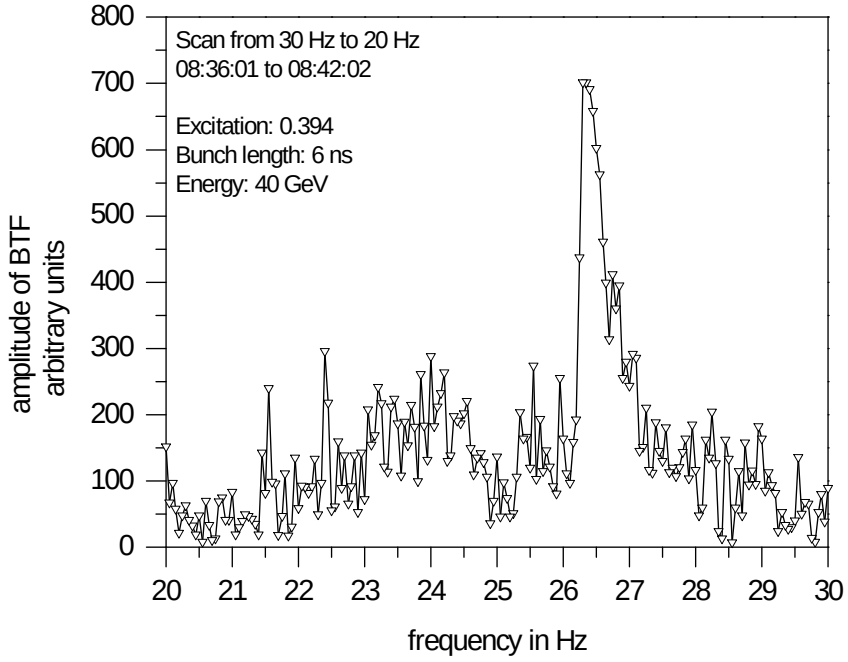


**Figure 15.7**: BTF with 52 MHz on and 208 MHz system off but with working 208 MHz fast feedback loop. The 208 MHz tuners was locked in the normal working positions.

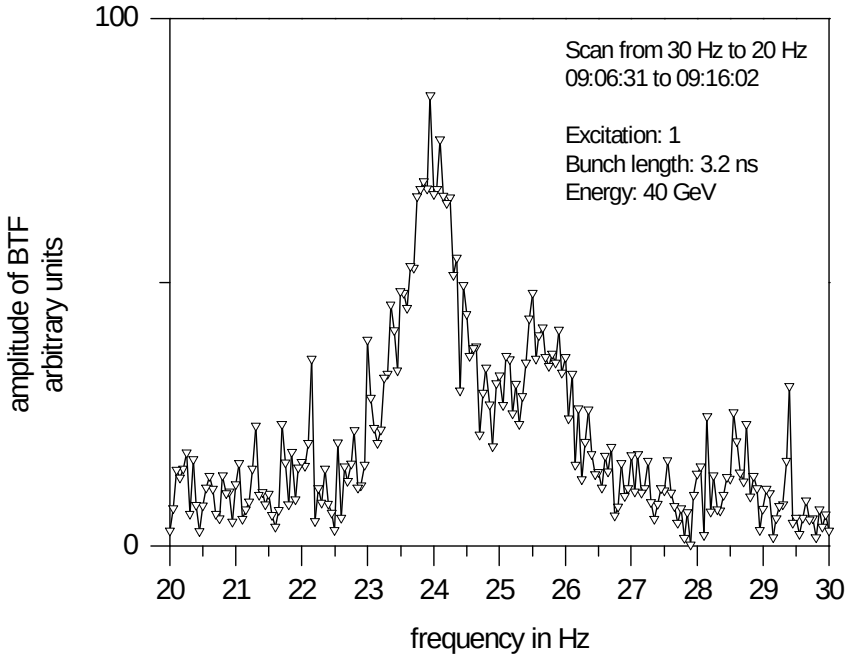


**Figure 15.8**: Standard situation after new injection i.e. 52 MHz and 208 MHz system on.

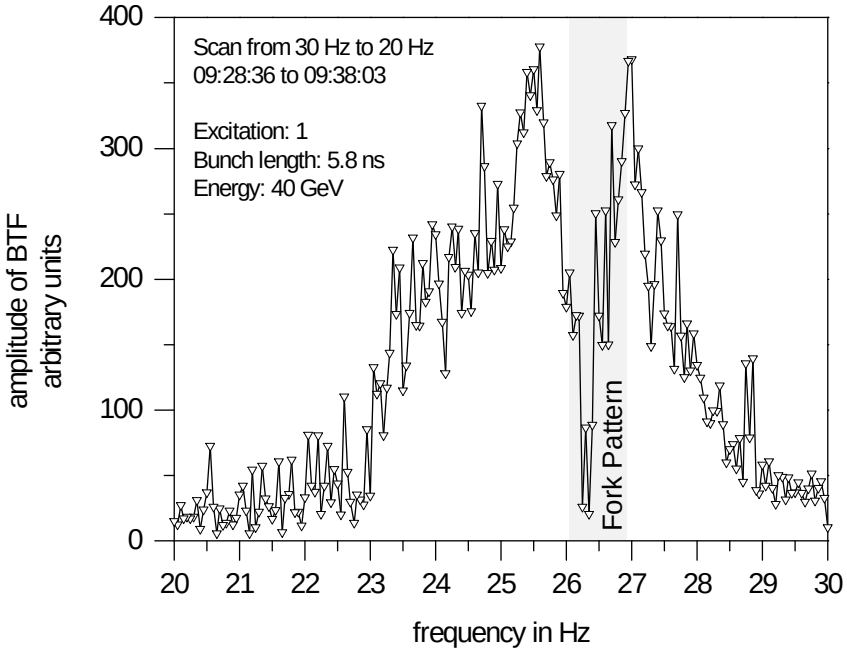


**Figure 15.9**: BTF with 52 MHz on and 208 MHz system off but with working 208 MHz fast feedback loop. The 208 MHz tuners was locked in the normal working positions. In the marked area was a higher multi bunch oscillation mode observable.

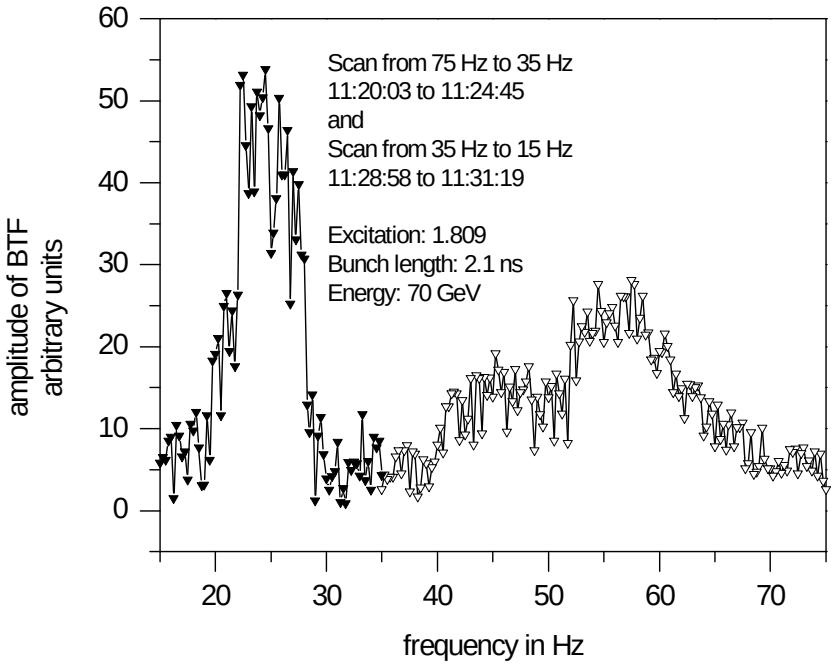


**Figure 15.10**: Standard situation at 70 GeV. One can see the synchrotron frequency above 50 Hz.

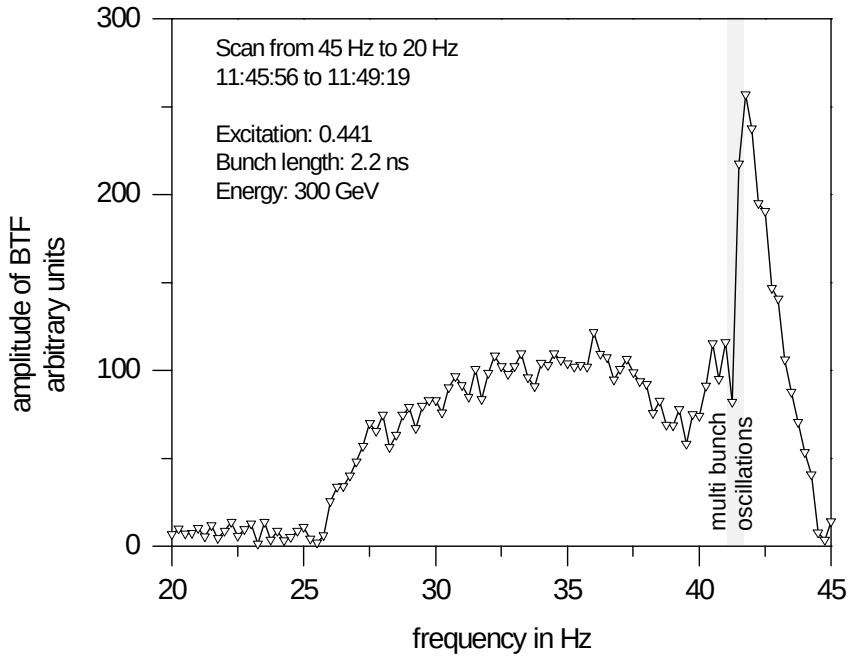


**Figure 15.11**: Standard situation at 300 GeV with higher multi bunch oscillation modes at the marked area.

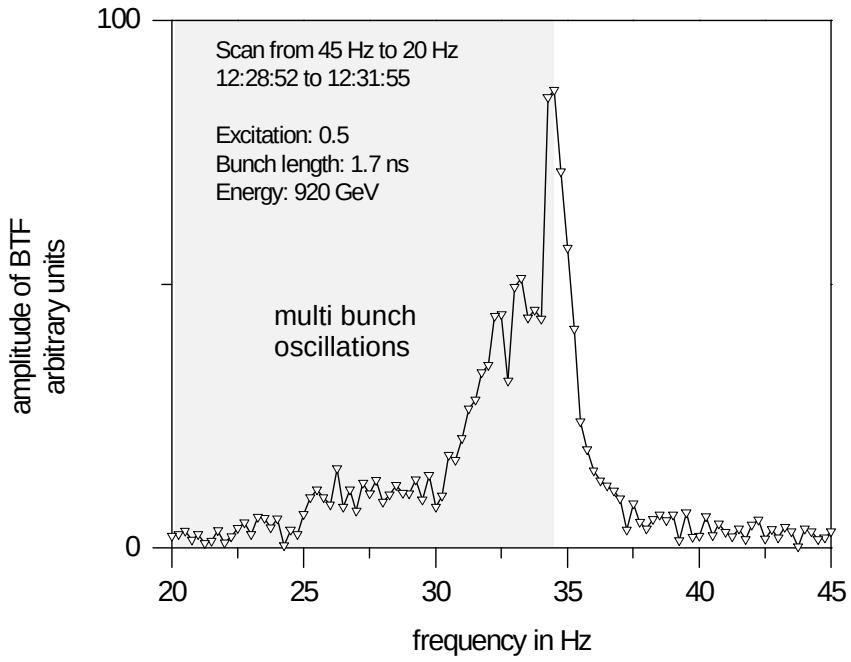


**Figure 15.12**: Standard situation at 920 GeV. We observed higher multi bunch oscillation modes at the marked area.

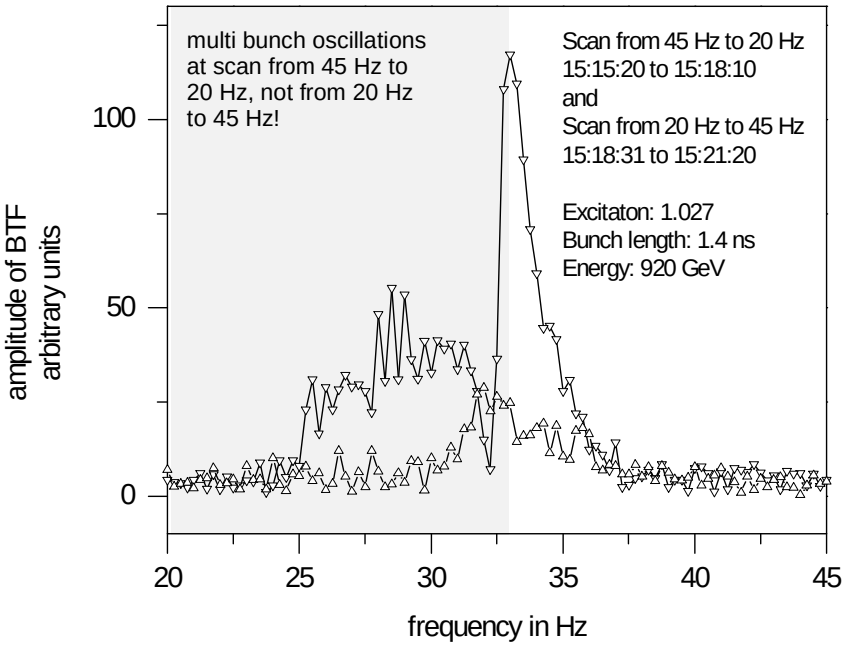


**Figure 15.13**: The hysteresis effect at different scan directions. One excites the protons most at the actual excitation frequency. These Protons gets a higher oscillation amplitude and therewith a lower frequency. With a scan from lower frequencies one goes like a snowblower through the frequency distribution. At a scan from higher frequencies one works like a snow pusher. This results in a inflated BTF.

But for more quantitative statements, we still have to work with the measured data. One open point is at the moment the calibration of the BTF amplitude. The reason for the nebulousity there is our sophisticated excitation method. Additional we discovered a systematic error in our BTF phase measurements. We first have to clarify in which way we have to correct our data. The interested reader will find later the results of this work in doctoral thesis from Elmar Vogel.

# 16 Excitation Studies for the "Head–Tail" Phase Shift Chromaticity Measurement Method

by O. R. Jones, CERN and C. Montag, M. Wendt, DESY Hamburg

Date: 1999, Dec. 13, 3pm to Dec. 14, 7am Logbook XXXXI, p. 29–30
1999, Dec. 15, 11pm to Dec. 16, 7am Logbook XXXXI, p. 45–46

Based on earlier "head–tail" phase shift chromaticity experiments a single bunch excitation and measurement method could be established.

## 16.1 Introduction

The method for resolving the *chromaticity* of a proton beam by exciting "head–tail" oscillations and measuring the coherent turn–by–turn phase shift was shown in theory and practice [46, 47].

It turned out from our previous experiments at HERA-p [48] that several improvements are needed to implement the head–tail chromaticity measurement method as practical routine setup:

**Detection hardware** Since a closed orbit distortion at the location of the beam position monitor (BPM) used for the detection of the turn–by–turn phase shift would limit the sensitivity of the chromaticity measurement, a local feedback loop in the front–end detection hardware has to be used to automatically compensate for these closed orbit beam offset signals.

**Excitation signals** As the detection hardware is capable of analyzing a selected single bunch on a turn–by–turn bases it is sufficient to also excite only one bunch. In this way the blowup of the transverse emittance is minimized, since it would be possible to excite a non–colliding "pilot" bunch.

**Theory** The theory describing the head–tail phase evolution is based on a single kick excitation. To minimize the emittance blowup of the excited bunch a chirp excitation is preferred. However, with chirp excitation a beating effect in the phase evolution of the signals resulting from such an excitation cannot be explained on this basis and requires a modification to the theory.

Based on the 1998 head–tail results we experimented this time with a different excitation hardware and signals. Introductory information on the measurement principle and details on its implementation at the HERA proton ring are found in [48, 49].

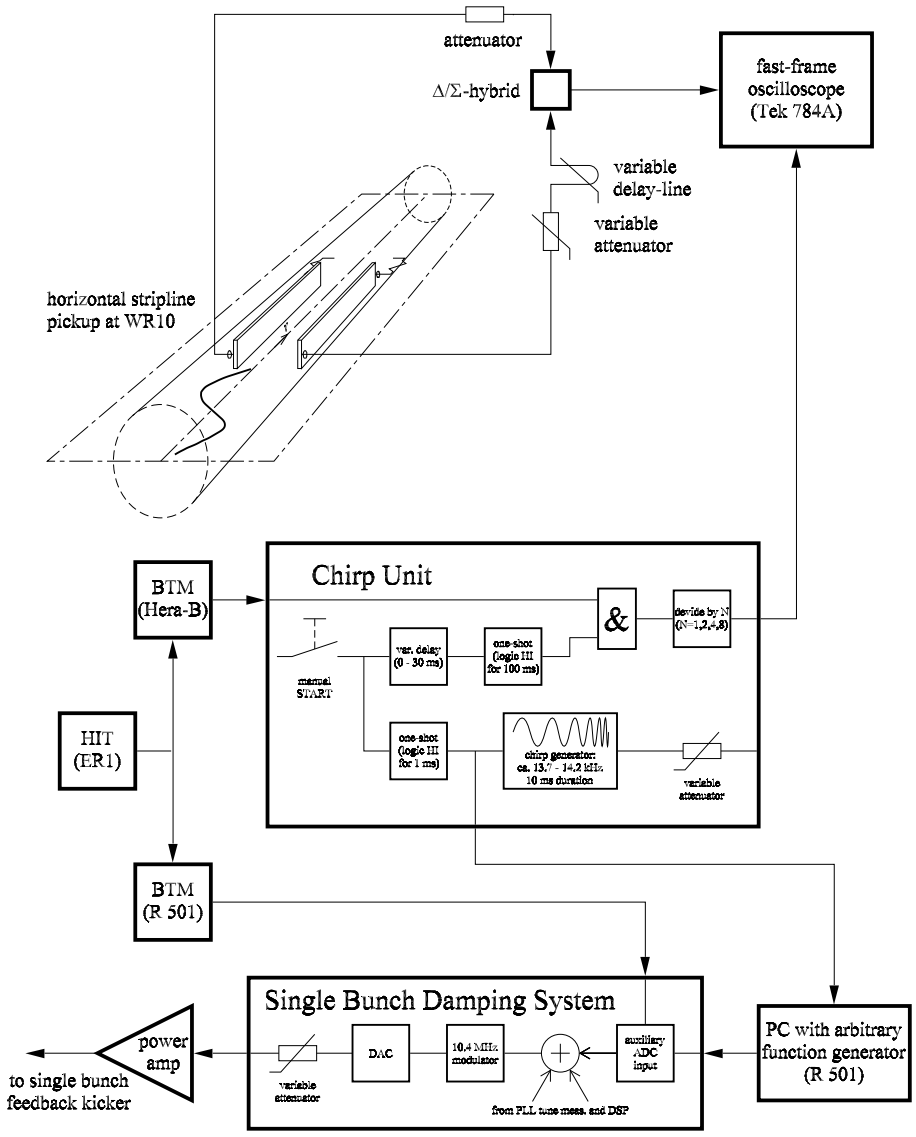


**Figure 16.1**: Hardware setup for the chromaticity measurements with chirp excitation.

## 16.2 Experimental Procedure

### 16.2.1 Hardware Setup

Compared with the winter 1998 measurements the hardware setup was changed only at the excitation path (see Figure 16.1). The manual start trigger on the *chirp unit* was sent to a PC–based *arbitrary waveform generator*, located in Halle West room 501. This software programmable generator replaced the analog chirp generator on the chirp unit. We programmed a similar chirp waveform, 13.170...14.42 kHz, 10.25 ms duration with an internal sampling rate of $\Delta t = 0.5$ $\mu$s.

This digital signal $v(i\Delta t)$ can be described as

$$v(i\Delta t) = \sin(2\pi f_{\text{chirp}} i\Delta t), \tag{16.1}$$

with

$$f_{\text{chirp}} = f_{\text{start}} + \frac{\Delta f}{2N_{\text{chirp}}} \cdot i. \tag{16.2}$$

Here $f_{\text{start}} = 13.170$ kHz, $\Delta f = (14.42 - 13.17)$ kHz $= 1.25$ kHz, and $N_{\text{chirp}} = 10.25$ ms/0.5 $\mu$s was used.

Instead of using the resonant **SSB** excitation system of the tune measurement, we now used a part of the broadband *transverse damping system* [50] to excite a selected single bunch. It has an auxiliary digitizing input which samples the chirp signal generated with the arbitrary waveform generator. The turn–by–turn sampling is synchronized via the HERA *integrated timing* HIT system to the proton bunches circulating in HERA. Any single bunch is selectable for excitation. A 10.4 MHz digital synchron modulator is used in the system to overcome the 300 kHz lower cutoff frequency of the power amplifier. The bandwidth of the amplifier/kicker system allows the excitation of a single bunch in a train of 96 ns spaced bunches.

Everything in the signal detection path as well as data sampling and read–out technique stayed unchanged from the winter 1998 setup.

### 16.2.2 Shift Operations

During the machine study period in December 1999, three shifts were scheduled for head–tail chromaticity measurement experiments. During the late shift December, 13 we started to setup the new front–end hardware to eliminate the closed orbit offset. This was manufactured just in time and had therefore not been fully tested. The system is based on a voltage–controlled variable attenuator, which automatically compensates the closed orbit offset at the $\Delta/\Sigma$–hybrid input. Unfortunately this new hardware system was damaged when an electrolytic capacitor in the BPM subsystem started to burn(!) for unknown reasons. Because of the limited shift time we decided to stop our activities on this brand new hardware and switched back to our original setup as used in the winter 1998 measurements (Figure 16.1).

We therefore started with the same measurements as in the winter 1998 experiments [1]:

[1] see section 9.3.2 and Figure 28 in [48]

This meant exciting all injected bunches, using the analog chirp generator, located on the chirp unit to modulate the signal for the resonant SSB–modulated kicker. The beam current was 4. . . 5 mA in 10 bunches at 40 GeV/c injection energy. After solving some problems with our data analysis program which calculated a wrong chromaticity from the recorded, "well looking" head–tail signals, the chromaticity measurement at injection energy started.
Later during this shift we ramped 10 bunches up to 677 GeV/c, while taking many chromaticity measurements at various beam energies. The level of the chirp excitation signal had to be increased during the ramp to get an acceptable response.

During the following night shift we changed the setup to excite a single bunch via the transverse damping system, but still using the analog chirp unit to produce the chirp signal. The excitation was now limited to the selected bunch #4 of the 10 filled bunches, which were spaced by 96 ns. The excitation level of the neighboring bunches #3 and #5 was negligible. The chromaticity of the proton beam was analyzed at 40, 70 and 150 GeV/c with different sextupole settings using the single–bunch head–tail chirp method and comparing this with the "classic" chromaticity measurement which obtains the chromaticity by changing the RF frequency in order to provide the required momentum change. The head–tail signals looked fine, particularly at small or negative chromaticities, but we still had some problems with the data analysis. At 40 GeV/c beam energy the observed turn–by–turn phase difference evolution is rather small, so we expect difficulties to compute the correct chromaticity for high chromaticities.

On December 15/16, night shift starting at 11 pm we unplugged the analog chirp generator and cabled the manual start trigger signal from the chirp unit to the PC–based arbitrary waveform generator (see Figure 16.1). The programmed chirp signal had similar parameters as for the analog chirp generator: ca. 13.1 kHz to 14.2 kHz, 10.25 ms duration to excite bunch #4 during $\approx$ 500 turns at our 0.285. . . 0.31 betatron tune. After some fight with PC programming we saw the expected chirp signals. The excitation worked as well, if not better (due to lower noise) as for the analog generated chirps.
In the last hours of the night shift we tried to generate band limited noise signals. We could observe some kind of response, but the signals looked quite different compared to those with kick or chirp excitation. Without understanding these effects we recorded some data at 40 GeV/c beam energy and different sextupole settings before the end of the shift.
The idea behind this kind of excitation was to build up a sufficient excitation amplitude before stopping the excitation and looking for the phase evolution of the head and tail. It was hoped that this would more closely resemble single kick excitation by removing the phase errors introduced by the chirp method. However, as it turned out this did not prove to be the case, and no coherent dephasing of head and tail was observed.

## 16.3 Results

### 16.3.1 Analog chirp excitation

The results from the first shift using the same excitation scheme as for the December 1998 measurements proved, as expected, to be similar to those obtained in 1998.

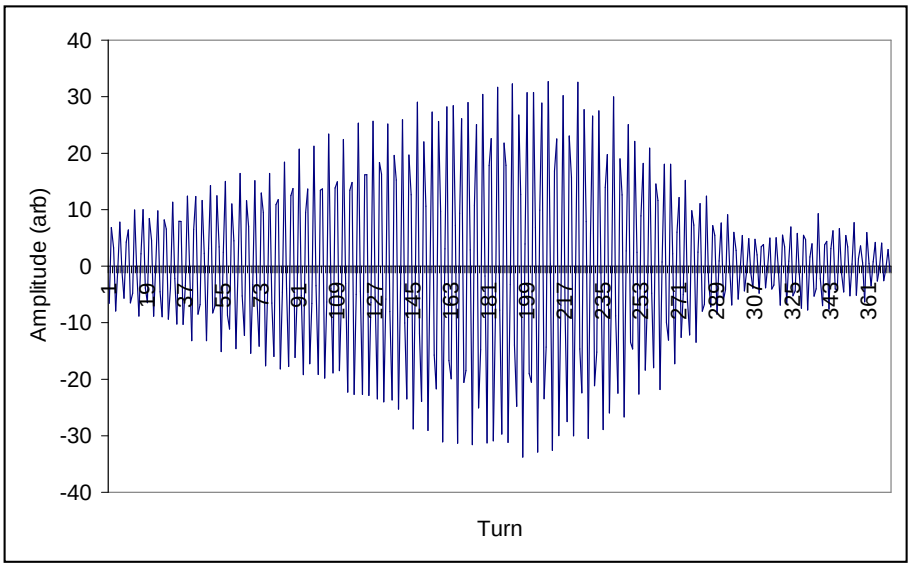


**Figure 16.2**: A typical chirp signal using the analog chirp generator, which excited all injected bunches.

Figure 16.2 shows a typical signal from such an excitation, with the corresponding head–tail phase changes and chromaticity shown in figures 16.3 and 16.4. All these measurements were taken in the horizontal plane at 150GeV with the horizontal chromaticity measured in the BKR as +5. It is again clear that the chirp excitation introduces phase errors, which can bee seen as a drop in oscillation amplitude in figure 16.2, or as a phase jump in figure 16.3. The analysis therefore has to be limited to turns 150–250, where the phase errors introduces by the chirp excitation is negligible. From figure 16.4 it can be seen that using these limited number of turns, the chromaticity by head–tail dephasing is calculated as +4, which is within experimental errors is in agreement with the BKR value of +5.

### 16.3.2 Computer generated chirp excitation

A similar set of results was obtained using the computer generated chirp signal, which excited a single bunch via the transverse damping system (figures 16.5–16.7). In this particular case the results were from exciting bunch #4 at 150GeV with a horizontal chromaticity of +3.5 as measured in the BKR. Once again the head–tail technique is in fairly good agreement, with the limited number of usable turns in figure 16.7 giving an average chromaticity of +3.

Figure 16.8 shows the result from a measurement where the BKR measured the horizontal chromaticity to be -2. Again a fairly good agreement is seen, with the

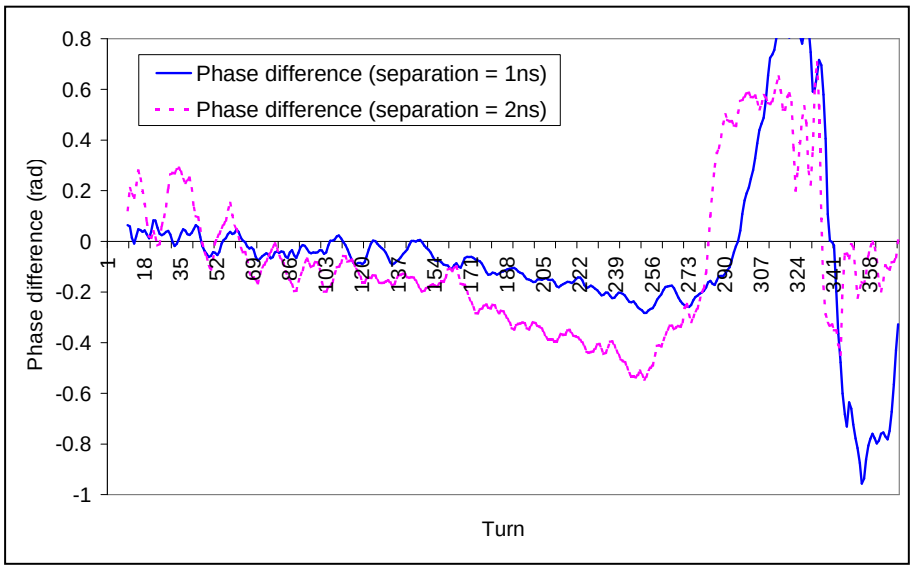


**Figure 16.3**: The phase difference between head and tail for 2 different head–tail separations (excitation of all bunches using an analog chirp generator).

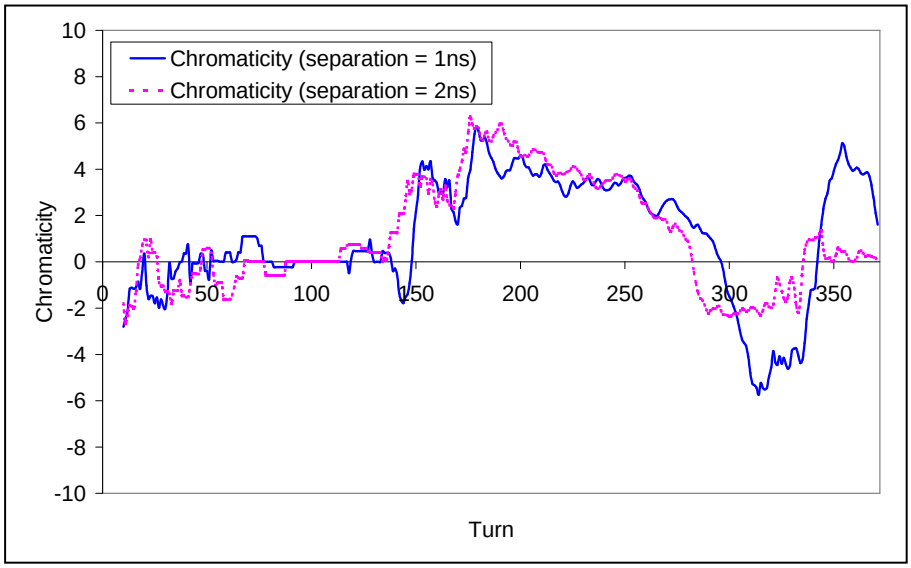


**Figure 16.4**: Turn by turn chromaticity for 2 different head–tail separations (excitation of all bunches using an analog chirp generator).

head–tail chromaticity calculated to be -1.5.

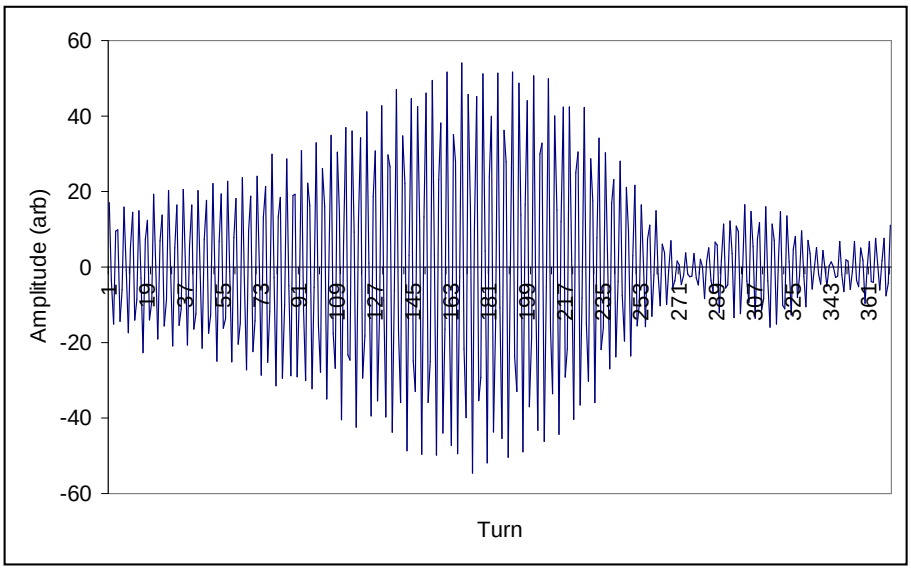


**Figure 16.5**: Typical single–bunch excitation signal from a computer generated chirp.

## 16.4 Conclusions

Unfortunately the results from this year's machine shifts did not advance the study of using head–tail technique for use as an everyday operational tool as much as we would have liked. In a broad sense the conclusions are the same as those presented last year:

- A fairly good agreement is found between the usual BKR chromaticity measurements and the calculation of chromaticity from head–tail phase shifts for low chromaticities after extensive analysis and data treatment and selection.

- The main factor complicating the measurement is the phase distortion that the chirp excitation itself introduces. This has yet to be introduced into the theory for calculating the chromaticity from studying the head–tail phase difference evolution.

- The long synchrotron period at low energies coupled to the fairly rapid damping of the signals at moderate chromaticities means that the phase differences to be measured are very small.

- The accurate calculation of the chromaticity will rely on the full synchronization of the chirp with the data acquisition to allow the analysis to be started at the point where the chirp crosses the betatron tune resonance. At the moment this is done by eye by looking at where the dephasing of head and tail begins.

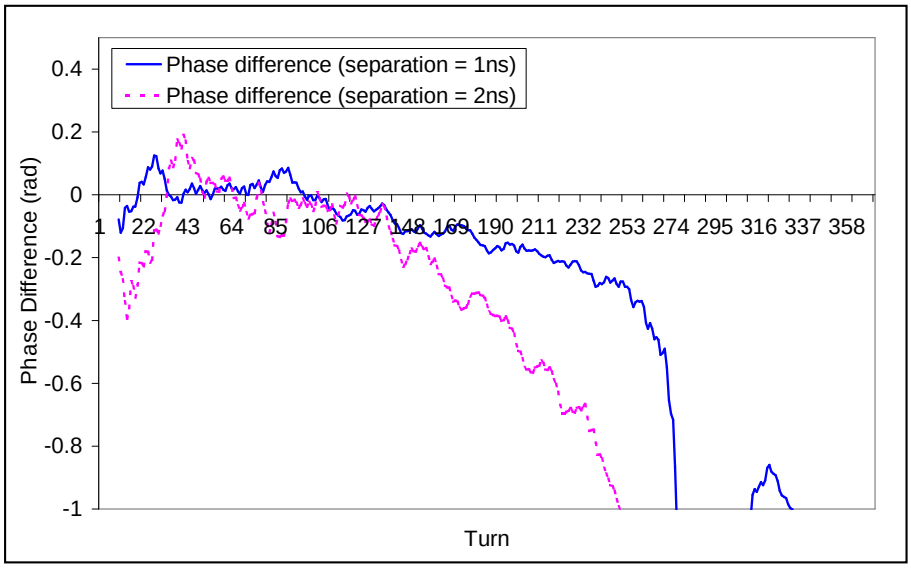


**Figure 16.6**: The phase difference between head and tail for 2 different head–tail separations (excitation of a single bunch using a computer generated chirp signal).

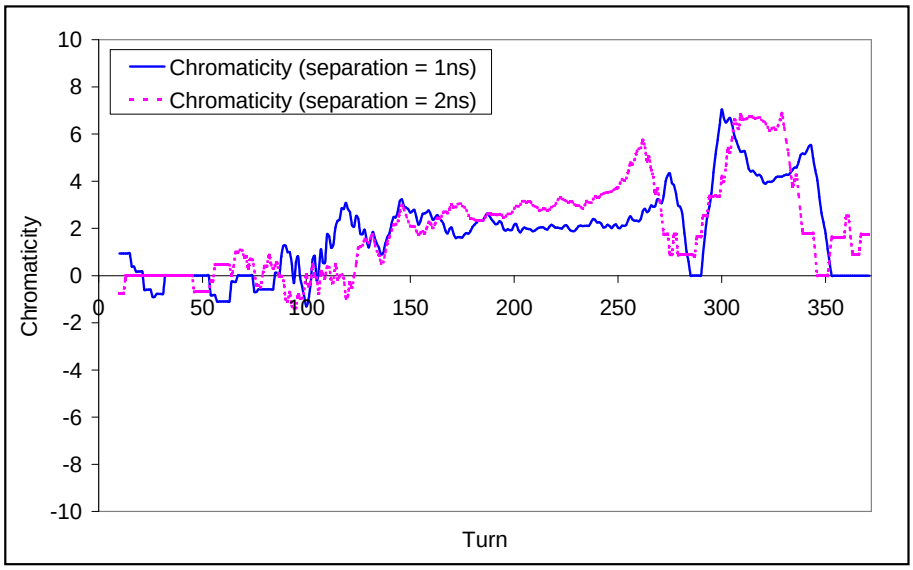


**Figure 16.7**: Turn by turn chromaticity for 2 different head–tail separations (excitation of a single bunch using a computer generated chirp signal). BKR measured chromaticity = +3.5.

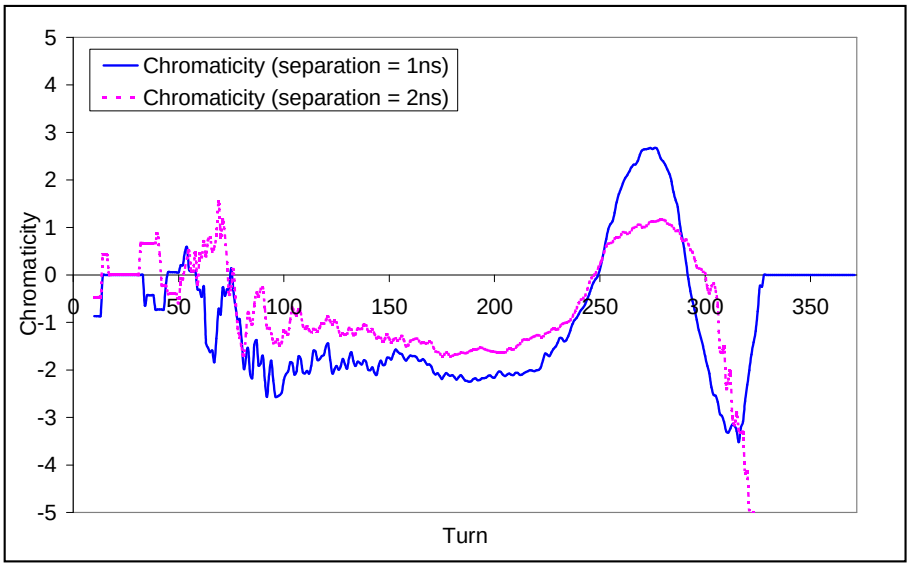


**Figure 16.8**: Turn by turn chromaticity for 2 different head–tail separations (excitation of a single bunch using a computer generated chirp signal). BKR measured chromaticity = -2.

One important positive step to come out of this year's studies were the possibility of exciting a single bunch using a computer generated chirp signal. Single bunch excitation would significantly reduce emittance blowup problems by allowing the measurement to be performed on non–colliding bunches. The computer generation of the chirp signal should allow for the future a full synchronization of the chirp and acquisition. The generation of the excitation signal in this way also makes the excitation scheme much more flexible. During this year's machine studies a single bunch was successfully excited using chirp, white noise and bandwidth limited noise. However, the attempt to observe head–tail dephasing after the noise excitations did not give any comprehensible results. In the future, one could envisage using more complicated excitation algorithms, which could possibly remove the phase distortion currently limiting the measurement with chirp excitation. This was the original aim for trying the noise excitation.

# References

[1] HERA, A Proposal for a Large Electron Proton Colliding Beam Facility at DESY, *Report DESY–HERA–81–10* (1981)

[2] R. Brinkmann and F. Willeke, First Experience with Colliding Electron-Proton Beams in HERA, *IEEE Proc. PAC93, Washington/DC* (1993)

[3] U. Schneekloth (ed.), The HERA Luminosity Upgrade, *Report DESY–HERA–98–05* (1998)

[4] E. Gianfelice-Wendt, HERA Upgrade Plans, *Proc. EPAC98, Stockholm* (1998)

[5] B.J. Holzer, The HERA Run Year 1997, *Proc. HERA seminar 98, Bad Lauterberg, Report DESY–HERA–98–04* (1998)

[6] M. Bieler et al., Recent and Past Experiences with Beam-Beam Effects at HERA, *Proc. Beam–Beam Effects, CERN* (1999) and in *Report DESY–HERA–99–04* (1999)

[7] F. Willeke, HERA Status and Upgrade Plans, *IEEE Proc. PAC97, Dallas/TX* (1997)

[8] *Proceedings of EPAC96, Sitges/SP* (1996)

[9] D. Heins et al., The Transverse Damping System with DSP PLL Tune Measurement for HERA-p, in [8]

[10] E. Keil, Beam–Beam Dynamics, *CERN SL/94–78 (AP)* (1994)

[11] M. Bieler, E. Gianfelice-Wendt, G. H. Hoffstaetter (ed.), B. Holzer, S. Levonian, T. Limberg, M. Lomperski, M. Minty, Ch. Montag, R. Wanzenberg, M. Wendt, F. Willeke, and K. Wittenburg, HERA Machine Studies December 1998, *Report DESY–HERA–99–03* (1999)

[12] Bieler et al., in [11]

[13] W. Kriens and M. Minty, *private communication* (1999)

[14] R. Brinkmann, Proton Emittance Growth Caused by Electron RF-Noise and the Beam-Beam Interaction in HERA, *Report DESY–M–88–04* (1988)

[15] G. H. Hoffstaetter, New Beam Optics for HERA-e: Theoretical Investigations and Experimental Tests, *Reprot DESY–HERA–99–04* (1999)

[16] G. H. Hoffstaetter and F. Willeke, Electron Dynamics in the HERA Luminosity Upgrade Lattice of the Year 2000, *Proc. PAC99, New York* (1999)

[17] G. H. Hoffstaetter, Experiences with a 72° HERA-e Optics, in [11]

[18] G. H. Hoffstaetter, The Central Frequency of HERA-e, in [11]

[19] M. Sands, The Physics of Electron Storage Rings – an Introduction, *Report SLAC-121* (1970)

[20] G. H. Hoffstaetter, The Emittance in HERA-e for Different RF Frequencies, in [11]

[21] A. Meseck, The Emittance Measurements at the HERA Electron Ring with and without Beam–Beam Interaction, in [11]

[22] A. W. Chao, In *Frontiers of Particle Beams*, ed. by M. Month, S. Turner, *Lect. Notes Phys. Vol. 296 p. 51*, Springer (1988)

[23] T. Chen, J. Irwin, and R. H. Siemann, New Physics and Improvements in Beam–Beam Tail Simulations, *Report SLAC–PUB–7193* and in [8]

[24] Yu. I. Alexahin, Closed Orbit Effect on the Equiliberium Emittance in the HERA-e 90/60 Lattice, *Report DESY–HERA–99–02* (1999)

[25] B. Holzer, Measurement of the Center Frequency in the HERA Electron Ring, in [11]

[26] D.Sagan, Detection of Coupling Elements in CESR, *Proc. PAC99, New York* (1999)

[27] E. Gianfelice–Wendt, Coupling Measurements in HERA-e, in [11]

[28] J.Billan et al., Measurement of the LEP Coupling Source, *Proc. EPAC90, Nice p. 258–260* (1990)

[29] F.Willeke and G.Ripken, Methods of Beam Optics, *Report DESY–88–114* (1988)

[30] J.Kewisch et al., Vertical Dispersion Generated by Correlated Closed Orbit Deviations, *Report DESY–86–020* (1986)

[31] F. Ridoutt, 2. Institut fr Experimentalphysik der Universität Hamburg, *PIN-Strahlverlustmonitore und ihre Anwendung in dem HERA-Electronen-Ring* (in German), Diploma thesis, Report DESY–HERA–95–08 and W. Bialowons, K. Wittenburg, and F. Ridoutt, Electron Beam Loss Monitors for HERA, *Proc. EPAC94, London* (1994)

[32] K. Wittenburg, Preservation of Beam Loss Induced Quenches, Beam Lifetime and Beam Loss Measurements with the HERA-p Beam Loss Monitor System, *Nucl. Instr. Meth.* A345 p. 226–229 and *Report DESY–94–003* (1994)

[33] K. Wittenburg and F. Ridoutt, Experience with the Electron and Proton Beam Loss Monitor (BLM) System at HERA, in [8] and D. R. C. Kelly, W. Bialowons, K. Wittenburg, HERA Electron-Beam Lifetime Disruption Machine Studies and Observations, in [8] and K. Balewski, H. Ehrlichmann, J. Kouptsidis, K. Wittenburg, Influence of Various Integrated Ion Getter Pumps on Electron Lifetime in [8]

[34] A. W. Chao and M. Tigne, *Handbook of Accelerator Physics and Engineering*, World Scientific (1999)

[35] S. Schaller, *Determination of Individual Bunch Contribution to the HERA-B Interaction Rate*, Diploma thesis (in German) (1998)

[36] K. Ehret et al., Observation of Coasting Beam at the HERA Proton–Ring, *Report DESY–00–018* (2000)

[37] G. Hoffstaetter, *private communication* (1999)

[38] R. Neumann, *private communication* (1999)

[39] C. Montag, Status and First Results of HERA-B Machine Studies, in [11]

[40] K. Ehret, *private communication* (1999)

[41] W. Fischer, An Experimental Study on the Long-term Stability of Particle Motion in Hadron Storage Rings, *Report DESY–95–235* (1995)

[42] O. Brüning, An Analysis of the Long-Term Stability of the Particle Dynamics in Hadron Storage Rings, *Reprot DESY–94–085* (1994)

[43] E. Hartouni et al., *HERA-B Design Report, DESY–PRC–95–01* (1995)

[44] R. Brinkmann, A Simulation Study for the Beam-Beam Interaction of Protons with a Flat Electron Beam in HERA, *Report DESY–HERA–89–24* (1989)

[45] I. Ludwig, *private communication* (1999)

[46] D. Cocq, O. R. Jones, H. Schmickler, The Measurement of Chromaticity via a Head–Tail Phase Shift, *Proc. Beam Instrumentation Workshop BIW98, Stanford/CA* (1998)

[47] O. R. Jones, H. Schmickler, M. Wendt, F. Willeke, Head–Tail Chromaticity Measurements at HERA-p, *CERN Internal Note, SL Division* (1998)

[48] A. Budsko, O.R. Jones, M. Wendt, Head-Tail Phase Shift Measurements at HERA-p with Chirp Excitation, in [11]

[49] A. Boudsko, O. R. Jones, H. Schmickler, M. Wendt, F. Willeke, Chromaticity Measurements at HERA-p using the Head–Tail Technique with Chirp Excitation, Proc. European Workshop on Beam Diagnostics and Instrumentation for Particle Accelerators DIPAC99, Chester/UK (1999)

[50] D. Heins, J. Klute, R. D. Kohaupt, K. H. Matthiesen, S. Pätzold, J. Rümmler, The Transvers Damping System with DSP PLL Tune Measurement for HERA-p, *Report DESY–M–96–21* (1996) and in [8]